The Thermal Monitoring and Management of Lithium-Ion Batteries

Keith Michael Alcock

A thesis submitted in partial fulfilment of the
requirements of Edinburgh Napier University,
for the award of Doctor of Philosophy.

**School of Computing, Engineering
and the Built Environment**

September - 2023

Declaration

I hereby declare that the work presented in this thesis has not been submitted for any other degree or professional qualification and is the result of my investigation and independent work, except where stated otherwise.

This PhD process was conducted on a part-time basis between 2017 and 2023 under the supervision of Dr Keng Goh, Dr Francisco Vedreño-Santos and Dr Zuansi Cai at the School of Computing, Engineering and the Built Environment, Edinburgh Napier University.

Keith Michael Alcock

17th August 2022

Abstract

Battery Thermal Management Systems (BTMSs) are critical for the safe operation of Lithium-Ion Batteries (LIBs), especially in high-use applications such as electric vehicles (EVs). BTMSs are generally in charge of two major functions: monitoring battery temperature and managing temperature gradients caused by battery pack activity. The measuring of a LIB's temperature is essential for the successful deployment of battery packs. Furthermore, because degradation mechanisms are closely connected to battery temperature, the temperature gradient caused by battery discharge must be minimised as much as possible.

This thesis presents an experimental investigation of two battery thermal management fields: (i) testing of a novel temperature measurement method for individual cell-level monitoring of the LIB using Fibre Optic Sensors (FOS) and (ii) copper plated foam composite materials for passive LIB thermal management.

The first section of this thesis concentrates on the implementation of a FOS system on a single-cell and a three-cell parallel battery pack utilising Fibre Bragg Gratings (FBGs). In laboratory experiments, temperature measurements of a single-cell LIB and three-cell parallel battery pack are obtained by adopting a novel mounting method for the FOS, which is confirmed by comparison to standard thermocouple and platinum resistance sensing approaches. Cell-level temperature monitoring is achieved with an average error of 0.97 °C, 1.33 °C, and 1.27 °C for cells three different cells respectively, which is comparable with conventional thermocouple and platinum resistance sensing approaches.

The second section of this thesis demonstrates, experimentally, a novel use for copper plating of polyurethane foam substrates for passive battery thermal management. To capture heat generated by the cell, Phase Change Material (PCM) foam composites are used. A variety of experiments are carried out on various copper deposition quantities. The plated copper foam resulted in an average cell surface temperature reduction of 63.23%, which is comparable to the commercial alternative of 65.44% in the best scenario. This is crucial since the weight of the foam skeletons differs substantially in this scenario, with 91.47% less mass. It is demonstrated that copper plating can mimic the

characteristics of solid commercially available foams, leading to a substantial reduction of copper material, lowering the total cost implication.

Publications and Dissemination

The following are research outputs associated with the PhD work.

- K. M. Alcock, M. Grammel, L. Binetti, Á. González-Vila, K. Goh, and L. S. M. Alwis, "Feasibility Study on the Potential of Fibre Bragg Gratings for Thermal Monitoring of Cylindrical Lithium-Ion Batteries," in Optical Fiber Sensors Conference 2020 Special Edition, G. Cranch, A. Wang, M. Digonnet, and P. Dragic, eds., OSA Technical Digest (Optical Society of America, 2020), paper T3.49.

- Keith M. Alcock, Markus Grammel, Álvaro González-Vila, Leonardo Binetti, Keng Goh, Lourdes S.M. Alwis, An accessible method of embedding fibre optic sensors on lithium-ion battery surface for in-situ thermal monitoring, Sensors and Actuators A: Physical, Volume 332, Part 1,2021, ISSN 0924-4247, https://doi.org/10.1016/j.sna.2021.113061.

- Alcock, Keith M., Álvaro González-Vila, Mustehsan Beg, Francisco Vedreño-Santos, Zuansi Cai, Lourdes S. M. Alwis, and Keng Goh. 2023. "Individual Cell-Level Temperature Monitoring of a Lithium-Ion Battery Pack" *Sensors* 23, no. 9: 4306. https://doi.org/10.3390/s23094306

The research work associated with the PhD work listed below is being prepared for peer review.

- Proof of concept experimental investigation of copper plated foam for the enhancement of phase change material for the passive thermal management of Li-Ion battery.

Acknowledgements

First, I would like to thank my mother, without her support, generosity and understanding this thesis and many years of research work would not have been possible. I also want to thank my father, who couldn't be here to witness this endeavour through to the end. I appreciate you reminding me time and time again that if I put in the effort, I can do anything in life.

I especially want to thank Arthur Spry for the many hours of maths tutoring; without your help, I undoubtedly would not have started my academic journey all those years ago.

I would like to thank Dominic O'Rourke for all the support and advice in the chemistry lab, your insight and knowledge has been invaluable.

Thank you to Dr Álvaro González-Vila for helping fabricate the Fibre Bragg Grating sensors.

Finally, I would like to thank my academic supervisors, Keng, Paco and Zuansi for all your help, advice, and countless meetings over the past 5 years.

Table of Contents

List of Figures

List of Table

List of Abbreviations

2MBT	*2 - mercaptobenzothiozole*
BEV	Battery Electric Vehicle
BTMS	Battery Thermal Management System
C	Battery C-Rate
CC	Constant Current
Cu-EP	Electroplated Copper
Cu-P	Electroless Plated Copper
Cu-S	Solid Copper
CV	Constant Voltage
CW	Constant Power
DSC	Differential Scanning Calorimeter
EDTA	Ethylenediaminetetraacetic
EMF	Electromotive Force
EV	Electric Vehicle
FBG	Fibre Bragg Grating
FOS	Fibre Optic Sensor
GBP	Great British Pounds
HEV	Hybrid Electric Vehicle
LIB	Lithium-Ion Battery
Li-ion	Lithium-Ion
MEA	More Electric Aircraft
PCM	Phase Change Material
PT	Platinum Resistance Sensor
PTFE	Polytetrafluoroethylene
PU	Polyurethane
PVC	Poly Vinyl Chloride
RIM	Refractive Index Modulation
RTD	Resistance Temperature Device
SEI	Solid Electrolyte Interface
TC	Thermocouple Sensor
USD	United States Dollars

List of Units and Symbols

λ	*Measured Peak Wavelength*
λ_0	Reference Wavelength
λ_B	Refraction Wavelength
λ_e	PCM/Foam Composite Theoretical Thermal Conductivity
λ_{pcm}	Phase Change Material Thermal Conductivity
λ_{sk}	Foam Skeleton Thermal Conductivity
ΔT	Temperature Change (°C)
A	Amperes
A_c	Correlation Coefficient
E_{stored}	Energy Stored in PCM
I	Current
k	Temperature sensitivity
L_f	Latent Heat of Fusion
m	Mass
mA	Milliamperes
mAh	milliamp hours
m_{fo}	Metal Foam Mass
mg	Milligrams
mJ	Millijoules
n_{eff}	Effective Refraction Index
nm	Manometers
pm	Picometer
T	Temperature (°C)
V	Voltage
V_{CR}	Conversion Rate Voltage
V_{out}	Amplifier Output Voltage
V_t	Foam Volume
α	Thermal Expansion Coefficient of FOS Material
α_i	Foam Impregnation Ratio
α_s	Seebeck Coefficient
Δ_{mi}	Mass Difference of Foam and Foam/PCM Composite

ε_b	Bulk Porosity
ε_z	FBG Longitudinal Strain
η	Thermo-optic Coefficient
Λ_B	Period of Refraction Index
ρ_e	Photo-elastic Constant
ρ_{pcm}	Solid Phase Change Material Density
ρ_{sk}	Foam Skeleton Material Density
Ω	Ohms

Chapter 1: Introduction

1.1 Electrochemical Energy Storage: A Growing Demand

Electrochemical energy storage is rapidly becoming the default method for electrical energy storage across the globe, with many types of battery storage deployed in many different applications. Generally, batteries are of two types; primary batteries are used only once and cannot be recharged, due to the irreversible electrochemical reactions occurring in the batteries, whereas secondary batteries, or rechargeable batteries, are electrochemical batteries that can be cycled by discharging and recharging. Primary batteries hold the major part of the commercial battery market, however, there are challenges associated with the use of primary batteries, including the generation of large amounts of unrecyclable materials, and the toxic components in the batteries which create environmental concerns [1, 2].

A major secondary battery is the Lithium-Ion Battery (LIB), it has many advantages as the leading electrochemical storage device, with common characteristics such as high specific energy, high specific power, high conversion rate and long cycle life. It is widely used in electric vehicles and various energy storage devices due to its good electrochemical stability, high energy density, long battery life, and no need for maintenance [3].

The application of LIBs can generally be divided into five key fields: transportation, electric energy storage, mobile communication, new energy storage, and aerospace/military. Its application in electric vehicles could not only replace the reliance on oil with electricity and reduce greenhouse gas emissions but also store excess electricity from the grid [3]. As the demand for LIBs grows so does the market for the batteries, Figure 1.1-1 shows the market value for the LIB industry from 1992 to 2018, with predictive values for 2019 and 2020. The study conducted in 2019 by Zhenghai Liao et. al. shows that the world market value for LIBs was well over 25 billion USD in 2018 and was estimated to be over 35 billion USD in 2020. Current projections estimate the global market to grow from USD 41.1 billion in 2021 to USD 116 billion by 2030[4]. Specifically for electric vehicles, one estimate projects global sales of electric vehicles to climb from 1.7 million in 2020 to 26 million in 2030 [5].

Figure 1.1-1: Lithium-ion batteries' world market value from 1992 to 2020 [3].

With this in mind, the LIB will inevitably play a larger role in many sectors, one of these sectors is the power distribution grid. Countries and individuals require secure energy supplies; they need to know that sufficient and appropriate energy will reach them in the future; therefore, being in control of independent and assured supplies is essential – renewables energy generation technologies, such as solar, wind and tidal, can provide this with some caveats [6].

Traditionally, the production, transmission, distribution, and consumption of electric energy are simultaneous, i.e. the electricity produced by power plants at any moment must equal the sum of the power used by consumers and grid loss [7]. Arguably, this is where renewable energy generation technologies fail as fluctuating weather conditions can hinder the reliability of electrical output, hence the need for grid-scale electrical storage, i.e., battery storage. Grid-scale battery storage is an ongoing research area with some notable developments in recent years; for example, in 2017, the world's largest lithium-ion battery began distributing power into the electrical grid in South Australia.

The Tesla manufactured battery, rated at 100 megawatts was deployed to solve South Australia's electricity problems, such as the state-wide power shortage experienced in 2016. The battery, integrated within a wind farm, is run by French energy company Neoen and has the potential to store energy to power 30,000

homes for one hour; however, its primary purpose is to stabilise the existing electrical supply to the grid [8].

In 2017, the cost of one kilowatt-hour of lithium-ion battery energy storage was USD 100 [9]; compared to the most common grid-scale storage, hydro pump storage, battery storage can offer a substantial cost saving. For the UK national grid to fully cope with the transition to renewable energy, it will require approximately 100 gigawatts of energy storage, or ten hydropower stations the size of the Dinorwig station in Wales. The cost of 100 gigawatts of hydro storage based on the original 1984 cost of the Dinorwig power station, adjusted for inflation, would be estimated at £13.7 billion; comparably, the cost of battery storage equates to £7.8 billion, a substantial saving [9].

The transport sector is facing a shift toward electrification in the coming decades. Globally, fossil fuel-based transportation accounts for 14% of human-generated greenhouse gas emissions, resulting in a shift away from carbon-intensive transportation modes [10]. Countries such as France and the UK are to end sales of internal combustion-engine cars in favour of Electric Vehicles (EV) by 2040, whereas India plans to achieve this by 2030 [11]. In 2017 electric vehicle sales grew from 740,000 the previous year to 1.1 million, a 51% increase, reaching a market share of 1.7%. It is forecast there will be nearly 400 models of Electric Vehicles (EVs) and 25 million sales by 2025 [12]. Lithium-Ion Battery technology, typically used in Battery Electric Vehicles (BEVs), is prevalent in modern-day society as mobile phones, laptops and a plethora of other gadgets are relied upon on a day-to-day basis. The LIB is expected to play an ever-increasing role in more diverse ways with the advancement in battery technology. One example of this is the aviation industry; manufacturers are deviating towards More Electric Aircraft (MEA), replacing the conventional systems, typically non-propulsion systems, with electrical-based systems. As hydraulic and pneumatic emergency systems migrate to electrical equivalents, the onboard power demand increases; thus, MEA uses state-of-the-art LIB technology as these have higher energy density and lower weight [13].

Transport modes such as electric and hybrid buses, EVs, and MEA require medium-to-large scale LIB packs; thus, the safe operation of the LIB is pertinent to the successful deployment of large-scale applications. One main obstacle to this is the multitude of safety concerns when utilising LIBs [14-16]. The

environmental conditions and specific usage cases in which a LIB is operating can have a role in performance issues [12], [17]; therefore, the temperature, in particular, is considered a critical safety concern [14], [16], [18-22]. Thankfully there are many research avenues and institutions around the world working towards solving issues with the implementation of batteries.

1.2   Energy Storage Principles

The standard battery is typically referred to as a 'cell' which contains chemical energy which is converted into electrical energy. These cells are connected in a series and/or parallel configuration to form a battery pack. The connections are based on the battery's application; a connection in series adds the voltage and connecting in parallel adds the amperage. There are four main components of a battery, the positive electrode or 'cathode', the negative electrode or 'anode', the electrolyte, and the separator as shown in Figure 1.2-3. During the battery operation, a chemical reaction in both the anode and cathode results in electrons flowing between each side of the battery, as shown in Figure 1.2-3. The electrons can only flow using an external circuit; a separator in the cell stops the flow of electrons internally. The separator is the electrically insulating layer of material that physically separates electrodes of opposite polarity. The separator must be permeable to the electrolyte ions; modern separators are made from a synthetic polymer. The electrolyte is the medium that allows for the ionic conduction between the anode and cathode but, importantly, is a non-conductor for electrons as this would result in the self-discharge of the battery.

The positive electrode can be an oxide, sulphide or another compound that can be reduced during the discharge of the cell. The negative electrode is usually a metal or alloy capable of being oxidised. Both electrodes must be electrically conducting for electrons to flow via the external circuit [23].

In a typical Li-Ion cell, the negative electrode uses a technique called 'negative insertion host' where graphite or tin oxide is used. During charged status, the negative electrode contains lithium ions in its atomic structure, which are then passed back to the positive electrode through the organic electrolyte during discharge. The positive electrode is typically either manganese, cobalt, or nickel oxide. The reverse process occurs during the charging status.

Figure 1.2-3: Battery Cell Cross Section, showing heat generation($\dot{Q}$)[2]

Figure 1.2-3: Lithium-ion Battery Schematic (Adapted from [1]).

Figure 1.2-3: Battery cell types (a) pouch cel, (b) prismatic cell, and (c) cylindrical cell. (adapted from [23]).

Generally, there are three common types of battery cells, cylindrical, prismatic and pouch cells (Figure 1.2-3). Cylindrical and prismatic cells have higher structural integrity than pouch cells because of their sheet metal designed casing, however, they are also heavier. The casing is made of strong aluminium sheets, in contrast to the polymer cover of the pouch cell [24].

At present, BEVs are powered using Lithium-ion batteries as these offer a significant advantage over other battery types. Lithium is the lightest of all metals with an atomic mass of 6.94 and a specific capacity of 3.86 Ah g [1]. Comparing this to sodium used for sodium batteries with an atomic mass of 23 and a specific capacity of 1.165 Ah g [1], it is clear to see the advantages of utilising such metal for battery applications.

1.3   Thermal Monitoring and Management of Li-ion Batteries

The monitoring and management of thermal generation from a lithium-ion battery are pertinent to the longevity and functionality of the battery cell. High-temperature exposure and thermal generation from the cell can induce several degradation modes leading to reduced capacity and power fade. The temperature build-up is caused by the electrochemical processes within the LIB, during operation the heat generated from the entropy change is reversible, however, the heat generation which is caused by the charge transfer, ohmic loss and mass transfer limitations is irreversible [25], thus heat build-up occurs.

Figure 1.3-1 illustrates the cause and effect of battery degradation for lithium-ion batteries. High temperature can lead to solid electrolyte interface layer (SEI) growth, SEI decomposition, electrolyte decomposition and binder decomposition degradation mechanisms. These degradation mechanisms can lead to the three main degradation modes, which in turn result in capacity fade and power fade of the battery cell.

The three common modes of degradation are as follows;

1) Loss of lithium inventory: lithium ions are consumed by parasitic reactions, such as surface film formation, for example, SEI growth, decomposition reactions, and lithium plating and are no longer available for cycling between the positive and negative electrode, leading to capacity fade. Surface films may also cause power fade. Lithium ions can also be lost if they are trapped inside electrically isolated particles of active materials [26].

2) Loss of active material of the negative electrode: active mass of the negative electrode (anode) is no longer available for the insertion of lithium due to particle cracking and loss of electrical contact or blocking of active sites by resistive surface layers. These processes can lead to both capacity and power fade [26].

3) Loss of active material of the positive electrode: active mass of the positive electrode (cathode) is no longer available for the insertion of lithium due to structural disordering, particle cracking or loss of electrical contact. These processes can lead to both capacity and power fade [26].

Thermal management of lithium-ion cells is a challenge facing electric vehicle manufacturers. The excessive local temperature rise in Li-ion cells causes reductions in cycle life and may lead to thermal runaway of individual cells or an entire battery pack [27]. The charging efficiency and lifecycle will be reduced if operating temperatures are above 50 °C. For temperatures above 100 °C, which can be either caused by overcharging or internal short-circuiting, thermal

Figure 1.3-1: Cause and effect of degradation mechanisms and associated degradation modes [25].

runaway may occur [28]. Temperature not only affects the life cycle of a battery pack; it can also affect aspects such as charge acceptance, energy capability and reliability [27].

Li-ion battery packs tend to be more compact and lighter compared to the NiMH equivalents found in hybrid electric vehicles (HEVs). The battery pack thermal management needs to be carefully considered in the lithium-ion battery module design to guarantee the temperature of batteries in operation within a narrow optimal range of 25-40 °C under standard power/current loads and ambient temperature conditions [29]. However, stressful conditions such as high-power draw at high cell/ambient temperatures, as well as defects in individual cells, can significantly increase heat generation [30, 31].

There are generally two broad forms of cooling systems known as 'passive' and 'active'. An active cooling system uses blowers for air cooling or liquid flow distributors to remove the heat generation of the batteries. A passive solution doesn't use such devices and often incorporates phase change materials (PCM) or heat pipes to remove heat [27].

1.4   Aims and Objectives

This thesis aims to investigate the thermal monitoring and thermal management of lithium-ion batteries with a twofold approach. Firstly, the implementation of Fibre Optic Sensors (FOS) with multiple Fibre Bragg Gratings (FBGs) for the multiplexing measurement of a lithium-ion battery pack temperature at the individual cell level, pursuing the enhancement of information available for a theoretical battery management system (BMS).

Secondly, conduct an experiment-based 'proof of concept' for the novel application of copper electroless deposition onto polyurethane foam for the enhancement of phase change material (PCM). Implementing a passive thermal management system for lithium-ion batteries.

To achieve this aim, the following research objectives have been set:

- To investigate the mounting method of the FOS on the LIB surface for reliable temperature measurement.
- Develop a system to measure the surface temperature of a lithium-ion battery pack with one FOS strand demonstrating individual cell level monitoring.
- Assess the reliability and accuracy of the developed mounting method for individual cell level monitoring.

- Develop a method for the implementation of foam structures into PCM for the thermal management of a Lithium-ion battery.
- Investigate the method for copper electroless plating of polymer structures for use in PCM material. Implement this to conduct a 'Proof of concept' for the thermal management of lithium batteries.

1.5 Hypothesis and Contribution

The hypothesis of this thesis is twofold, where (i) the individual cell level monitoring of a LIB can be achieved by implementing a multiplexing FOS scheme of FBGs on cylindrical cells, and (ii), the use of copper plated foam is comparable to the conventional commercially available copper foams, resulting in a thermal management system component which is effective and uses less copper material resulting in cost saving overall.

The literature review in chapter two provides evidence of a gap concerning individual cell level monitoring of LIBs using FBGs, additionally, it shows that there is currently no known implementation of copper deposition onto polymer foam structures for the use in passive battery thermal management systems.

The main contributions of this thesis are the following:

- Development of a new 'guide tube' method for the mounting of a FOS strand onto a LIB and assessing its suitability for the measurement of battery surface temperature.
- Further development of the 'guide tube' method for individual cell monitoring of a lithium-ion battery pack containing multiple LIB cells.
- The novel implementation of copper deposition on polymer foam structures for use in a phase change material-based passive battery thermal management system. Focus on the 'proof of concept' of this application and the influence of the electroless copper deposition mass on the ability of the system to lower battery surface temperature.

1.6 Thesis Outline

This thesis is organised as follows:

Chapter 1 presents the motivation, objectives and contribution of this research work.

Chapter 2 reviews the literature relating to the temperature measurement of LIBs, with a section devoted to the use of FBGs for this application. Additionally, a literature review of methods for battery thermal management is conducted, with a focus on foam/PCM composites.

Chapter 3 presents the methodology and results of a proof-of-concept experimental study on the guide tube mounting method of a FOS strand with 5 FBG sensors. A single LIB cell is used to evaluate two mounting methods.

Chapter 4 applied an enhanced guide tube method of mounting the FOS strand on a three-cell LIB pack and deploys the five FBGs for individual cell level monitoring. The method's suitability is evaluated and compared to industry standards for temperature measurement.

Chapter 5 discusses the manufacturing methodology of copper-plated foam for the impregnation of PCM material. The copper foam PCM composites are then utilised for the thermal management of a pouch cell LIB. Laboratory experiments show different masses of copper plating on the foam structures and compare this to the commercially available copper foam of much greater mass. The experimental results are summarised, and conclusions are made regarding the performance of the copper-plated foam.

Chapter 6 finalises this thesis by presenting a summary of the results and a discussion of future work.

Chapter 2: Literature review

2.1 Introduction

This chapter presents a review of the fundamentals of contact-type temperature measurement techniques and their applications in the peer-reviewed literature. Additionally, the fundamentals of the battery thermal management system (BTMS) and examples of their applications in the peer-reviewed literature.

2.2 Temperature Sensing Techniques

There are several types of thermal sensing devices which use several techniques to obtain a reliable temperature change. This section outlines the most common techniques used for contact-type temperature measurement where a sensor is physically placed onto a surface. These are categorised into three main classes, i.e., a thermo-resistive sensor which can be classified into the thermally sensitive resistor (thermistor) and resistance temperature detector (RTD), thermocouple, and the optical Fibre Bragg Grating (FBG) sensor [25].

2.2.1 Thermocouples

The Thermocouple sensor (TC) is a standard method of sensing temperature, widely viewed as an industrial standard and extensively utilised in many industrial processes [25].

Consisting of two conductors of different metal types welded to create a sensing tip; the principle of operation is based on the 'Seebeck' or thermoelectric effect discovered by Thomas Seebeck in 1821. The thermoelectric effect describes the small voltage change experienced when the welded and the reference end of the TC sensor cable are exposed to different temperature points, and hence a thermoelectric Electromotive Force (EMF) is developed which can be measured, for example, with a voltmeter [32, 33].

The simply joining of two dissimilar conductors with a large relative Seebeck coefficient will induce a potential difference (Figure 2.2-1). The materials also have large electrical conductivities and small thermal ones, so there is a relatively low voltage drop across the length and a small thermal gradient.

This generated voltage, (V) is the Seebeck voltage and is related to the difference in temperature (ΔT) between the heated junction and the open

junction by a proportionality factor (α_s) called the Seebeck coefficient. As described in (1), where the value for α_s is dependent on the types of material at the junction.

$$V = \alpha_s \Delta T \tag{1}$$

Figure 2.2-1: Thermocouple Construction [33]

2.2.2 Thermo-resistive Sensors

The resistance of metals is dependent on the temperature, this is the basis of thermo-resistive sensors. The most common types of thermo-resistive sensors are discussed along with some of their applications.

2.2.2.1 Thermistor

The thermistors are typically solid semiconductors whose electrical resistance is highly responsive to the surrounding temperature, and share many merits, including low cost, high sensitivity to the temperature, wide measurement range ($-55\,°C$ to $300\,°C$), and small size [25]. The thermistor is one of the most widely used temperature sensors for commercially available battery systems, such as those used by the Toyota Prius and Honda Civic Hybrid [34].

The NTC thermistor or, Negative Temperature Coefficient thermistor will see a decreasing resistance (R) as temperature (t) increases. The resistance changes exponentially as defined in (2), where x and y are constants for the material the thermistor is made from.

$$R = xe^{y/t} \tag{2}$$

The thermistor is seen in the literature for battery surface temperature measurement applications and many applications for monitoring the surface temperature to study thermal behaviour. For example in [35] the temperature on the surfaces of a LIB cell was recorded using thermistors. The sensors were placed in the middle of the 18650 cylindrical LIB between the negative and positive connections and had an error range of ±1 °C. Additionally, M. Debert et.al. presents a model of heat transfers in a battery module and uses a mass produced thermistor as one element of data gathering on a specially equipped battery module for model parameter identification [36].

2.2.2.2 Resistance Temperature Detector

The resistance temperature detector (RTD) measurement makes use of metallic conductors with their electric resistance sensitive to temperature. The platinum resistance sensor is most widely used due to the high-temperature resistance linearity, high precision, ±0.2 °C in industrial applications, wide temperature range, − 260 to 960 °C, and reasonable stability in the environment [25].

RTDs have also been frequently used for LIB surface temperature measurement. Particularly, commercial PT100 RTDs have been reported widely for LIB surface temperature measurement.

An electro-thermal model of a stack of three lithium-ion batteries for automotive applications is proposed in [37], where the thermal behaviour is validated using RTD PT100 class A sensors attached to the battery surface and can capture the surface temperature from -73 °C to 260 °C. Additionally, Tippmann et. al. utilise six PT100 sensors to measure the temperature profile of a high-energy Li-ion cell to aid in the development of an electrochemical model to help understand internal processes and predict ageing effects at low-temperature high discharge conditions [38].

D. Chalise et. al. present an experimentally-validated analytical method to rapidly and accurately predict the temperature of a LIB cell undergoing cyclic charge and discharge [39]. Using INR18650-15L Samsung LIB cells, it is stated that the temperature of each cell is monitored using a PT-100 temperature sensor attached to one of the cells, the sensor is configured in a four-wire circuit for improved measurement accuracy. The obtained temperature profiles as functions of time are used to validate the theoretical model [39].

It is seen in the literature that a common type of PT sensor is the PT100 sensor which means at 0 °C the resistance of the sensor is 100 Ω [40]. These sensors are subcategorised into classifications. Sensor manufacturers offer a wide range of sensors that comply with BS1904 class B (DIN 43760): these sensors offer accuracy of ±0.3 °C at 0 °C and ±0.8 °C at 100 °C, or for increased accuracy, BS1904 class A (±0.15 °C) and tenth-DIN sensors (±0.03 °C), additionally, manufacturers such as Isotech can provide standards with 0.001 °C accuracies [41, 42].

2.2.3 Fibre Optic Sensors and Fibre Bragg Gratings

The fibre optic cable or strand is typically defined by two types, single mode and multimode. Single mode uses only one mode of propagation i.e., a single wavelength of light in the fibre core resulting in no overlap between the different wavelengths of light like there is with multimode fibres, typically FBGs are inscribed into single mode fibres. Shown in Figure 2.2-2 the single-mode fibre realigns the light toward the centre of the core, whereas multimode fibres simply bounce the light off the edge of the core.
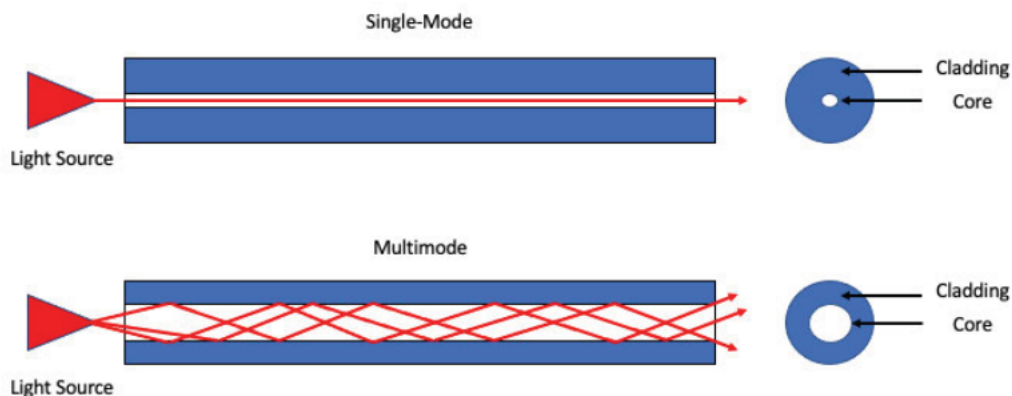
Figure 2.2-2: Single and multimode Fibre.

Fibre Bragg Grating (FBG) is a periodic modulation of the index of refraction in the single mode fibre core [43]. As uniform fibre gratings, the grating planes are perpendicular to the longitudinal direction of the fibre and are arranged in constant periodicity, which is the basic structure of Bragg grating, as shown in Figure 2.2-3. When incident light is emitted and guided along the fibre core, it is reflected on each grating plane. When the Bragg condition is satisfied, the waves reflected by each grating plane are superimposed to form a reflection

wavelength peak. According to the Bragg conditions, one Bragg wavelength λ_B is given by (3) [44, 45].

$$\lambda_B = 2n_{eff}\Lambda_B \qquad (3)$$

Where n_{eff} is the effective refraction index of the fibre core, Λ_B is the period of refraction index modulated as well as grating spacing. Any change of n_{eff} or Λ_B causes a variation in the centre of the reflection wavelength λ_B [25, 44]. The longitudinal deformation caused by the external force will change n_{eff} due to the photo-elastic effect, and further change Λ_B due to the changing pitch, thus it is possible to detect strain. Similarly, the temperature change also leads to the variation of n_{eff} and Λ_B due to the thermo-optical effect and thermal dilation [25, 44].

Figure 2.2-3 Working principle of the fiber bragg grating sensor [24].

An optical interrogator is used at one end of the fibre, this device detects the reflected wavelength frequencies while simultaneously providing the light source. When the fibre expands, contracts or the FBG bends, the grating distance between Braggs (Λ) and the refractive index (n) of the FBG elements change [46].

As the FBG sensor can measure the temperature and strain simultaneously, and the two variables are coupled together intrinsically needing specially-designed decoupling approaches [25].

The sensitivity of the Bragg wavelength with temperature and strain is as follows.

$$\frac{\Delta \lambda_B}{\lambda_B} = (1 - \rho_e)\varepsilon_Z + (\alpha + \eta)\Delta T \qquad (4)$$

Where α is the thermal expansion of the FOS material (typically silica), η is the thermo-optic coefficient, which represents the temperature dependency of the refractive index, ρ_e is the photo-elastic coefficient, and ε_z is the longitudinal strain of the grating.

Equation 4 shows that the Bragg displacement is a function of strain and temperature thus, by observing only $\Delta \lambda_B$ it is not possible to determine if the displacement is due to strain, temperature, or both. To measure only temperature, the FBG must be protected against strain, however, to measure strain, it is very difficult to stop local temperature variation from interacting with the FBG [44].

$$\frac{\Delta \lambda_B}{\lambda_B} = (\alpha + \eta)\Delta T \qquad (5)$$

To measure strain only, compensation for the localised temperature must be made. To do this, the measurement of the local temperature using a thermistor or thermocouple must be made and applied to (5), to calculate the effect of temperature alone in the Bragg wavelength displacement. Then, the displacement of the Bragg wavelength due to strain alone is the total displacement observed minus the displacement due to temperature alone [44].

The most common method for decoupling strain and temperature, to obtain temperature is the mechanical method, with the use of microtubing, this allows for the expansion and contraction of the FOS strand due to temperature without inducing strain on the FBG sensors [25, 44, 47, 48].

There have been several notable examples of strain, pressure and temperature decoupling using microtubing in the literature, for example, Dan L. Romanyk et.al use FBG sensors to measure the temperature and strain of resin-based composites, commonly used in dental restoration. They measured the strain and temperature of their resin-based composites with and without polyimide tubing, resulting in larger strain in the non-tubing covered FBGs, said to be a result of thermal volumetric expansion of the resin composites [49].

Lihui Liu et. al. develops an FBG pressure sensor partly shielded with a metal tube. It is said that the thermal-strain cross effect is avoided, and its pressure sensitivity is increased to 1200 times that of bare fibre grating. It is concluded that due to its good sensing linearity the sensor can be applied for the measurement of hydraulic pressure and vibration [50].

C.-H. Lee et. al. enhances the temperature sensitivity of an FBG temperature sensor using a copper tube to jacket the FBG. In the setup, both sides of the FBG are glued with epoxy to cylindrical tubes that in turn are inserted and glued to a cylindrical copper tube. As the high thermal expansion coefficient of the cylindrical copper tube pulls both sides of the FBG, the temperature sensitivity is improved threefold when compared to a bare FBG [51].

An all-fibre seawater temperature and depth sensing array is proposed by Li Wang et. al., used to obtain seawater temperature and depth profiles in the yellow sea of China. The FBGs were coated with a layer of silica gel and were then encapsulated in a metal tube, successfully preventing the influence of pressure on the FBG sensors [52].

It is clear from the literature that it is important to employ a method to mechanically decouple strain and temperature when using FBG sensors for thermal monitoring, it is also shown that FBG is deployed in a multitude of scenarios and has wide application in both temperature, pressure, and strain measurement.

2.2.4 Battery Thermal Monitoring with FBG sensors

It is said that fibre optic sensor methods are expected to be one of the most prominent methods for obtaining battery parameters, particularly because of the multiplexing capabilities associated with fibre optics, where it is possible to obtain multiple measurements from a single FOS strand [43, 45].

There are many examples of battery surface temperature measurements using the FBG sensor in the literature, where it is seen that the research mostly employs tubing of some form to decouple the strain and temperature measurements.

E. Vergori and Y. Yu utilise a Polytetrafluoroethylene (PTFE) tube to constrain the FBG sensors on the surface of a 5 Ah A5-sized pouch cell, successfully

decoupling strain and temperature to measure both parameters during three different C rate discharge conditions and three ambient temperature conditions. They find that the deployed sensor can demonstrate successful recording of these parameters [53].

Yifei Yu et al. also employs a PTFE tube to decouple strain and temperature when using FBG sensors on the surface of a LIB. As shown in Figure 2.2-4 the five-meter-long FOS with FBGs is attached to the A5 LIB cell and eight TC sensors using a PicoLog data logger are used to validate the FBG response.

Figure 2.2-4: FOS Strand on A5 pouch cell with thermocouples [52].

The authors state that the FOS was calibrated in an ESPEC thermal chamber and a thermal fluctuation was induced from 5 °C to 55 °C at 10 °C increments, at each incremental step the chamber was allowed to reach thermal equilibrium, then 100 measurements were recorded, and the arithmetic mean was taken for the wavelength shift. The authors find that the FOS is comparable to the temperature response of the TC sensors through 1 C, 3C and 5 C discharge conditions [54].

The electrode temperature was measured using an aluminium metal ring and FBG sensors in [55], where the temperature response of the FBGs was compared to a PT100 sensor located near the loosely attached FBGs. The metal ring with FBG and PT sensors is attached to the terminals of 60 Ah 3.2 V lithium iron phosphate cells, the setup shown in Figure 2.2-5 . The sensors are

calibrated at a temperature fluctuation from 10 °C to 80 °C in a thermostatic bath and show that the FBG sensors show good linear response. A multitude of testing at various C rates ranging from 0.3C to 0.6C showed a cell temperature change ranging from 1.5 °C to 6.5 °C. It is concluded that the method proposed for detecting external electrode temperature is successful, showing good agreement with the adjacent PT100 sensors.

The internal temperature of a LIB is recorded using the FBG method in [56, 57], where in both cases a single-mode SMF-28 fibre with FBGs inscribed was used to measure the internal temperature of a cylindrical LIB cell. In [56] it is found that the insertion of the FBG sensor into the cell provides unprecedented cell data, whereas in [57] it is found that with the use of K-type thermocouples on the outside of the cell, the variation in temperature between the inside and outside of the cell can reach up to 6 °C in the scenarios tested.

S. Novais et al. measure the internal and external temperature of an in-house manufactured LIB pouch cell of less than 1mm thickness. Using a Micron Optics SM-125 optical interrogator, they measure the temperature of the cell using parallel laid FBG sensors both internally at the separator and externally on the LIB surface. The authors state that as the LIB cell is less than 1mm thick they can neglect any strain induced on the FBG and only record temperature from the FOS. The approach uses the same method for calibration as seen in other research works, where the sensor is exposed to a temperature fluctuation, in this case, 10 °C to 35 °C at 5 °C intervals. It is concluded that the FBG sensors are successfully integrated into the LIB cell and can detect accurate temperature measurements at C rates ranging from 1 C to 8 C. Furthermore, it is stated that the cell internal temperature increases as much as 4.7 °C which is an important insight that should be taken into account for battery management systems and battery modelling [58].

The FBG sensor is also used to measure the strain and temperature of coin cells in [20], where the FBG signals were acquired using a Micron Optics interrogator and the ENLIGHT software used to translate the strain and temperature experienced by the FBGs. It is found in the study that the FBGs show stable strain response and the temperature measured was 10 °C higher internally compared to the external temperature.

Although the FOS and FBG scheme inherently has good multiplexing capabilities, there are limited instances where distributed temperature measurements over multiple LIB cells are explored, [53] discuss the measurement of two LIB pouch cells with the same 5-meter-long FOS strand with FBGs, utilising PTFE tubing in select areas to decouple strain and temperature. The authors state that knowing the temperature distribution of the cells and between the cells is fundamental to guaranteeing a good state of health and safety of the battery. On the other hand, J.Mayer et.al. utilises 96 FBGs over fourteen multiplexed FOS strands to measure the distributed
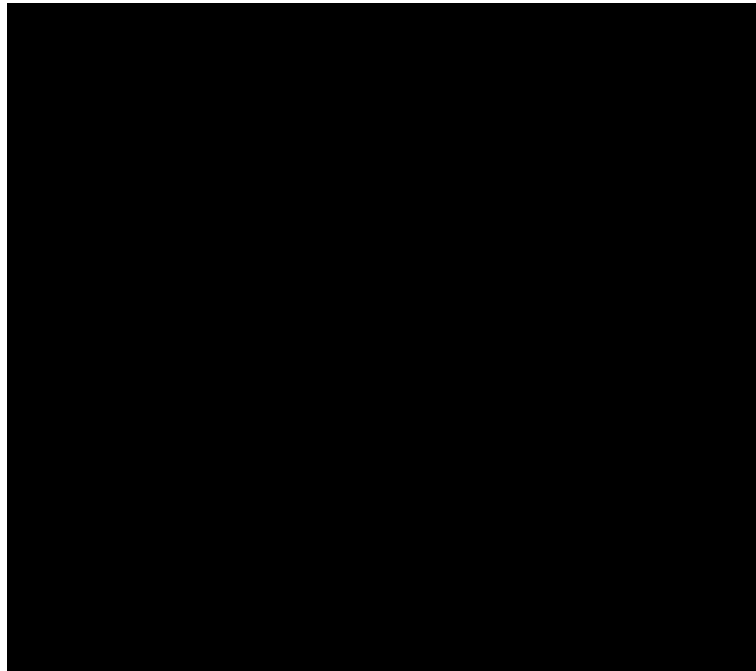
Figure 2.2-5: Schemating of experimental setup for temperature monitoring of a Lithium iron phospahate lib cell [53].

temperature of a 13.8 kWh electric vehicle battery pack. Using the setup to measure the effects of thermal runaway of the battery pack, the temperature rise was recorded at 477 °C [15].

It is clear from the literature that the use of FBGs for temperature measurement is an area of great interest where many researchers have successfully utilised the sensing method for the measurement of a single LIB cell, in limited cases multiple measurements across multiple LIB cells.

2.3 Battery Thermal Management

As mentioned previously, the battery thermal management system (BTMS) is very important for the reliable use of a LIB. The management of temperature

gradients is beneficial to the safety and longevity of LIBs, thus the BTMS plays a critical role in achieving sufficient temperature control [59]. It is said that temperatures above 50 °C can lower the charge efficiency and lower the longevity prospects of the LIB [60]. Moreover, the discharge of a LIB at higher C rates is shown to increase the battery surface temperature significantly, for example in [61] a 20 Ah Lithium-ion phosphate (LiFePO$_4$) is discharged at 4C resulting in a cell temperature of 58.1 °C.

Moreover, Panasonic NCR18650B cylindrical batteries are discharged in [59] using a configuration of nine cells connected in a series. The baseline of this study, where the cells were not cooled showed a temperature of 59.1 °C at the end of a 5 A constant current discharge.

Air, liquid and PCMs are the three most common cooling media for the BTMS [62]. This section will discuss these methods concerning the defined terminology, active and passive.

2.3.1 Active Thermal Management Systems

Active cooling typically refers to the use of a cooling medium with a powered component to actively remove heat gradients from the LIB cell or pack. This generally refers to the use of air or liquid heat transfer mediums, where fans or water pumps are used to move the heat transfer medium over the battery and remove excess heat generation.

2.3.1.1 Air Cooling

Rui Zhao et. al. explore a BTMS for a nine-cell Panasonic NCR18650B LIB pack using air and direct evaporative cooling. The battery pack under testing is placed in the centre of a specifically manufactured wind tunnel, and K-type thermocouples are taped to the battery surface for temperature measurement. Three cooling systems, natural convection cooling (baseline), forced air cooling, and direct evaporative cooling is applied to the batteries during tests [59].

In the baseline condition, the battery pack experienced a dramatic temperature increase with the temperatures peaking at 80.2 °C during 5 A discharge. It is said that in the forced air-cooling systems, a significantly lower temperature was achieved. The authors then deployed direct evaporative cooling which showed

a further enhanced cooling performance compared to air cooling due to the lower intake air temperatures, which was achieved by the absorption of the sensible heat of air during a water evaporation process. Additionally, it is said that cycle test results indicated that the battery equipped with direct evaporative cooling has improved long-term performance, with less capacity loss than the batteries cycled in baseline and air cooling conditions [59].

In [63] the authors tested an air-cooled module that contains prismatic lithium-ion cells operating under an aggressive driving profile. It is found that lowering the gap spacing between the LIB cells and/or the higher flow rate of the cooling fan leads to a decrease in the maximum temperature. Additionally, it is found that for the LIB module, operating with a uniform cell gap of 3 mm and an airflow rate of 40.8 m^3h^{-1} is the best choice when considering the fan power, maximum temperature rise and temperature uniformity.

Highlighted in [63] is the requirement of power to the cooling fan to produce adequate forced air cooling, in systems such as electric vehicles the power for the cooling system must come from the main traction battery, which can be seen as a drawback to such cooling methods, additionally the poor heat capacity and low thermal conductivity of air can be seen as insufficient [64].

However, considering the simplicity and low cost of the air-based BTMS, it is favoured by some Chinese and Japanese EV manufacturers with air-based systems used in popular EV models such as BYD E6, Toyota Prius, and Nissan Leaf. These systems typically use several fans to direct air to cool the cells with airflow over the cell surface [64].

2.3.1.2 Liquid Cooling

For liquid cooling BTMS, the heat is carried by convection and conduction from the battery cells to the coolant via cooling channels. The coolant is usually water and Ethylene glycol solution, which typically provide a wide operation temperature range from −40 °C to 105 °C. With the high thermal conductivity of liquid coolants, BTMSs have both higher cooling capacity and cooling efficiency than other systems [62].

Typically, there are two forms of liquid cooling, indirect and direct, in the direct scenario the cooling liquid is directly passed over the cell surface to remove the heat generation, this poses some issues such as the possibility of electrical

shorts. Due to this EV manufacturers such as Tesla and General Motors favour indirect cooling, where a mixture of water and ethylene glycol is normally used as a heat transfer medium via tubes, cooling channels, fins or jackets [64].

There is a large interest in the development of liquid cooling for LIBs, which can be seen in the literature. For example, A. Ibrahim et.al. construct a compact lightweight serpentine wavy channel indirect liquid cooling system for a battery module of cylindrical Li-ion cells. The authors find the system can cool the system maintaining the module temperature within appropriate working conditions for electric vehicle applications i.e. below 50 °C [65].

In [66] the authors cool a pouch cell using the cold plate method, shown in Figure 2.3-1. The water-cooled cold plates are used to remove heat from the cell under various discharge rates ranging from 1 C to 5 C. The authors conduct experiments at different water flow rates and different coolant inlet temperatures from 15 to 35 °C. Their results show that lower coolant inlet temperature causes the largest maximum temperature difference on the battery surface. Comparing a mini-channel cold plate to a serpentine cold palate resulted in a 5.7 °C reduction of maximum average battery surface temperature, additionally, battery surface temperature homogeneity was improved up to 40% with the mini-channel cold plate.
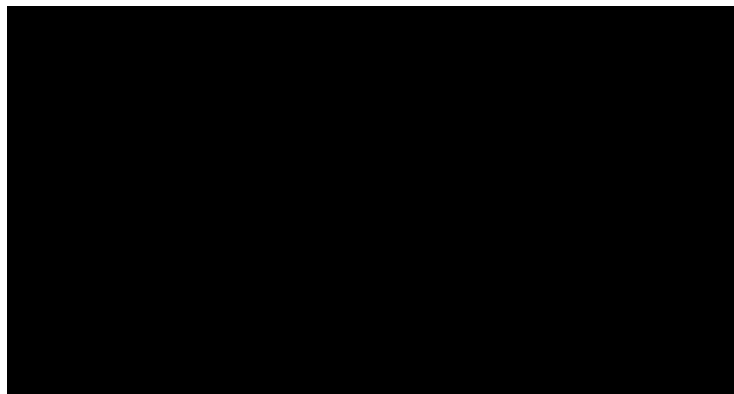
Figure 2.3-1: Exploded view of the cold plate cooling method (adapted from [64]).

Direct liquid immersion cooling systems fully immersed the battery cells in a dielectric heat transfer fluid (dielectric coolant). The dielectric coolant is circulated with a pump providing a constant flow of dielectric coolant to ensure continuous contact with all the cell walls, tabs, and electrical wiring within the battery module. The flow of dielectric coolant absorbs the heat generated by the

cells through direct conduction and is circulated to a device such as a heat exchanger to transfer the heat energy to the environment [67].

D W. Sundin and S. Sponholtz subjected Samsung 286S battery cells to multiple rapid charge-discharge cycles while being cooled with forced air and by immersion in a dielectric AmpCool AC-100 coolant. Comparing those that were cooled with forced air, the dielectric coolant maintained an average cell temperature of 22.5 °C with a very low deviation from the mean, the forced air average cell temperature was 28.7 °C, with much greater temperature variation during charge/discharge. The dielectric immersion cooling method is also said to keep the LIB cells within the desired temperature range at higher discharge rates, concluding that this method is an attractive method for stationary battery systems.

While liquid cooling, in its multiple configurations is effective at cooling LIBs, there are some drawbacks of this form of BTMSs, for example, the high electric conductivity of water-based coolant requires the complete sealing of the whole BTMS. This is critical to the safety of the system as the normal operating voltage of electric motors in electric drive trains is typically around 400V, thus if the conductive coolant is leaked through the cooling channel into the electric motor or even into the vehicle cabin, the consequences could include, short circuit, engine or power module failures, fire, or even casualties to the driver and passengers [62]. Additionally, an active cooling system such as liquid cooling consumes extra energy due to the additional water pump, reducing the total mileage of EVs or HEVs [62]. For these reasons, there is ongoing research devoted to the development of passive thermal management systems.

2.3.2 Passive Thermal Management Systems

A passive thermal management system is a system which does not implement an active element such as fans, blowers or pumps to aid the heat transfer. Many of these passive systems make use of Phase Change Material (PCM) to absorb heat generation [27]. This section will review the most prominent thermal management systems utilising PCM as a heat storage medium.

2.3.2.1 Phase Change Material

The phase change material is a material which undergoes a melt-solidification cycle (solid-liquid phase transition), during this transition the material absorbs energy from its surroundings while maintaining a nearly constant temperature At the atomic level when transitioning from solid to liquid, when at melt temperature, the atomic bonds loosen which allows for the liquid transition [68]. The energy released or absorbed during the phase transition is known as the latent heat of fusion.

As shown in Figure 2.3-2, when heating a phase change material the sensible

Figure 2.3-2: Standard heating curve [66].

heat of solid will act to raise the material temperature until the transition temperature is reached, also known as the melt temperature, then the material will absorb energy at a constant temperature until the solid to liquid phase transition has complete (the latent heat of fusion), then sensible heat of liquid will continue to raise the material temperature to the latent heat of vaporisation, where the material will change state again, transitioning to a vapour. Beyond this point, the sensible heat of vapour will act to superheat the material.

For battery thermal management systems adopting PCM material, the systems will only utilise latent heat of fusion, as transitioning to the latent heat of vapour sees a large density change when the transition occurs, additionally, equipment such as boilers and condensers are required, adding complexity.

Generally, the energy stored in a mass of PCM material is defined in **Error! Reference source not found.**;

$$E_{Stored} = mL_f$$

(6)

Where m is the mass of the PCM material and L_f is the latent heat of fusion of the material.

Figure 2.3-3 shows the three main divisional groups of PCMs: organic (paraffin, non-paraffin compounds such as fatty acids), inorganic (salt hydrates, metallics) and their eutectic mixtures [69, 70]. Eutectic mixtures, a combination of two PCM compounds, will typically have a lower melting point than any constitutive compounds which make up the mixture [70].

Figure 2.3-3: PCM composition classification [68].

PCM for battery applications has been widely reported in the literature, typically using organic paraffin compounds The first instance of PCM for thermal management of LIBs is presented by Khateeb et. al. who demonstrates successfully a passive thermal management system, capable of replacing conventional thermal management system for Li-ion batteries in EV and electric scooter applications. Since this initial publication in 2004, there has been a multitude of works detailing the use of PCM for battery thermal management [71].

A. Mills and S. Al-Hallaj designed and simulated a PCM passive thermal management system for a li-ion laptop battery pack. The heat generation rate for a commercial 18650 2.2 Ah Li-ion battery was experimentally measured for various constant power discharges. Simulation of the six-cell LIB battery pack shows that safe operation of the battery pack during the most extreme case

requires the volume of the battery pack to be almost doubled to fit sufficient PCM [72].

In [73], the thermal management of battery modules with PCMs is investigated experimentally. An electric heater is used to simulate the heat source of a battery cell. Two different PCM designs are investigated: one with a PCM

Figure 2.3-4: Experiment configuration for PCM and two heater configuraitons [71].

cylinder surrounding the heater, and the other with PCM jackets wrapping the heater, as shown in Figure 2.3-4. It was shown that both designs are effective in maintaining the heater temperature, simulating the effects of a LIB.

In [74] a systematic investigation of PCM is conducted which considers the PCM thickness around cylindrical Samsung cells. The Samsung 18650-13L LIB cell with a capacity of 1300 mAh is surrounded by 5, 10 and 15 mm of PCM, with the temperature of the battery cell recorded using K-type thermocouples, the setup shown in Figure 2.3-6.

Figure 2.3-6: Single battery cell surrounded by varaible PCM layer thickness [72].

Figure 2.3-6: Maximum temperature difference with varying PCM thickness [72].

It is found by the authors that the PCM presents an apparent cooling effect reducing the maximum temperature of the battery to 30.3 °C, which is approximately 8 °C lower than without PCM. It is found that the temperature of the LIB with 5 mm PCM is higher than that with 10 mm PCM because of the increased heat storage capability associated with a thicker PCM layer. When further increasing the thickness to 15 mm it is found that the temperature is decreased contrarily. The authors then go on to conduct further experiments

varying the PCM thickness to obtain the optimum thickness. As shown in Figure 2.3-6, the research shows that the optimum PCM thickness is 10 mm.

Z. Ling et. al. discuss the combination of PCM and forced air cooling, creating a hybrid cooling system [75]. The temperature in a battery pack operating continuously is found to overrun the safety limit of 60 °C after two cycles with a discharge rate of 1.5 C and 2 C. The proposed hybrid system in the study integrates PCMs with forced air convection. It is discussed that the hybrid system successfully prevents heat accumulation and maintains the maximum temperature under 50 °C in all cycles. When considering airspeed the authors find that thermo-physical properties of PCMs dictate the maximum temperature rise and temperature uniformity in the battery pack, while forced air convection plays a critical role in recovering the thermal energy storage capacity of PCMs [75].

G. Kim et. al. analyse the suitability of PCM for battery thermal management in Hybrid Electric Vehicle (HEV) and Plug-in Hybrid Electric Vehicle (PHEV) systems [76]. A prototype PCM/graphite matrix module was evaluated experimentally under vehicle-based drive cycles. A twenty-cell 18650 LIB with five parallel by four series cell strings were used to experimentally test the porous graphite matrix, impregnated with PCM. The matrix acts like a sponge and provides a means of enhanced thermal conduction into the PCM wax, which provides structure and heat dissipation. The results were used to validate a thermal model. The model used to evaluate the benefits and limitations of PCM thermal management suggests that PCM can limit the peak temperature benefit for vehicle applications [76].

PCM has seen further adoption for individual battery components, for example in [77] PCM has been used in a separator material to develop a thermoregulating separator for LIBs. The authors develop a separator with a paraffin wax PCM which is encapsulated in hollow polyacrylonitrile (PAN) nanofibers (Figure 2.3-7). It is concluded that the PCM-based separator can efficiently suppress the enhanced temperature of batteries under abusive conditions, as found from a nail penetration test, additionally, the temperature-induced phase transition of paraffin allowed the phase-change separator to absorb a large amount of heat from an internal short-circuit. It is also said that

Figure 2.3-7: Schematic structure of the thermoregulating separator [77].

the electrochemical performance of the PCM-based separator outperformed a commercially available separator.

The main disadvantage of most solid-liquid PCMs is their relatively lower thermal conductivity, leading to excessive heat accumulations during normal or aggressive operations, and cycling operations. It is reported in [76] that the overall battery thermal management solution must rely on active cooling or limiting the battery's power output to avoid high temperatures during continuous cycling, due to the inability to remove the heat build-up in the PCM material.

Additionally, in extreme weather such as hot summers or geographical locations such as desert regions, the melted PCMs might become heat insulation materials due to their low thermal conductivities [62]. Due to this, research has adopted the use of foam materials to enhance the thermal conductivity of the PCM materials, this is discussed in the next section, with a focus on applications for battery thermal management.

2.3.2.2 Foam and Phase Change Material Composites

Metal foams, due to their combination of physical and mechanical properties, are used in many applications ranging from energy and blast resistance, fire resistance, thermal insulation, vibration, and sound dampening as well as lightweight applications such as foam core sandwich panels [78-81].

Foams are generally described as the uniform dispersion of gas bubbles in a liquid or solid, solid foams are when the liquid solidifies, thus creating a matrix structure [78, 82].

Metal foam is a cellular structure consisting of solid metal or an alloy containing a large volume fraction of fine gas-bubble pores. The pores in the foam are also called cells and they are of two types, open or closed cells. Open cell is constructed of interconnected pores, like a sponge, which allows fluid to pass through the material (Figure 2.3-8 (a)), whereas, closed cell foam have isolated pores (Figure 2.3-8 (b)). Open cell foams are generally used for heat transfer applications while closed cell foams have the advantage of higher compressive strength, but require more material [78].

Figure 2.3-8: Microstructure of foam (a) open cell foam, (b) closed cell foam. (adapted from [76]).

The open cell foam is categorised by pore density, denoted Pores Per Inch (PPI), which refers to the number of pores along a one-inch length. Figure 2.3-9 shows three pore density foams, 5, 10, and 25PPI, it is visible in the figure that as the pore density increases the connecting struts reduce in size.

A large portion of the research is devoted to the inclusion of open-cell foam structures into PCM material to enhance thermal conductivity, to unlock the storage potential of the PCM.

Figure 2.3-9: Foam desnity comparission, (a) 5PPI, (b) 10PPI, and (c) 25PPI [81].

X. Xiao et al. methodically detail the preparation of paraffin/metal foam composite phase change materials. Detailed in the study is the method used to impregnate the metal foam structures with PCM material. As the foam structure is porous, it is important to remove as much air as possible, in exchange for the PCM material. Show in Figure 2.3-10 is the process used for the impregnation of the foam with PCM to create a PCM/foam composite. The foam skeleton is placed in a vacuum chamber with solid PCM, the chamber is heated above the melting temperature of the PCM material, and once melted the Foam skeleton is submerged in the PCM. The use of the vacuum pump removes the air from the chamber, thus infiltrating the pores of the foam with PCM, exchanging as much air as possible for PCM material. The PCM is then left to cool down and solidify, the foam is removed after slight heating of the chamber to soften the PCM [83].

The authors of this study discuss the impregnation ratio of the foam, which is a dimensionless parameter relating to the percentage of impregnation, used to determine the compatibility of foam and PCM, the closer to one result in a higher impregnation of PCM into the foam skeleton. It is found in this study that it is not possible to reach 100% impregnation due to the cooling of the outside layer of PCM before the internal layers. Due to the density difference of paraffin-based PCM i.e., the density is greater when solidified, the inner PCM shrinks when

Figure 2.3-10: Process for impregnation of PCM foam composites [81]

cooling creating small air bubbles in the PCM. It is found that when under vacuum the impregnation of PCM increases to 96 - 98%, compared to 88.6 – 90.6% for non-vacuumed samples [83].

Many studies have been conducted using various foam skeletons/structures, most commonly the material of choice is aluminium, nickel or copper, and in some cases graphite.

Z. Wang et al. experimentally investigate paraffin/aluminium foam composite PCMs. The experimental results indicate that paraffin/aluminium foam composite has a cooling effect limiting the temperature rise of the LIB during discharge. The heat storage properties of pure paraffin and the composite PCM are also experimentally studied and is concluded that the addition of aluminium foam can largely improve the effective thermal conductivity of the PCM, although its existence suppresses the local natural convection. The experimental results indicate that the use of aluminium foam can speed up the melting process and improve the temperature uniformity of the PCM [84].

A notable study by W. Q. Li et al. experimentally investigates a sandwich structure of the copper foam and PCM for the passive cooling of a LIB pack. The nine 10 A LIB cells are sandwiched with 10 foam-paraffin plates which are constructed with 20PPI copper foam and RT44HC paraffin phase change material. The paraffin in this study is manufactured by Rubitherm GmbH, has a melting point of 42 °C and is a high-capacity variant. Foam impregnated with

(b)

Figure 2.3-11: Battery pack design (a) with copper foam, and (b) with PCM only [83].

paraffin is directly compared to a similar setup with only paraffin, shown in Figure 2.3-11. The authors report that when the battery pack is discharged at 0.5 C, there is no visible melting of the PCM, at 1 C and 3 C there was visible melting of the PCM. At the higher discharge rates, it is said that the battery remained under the safe temperature of 65 °C. This is true for both the PCM-foam and PCM-only configurations, however, it is noted that the battery temperature was lower for the PCM-foam configuration [85].

In [86] a novel passive thermal management system based on copper foam and paraffin composite PCM was designed for a lithium-ion battery pack, where the phase change storage energy unit was indirectly in contact with the cell. Different from the common configuration of filling the PCMs in the gap between the cells, two different Phase Change Storage Energy Units (PCSEUs), PCSEU-1 and PCSEU-2, were arranged in parallel on an L-shaped collector plate outside the battery pack. As shown in Figure 2.3-12, this arrangement avoided the PCMs directly contacting the battery cell but also utilises more PCM for heat absorption without occupying the battery pack space.

The core of the PCSEU is made of copper foam and n-eicosane paraffin, packaged by a 1 mm thick copper plate. The copper foam with a porosity of 95% and the paraffin with a purity of 99% were utilised.

Found by the authors, the highest temperature of the battery pack at 3C and 4C rates of charge/discharge could be maintained within the safety temperature under 28 °C, 35 °C and 42 °C respectively. The composite PCM is said to perform better temperature control capability at high ambient temperatures,

Figure 2.3-12: Phase change storage energy units setup. (adapted from [84]).

additionally, the indirect contact between the PCM and the battery cell avoided heating the battery as the PCM entirely melted.

As well to copper foam structures, research has adopted other forms of copper structures, for example in [87] the authors develop a copper mesh enhanced paraffin/expanded graphite as a composite PCM for battery thermal management where the copper mesh acts as a skeleton structure to enhance the thermal conductivity and strength of the cooling module. It is found that the copper mesh enhanced PCM shows much better heat dissipation performance and temperature uniformity compared to the absence of copper mesh, especially in harsh working conditions.

It is clear from the literature that the inclusion of foam structures plays an important role in the enhancement of PCM materials, particularly within the field of battery thermal management.

2.4 Conclusion

It is clear from the literature that there is scope for improvement in the collection of temperature data from the LIB, particularly when attempting to obtain reliable data from a LIB pack. This is prevalent when considering individual cell level monitoring of LIB packs, as there is limited literature on the use of multiplexed FBGs for this application. Additionally, there is scope for the investigation of the mounting method of the FOS sensor as typically the whole FBG is enclosed in microtubing to decouple strain and temperature.

When considering the use of foam and PCM/foam composited deployed for the removal of temperature build up at the LIB cell surface, the literature shows the use of solid metal foam such as copper and aluminium. There is scope within this research to investigate the use of alternative foam materials or manufacturing techniques to replicate copper foam. This is advantageous as the literature shows that the addition of copper foam into PCM is effective for the enhancement of PCM material to store heat generated by the LIB cells during discharge.

Chapter 3: Fibre Bragg Gratings for Li-ion Battery Thermal Monitoring

3.1 Introduction

Accurate temperature measurements can diagnose or prevent LIB failure; unfortunately, to date, there has been a multitude of accidents concerning LIB failure. In 2013 a Boeing 787 Dreamliner developed an abnormal temperature change and pressure build-up in a battery cell within its battery pack resulting in smoke and flames in the aircraft [20]. The Mars global surveyor was the victim of LIB failure in 2006; the exposure of the battery pack to high-temperature sunlight resulted in premature capacity degradation [20]. Studies have shown that when operating a LIB at lower temperatures, energy consumption is significantly reduced [16], [88], [89]. LIBs require a specific temperature window to work at peak efficiency, which is typically between 20 °C and 40 °C [59, 89, 90]. Temperatures below this range cause a slow reaction rate within the cell, resulting in less current delivery and, thus, reduced performance as well as accelerated ageing effects within the cell, impacting usable life [89]; therefore, temperature measurement is an appropriate tool for predicting temperature-induced degradation mechanisms [26], [57].

As discussed, thermocouples are the most widely used technique for temperature monitoring as they are typically low-cost and have small dimensions [91]; however, in comparison to thermocouples, fibre optic sensors (FOS) have several advantages, such as electrical passivity and the ability to withstand harsh environments at elevated temperatures [92]. FOSs are typically lightweight, with a smaller physical dimension compared to thermocouples and enable a wider bandwidth of data, which is useful to sensor systems involving the interrogation of a collection of sensing elements or a sensor grid [18]. Applications, i.e. where many measuring points are needed to achieve comprehensive monitoring, can take advantage of the multiplexing capabilities of FOS systems as they can offer multiple monitoring points on a single fibre resulting in minimal wiring requirements with high measuring points densities [93]. In a typical large-scale LIB pack of hundreds or thousands of individual cells, the battery management system (BMS) monitors the temperature of sub-grouped cells, often referred to as modules. LIB failure can occur due to the lack

of individual cell monitoring, which is avoidable if a broader range of information about individual cell temperature is available to the BTMS [20].

The FOS scheme with multiple fibre Bragg gratings (FBGs) is a promising alternative for obtaining battery temperature due to its ability to customise the location of the sensors. Applying multiple photo-inscribed Bragg gratings on one fibre means that individual cell monitoring is an ever-increasing possibility as one optical fibre strand containing multiple sensors could be used to monitor a multitude of cells simultaneously. Pouch cells, a common LIB type, are the subject of investigations using FOSs with FBGs [18], [19], [94], [95]. To date, research on utilising FOSs on cylindrical type LIBs is limited.

Notably, M. Nascimento et al. [96] utilise a Sanyo LITUR18650SAN cell to investigate the real-time monitoring of external temperature and strain variations using FBG sensors under charge and different discharge C-rates. During the discharge process, the study finds strain variations said to be induced by pressure increases within the LIB [96]. J. Fleming et al. and E. McTurk et al. take advantage of FOSs to reliably obtain core temperature data from a cylindrical LIB cell [57], [56]. Using a single-mode SMF-28, 9/125 mm fibre with four 5 mm FBGs evenly spaced, J. Fleming et al. were able to record "unprecedented cell data" from the LIB core [57]. E. McTurk et al. using a silica fibre with a single FBG for LIB Core temperature measurement highlight the linear relationship between the FBG Bragg wavelength, temperature or mechanical strain; in this study, the strain relief is obtained with an aluminium tube [56]. The Bragg reflected wavelength is sensitive to applied strain or temperature changes; this poses a requirement for a method to determine or alleviate strain or temperature, in the form of mechanical relief or by subtracting the difference in wavelength shift measured by a nearby FBG sensor which is isolated from the disturbance in question [56], [97].

The work presented in this chapter investigates an FBG sensor array placed on a Panasonic NCR18650B cylindrical LIB, with a particular focus on the sensor mounting technique. The Panasonic cell model is used as it is widely available commercially, and its form factor and electrical specifications are similar to the LIB Panasonic supplies to Tesla for the Model S EV [98]. The process carried out in this investigation is similar to other studies on the pouch and coin cell types [18], [19] in which a FOS with five FBG sensors are glued to the battery

and placed into a thermal chamber. These studies use varying sensor-mounting methods and sensor arrangements. For example, in [19], a pouch cell is monitored with 3 FBGs and three thermocouples with three glue spots evenly distributed along the length; and in [18], coin cells with FBG sensors placed at the positive and negative terminals, with thermocouples placed for comparability.

The work herein differs from the examples discussed above in terms of isolating the temperature reading from the strain induced on the fibre using a 'guide tube' mounting method. The FBG can measure temperature and strain simultaneously; thus, the two measurements must be decoupled. The adhesion of the sensors onto the battery surface is an essential aspect as the battery expansion and contraction, i.e. resulting from variations in the internal pressure, could influence the temperature measurement in that the strain-induced variation would read as a temperature fluctuation [96], [97]. The two mounting methods explored in this chapter clarify the potential errors in temperature measurement, i.e. induced by strain.

3.2 Materials and Methods

This section details the methodologies for the implementation of the mounting methods considered for evaluation and the subsequent materials used to achieve the experimental results.

3.2.1 Fabrication of the Fibre Bragg Gratings Sensors

The FBGs used for this work were manufactured by of the University of Mons, Belgium, using the following method: FBGs are photo-inscribed using a Noria FBG Manufacturing System from NorthLab Photonics. This setup integrates a set of different phase masks, an Argon Fluoride (ArF) Ultraviolet (UV) excimer laser (Coherent Excistar XS) emitting at 193 nm and all the optics required for FBG fabrication. The system provides a 1-D translational stage as well, allowing accurate control of the position of the optical fibre before the photo-inscription process. A hydrogen-loaded single-mode optical fibre (SMF-28) was placed on it to photo-inscribe 5 FBGs along with the same fibre. After the photo inscription of each FBG, the fibre was shifted along its longitudinal axis and placed under the next phase mask, repeating this sequence until the full FBG array was completed. The length of the FBGs was 5 mm each, and the pitch of the phase

masks was 1054 nm, 1063 nm, 1070 nm, 1075 nm and 1082 nm, respectively. The laser emission configuration was set to a pulse energy of 5 mJ and a repetition rate of 50 Hz, and each FBG was photo-inscribed by a single burst of 100 shots. The Refractive Index Modulation (RIM) induced on the fibres by using this manufacturing system occupies a broader region of the core [99], being the RIM more homogeneously distributed concerning FBGs fabricated using other methods. Finally, the FBGs were kept at 100 °C for 36 hours to remove the residual hydrogen content of the fibres and stabilise their thermal response while in operation.

3.2.2 Thermocouple sensors

This study uses two K-type thermocouples; these are typical sensors used for battery surface temperature measurement [19], [100], [101]. A Reveltronics EGT-K 4-channel thermocouple amplifier produces a linear voltage relating to the temperature experienced by the thermocouple sensors. Based on the AD8495 precision thermocouple amplifier with cold-junction compensation, the EGT-K amplifier converts thermocouple non-linear millivolts signal to 0-5 V linear analogue output. Where 0 V is 0 °C, and 5 V is equal to 1250 °C, the accuracy of this amplifier is ± 1.5 % with a conversion rate voltage of 4 mV/°C. The AD8495 thermocouple amplifier is explicitly designed for measurement using K-type thermocouples [91].

The temperature response of the thermocouples is calculated using Equation 7, where T is the temperature in degrees Celsius, V_{out} Is the amplifier output voltage, and V_{CR} is the conversion rate voltage of the amplifier.

$$T = V_{out}/(V_{CR} \times 1000)$$

(7)

3.2.3 Fibre Bragg Sensor Arrangement

Two sensor arrangements to evaluate the best practice for sensor adhesion on the battery are devised. In the first case, the optical fibre containing the sensors is glued at either end of the battery (configuration A), whereas in the second case, only one end is glued to the battery, while the other end is attached to the battery via a small tube for ease of expansion, "guide tube" (configuration B). Configuration A is depicted in Figure 3.2-2, configured with the FOS placed along the length of the cylindrical Panasonic NCR18650B LIB surface and a small amount of Micro-Measurements M-Bond 200 adhesive used at either end

to attach the fibre to the surface. Configuration B, depicted in Figure 3.2-2, is configured with the fibre placed along the length of the cylindrical surface and glued with the same adhesive at the negative terminal, attaching the fibre to the surface. At the same time, the other end of the battery utilises a guide tube, a small PVC tube serving the purpose of keeping the fibre in the longitudinal direction. The use of the tube allows for the natural expansion and contraction of the battery cell to occur without affecting the FOSs, thus allowing the FBG sensors to capture only temperature variations from the cell surface. This contrasts with sensor configuration A where the FOSs would experience strain due to the restrictive nature of 2 glue spots.

(a)

(b)
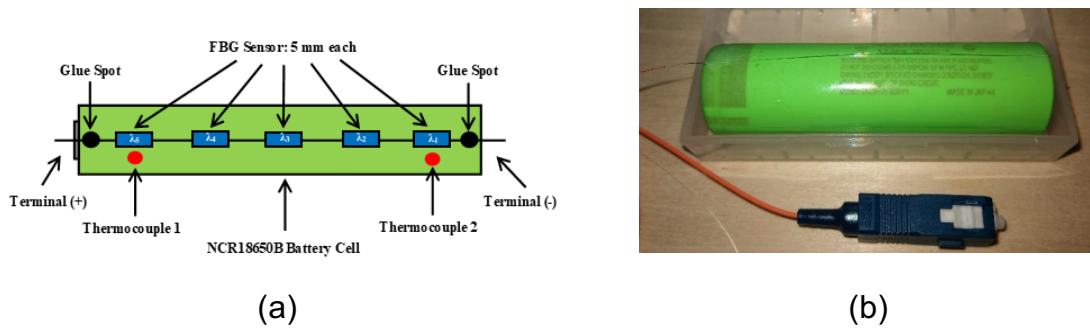
Figure 3.2-2: Sensor Configuration A: Illustration (a) and image of assembly (b) of the optical fibre with five FBG sensors placed along the length of the NCR18650B LIB.

(a)

(b)
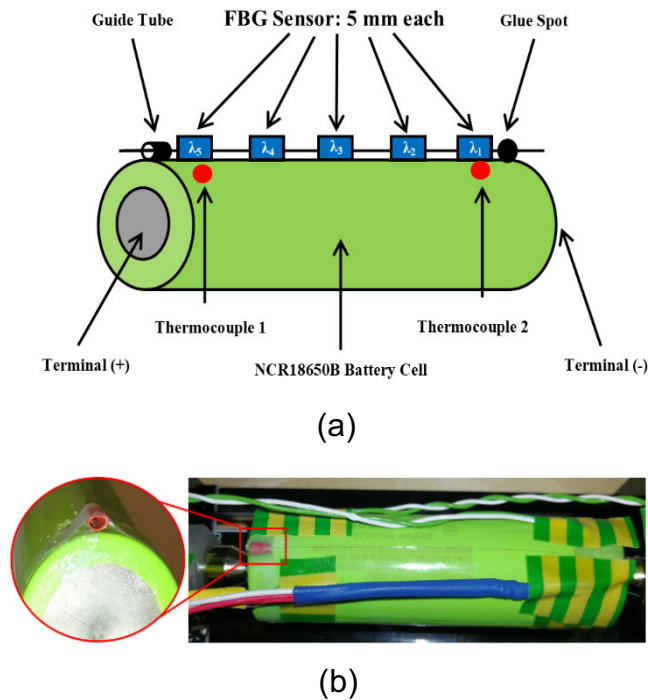
Figure 3.2-2 : Sensor Configuration B: Illustration (a) and image of assembly (b) of the optical fibre with five FBG sensors placed along the length of the NCR18650B LIB, guide-tube represented with a close-up in (b).

The Micro-Measurements M-Bond 200 adhesive used for the work presented herewith is a Cyanoacrylate type adhesive which can be used at a temperature range of -31.67°C to +65.55°C. In both configurations, the 5 FBGs were not directly attached to the battery surface; a slight slack remains in length, which allowed for some compensation from the natural expansion and contraction of the LIB due to internal pressure variation [97]. A K-type thermocouple at either end of the LIB surface is applied, directly opposite FBGs 1 and 5. Two thermocouples are used, i.e. instead of five, to avoid overcrowding on the battery surface, which might result in restricting or damaging the FOS. These adhere to the surface with vinyl tape, which offers flexibility in the mounting position; the use of tape to adhere thermocouples to the LIB surface is present in multiple studies [61, 101-103].

3.2.4 Sensor Calibration

Configuration A, with the FOS attached at both ends of the LIB, was calibrated over a temperature range of 10°C to 40°C ± 1 °C at increments of 10°C, for at least 30 minutes. The FBG response over the 40°C calibration schedule is shown in Figure 3.2-3, which demonstrates agreement between the wavelength shift of the FBGs and the data from the thermocouples. The calibration and mean sensitivity of each FBG sensor over the chosen temperature range are

Table 1: Configuration A Calibration mean wavelength shift

Temperature (°C)	FBG 1 (nm)	FBG 2 (nm)	FBG 3 (nm)	FBG 4 (nm)	FBG 5 (nm)
10	1524.22	1537.18	1547.08	1554.30	1564.22
20	1524.31	1537.27	1547.17	1554.39	1564.31
30	1524.50	1537.37	1547.27	1554.48	1564.41
40	1524.50	1537.47	1547.37	1554.59	1564.51

Mean wavelength of each FBG at each calibration temperature variation, 30 min averaged data, nm = nanometre.

Table 2: Configuraton A wavelength shift standard deviation

Temperature (°C)	FBG 1 (pm)	FBG 2 (pm)	FBG 3 (pm)	FBG 4 (pm)	FBG 5 (pm)
10	2.5	4.3	5.7	5.5	4.2
20	2.8	3.9	5.4	5.3	3.7
30	3.4	4.2	5.6	5.5	4.5
40	4.3	4.8	6.2	6.4	5.3

Wavelength shift standard deviation for each sensor in response to calibration temperature variation, pm = picometers
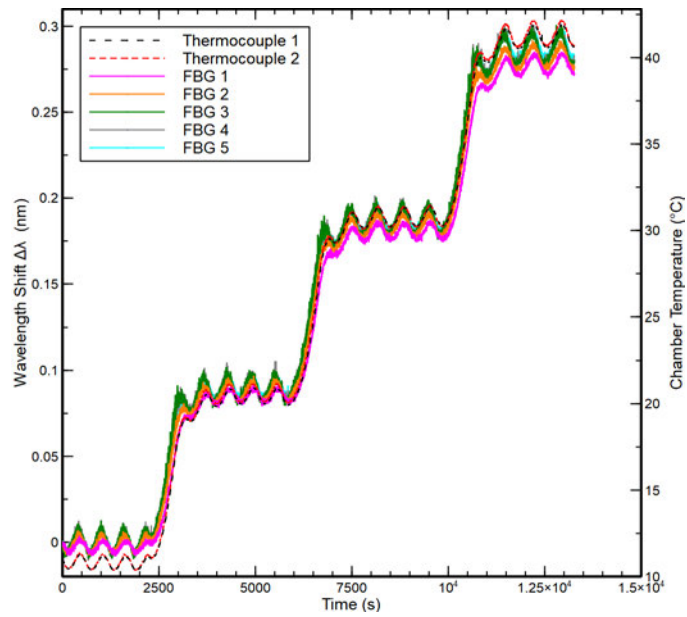
(a)
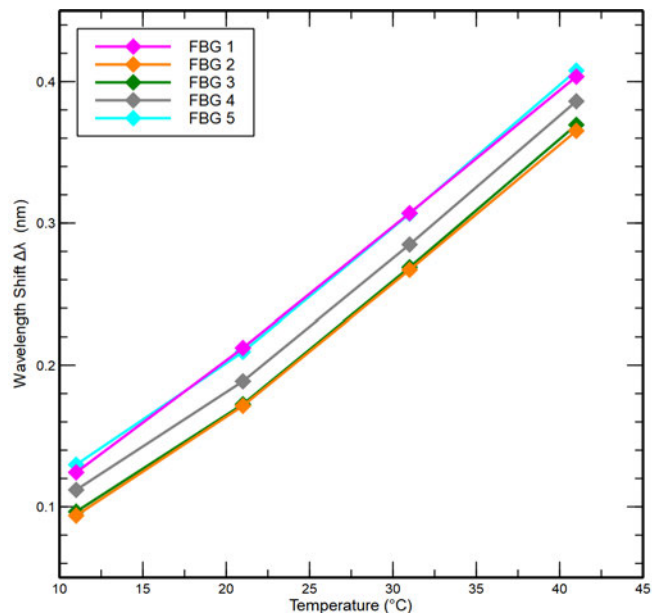
(b)

Figure 3.2-3: FBG calibration sequence under configuration A: The wavelength shift over the calibration temperature variation (a), and (b); the resulting sensitivity over the 40 °C variation using 30 min averaged data.

shown in Figure 3.2-3 (a) and (b), respectively. The chamber maintained a fluctuation of ±1°C throughout the testing, which is visible for each temperature step in Figure 3.2-3 (a). The fluctuation within the chamber is due to the maximum settings achievable with the current thermal chamber equipment. Taking the mean wavelength shift (Δλ) for each of the 5 FBG sensors over 30 minutes provides a single wavelength shift data point; **Table 1** shows the mean wavelength for each FBG over this period.

Calculated for the four temperature exposure points, Table 2 shows the standard deviation for all FBG measurements at the exposure temperatures. Thus, the method used herein accounts for the fluctuation of temperature within the chamber; this method of calibration is similar to those presented in other studies with FBG sensors [18], [19]. Using this method, the sensitivity of FBG sensors 1, 2, 3, 4 and 5 are 9.16, 8.90, 8.95, 8.99 and 9.12 pm/°C, respectively. For configuration B, the sensitivity factor is for a 'free' fibre, defined by the manufacturer, where the optical fibre did not adhere to any surface, the sensitivities of FBGs 1, 2, 3, 4 and 5 are stated as 9.80, 9.87, 9.93, 9.93 and 9.97pm/°C, respectively.

3.2.5 Data Acquisition

The schematic of the data acquisition is detailed in Figure 3.2-4, where the wavelength shifts corresponding to the 5 FBGs are acquired using a Micron Optics sm125 FBG interrogator with the ENLIGHT software. A PicoLog 1012 data logger is used to record the output voltage of the Reveltronics thermocouple amplifier with the PicoLog 6 software. A B&K Precision 8601 DC programmable electronic load is used to discharge the LIB; a B&K Precision 9202 multi-range programmable DC power supply is used for charging. Data logging in the ENLIGHT, PicoLog 6 is set to 2Hz while the B&K Precision software is set at 1Hz.
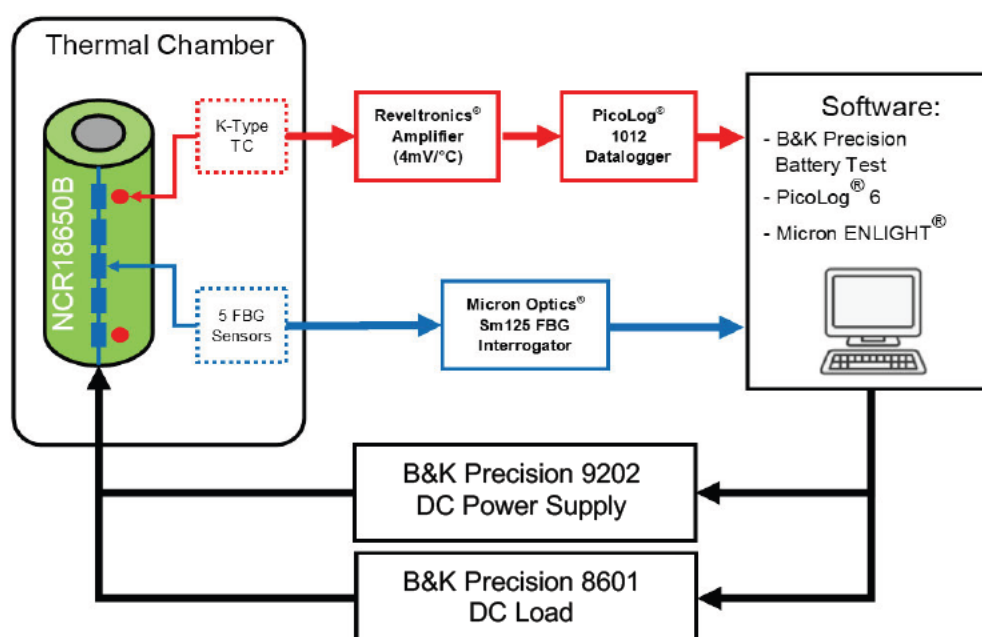
Figure 3.2-4: Detailed diagram of the data acquisition setup for single cell testing with FBG sensors.

The thermal behaviour of the FBG sensors is defined by Equation 8 [19], [104], where k is the temperature sensitivity, λ_0 Is the reference wavelength, and λ is the measured peak wavelength as a function of temperature.

$$\lambda = (k \times T) + \lambda_0 \qquad (8)$$

Rearranging (8) provides the temperature:

$$T = \frac{(\lambda - \lambda_0)}{k} \qquad (9)$$

The reference wavelength for both configurations A and B is defined from manufacture as 1524.1nm, 1537.1nm, 1524nm, 1554.2nm and 1564.1nm for FBG 1, 2, 3, 4 and 5, respectively. Thus, using (9), the thermal response of the LIB under the discharge conditions is derivable from the FBG signals.

3.2.6 Lithium-ion Battery Discharge Technique

Constant power (CW) discharge is used to assess the sensors attached to the LIB cell, shown in Figure 3.2-5, as the voltage decreases over the discharge period, the current increases to maintain the constant power output.

Ten-Watt CW discharge induces a thermal reaction from the Panasonic NCR18650B LIB. This rate of discharge increases the LIB surface temperature by approximately 14°C. An almost identical reaction from the LIB cell for both sensor configurations is shown in Figure 3.2-6 (a) and Figure 3.2-6 (b). During

Figure 3.2-5: Constant Power (CW) Discharge at 8 Watts [105].

the discharge, as the voltage reduces at a varying rate, the current must increase to provide a CW output; thus, the current reacts with a significant upward inflexion to counteract the downward Voltage inflexion. A significant temperature change occurs in the LIB with the increased current; typically, the temperature increase follows the current increase [72, 105], which makes the proposed setup an ideal technique for temperature measurement. Both sensor configurations are subject to the same treatment, i.e. the LIB is charged at 1 C (3.4 A) Constant Current (CC) Constant Voltage (CV) at 4.2 Volts. During charging, the LIB is charged at 1 C until the voltage reaches maximum cell voltage, i.e. 4.2 V, upon which the charger switches to CV and the current gradually reduces until the cut-off current, i.e. 65 mA, is achieved. Before discharging, the cell is in a state of rest for 4 hours to allow for internal balancing, similar to the process in [106]. Two thermal chambers keep the LIB cells at the optimal temperature; one chamber is for storage purposes where cell resting occurs, and the other is for testing. Both chambers are at an optimal 25°C ± one °C, which limits the temperature variance of the LIB cells between the testing and resting phases.

(a)   (b)
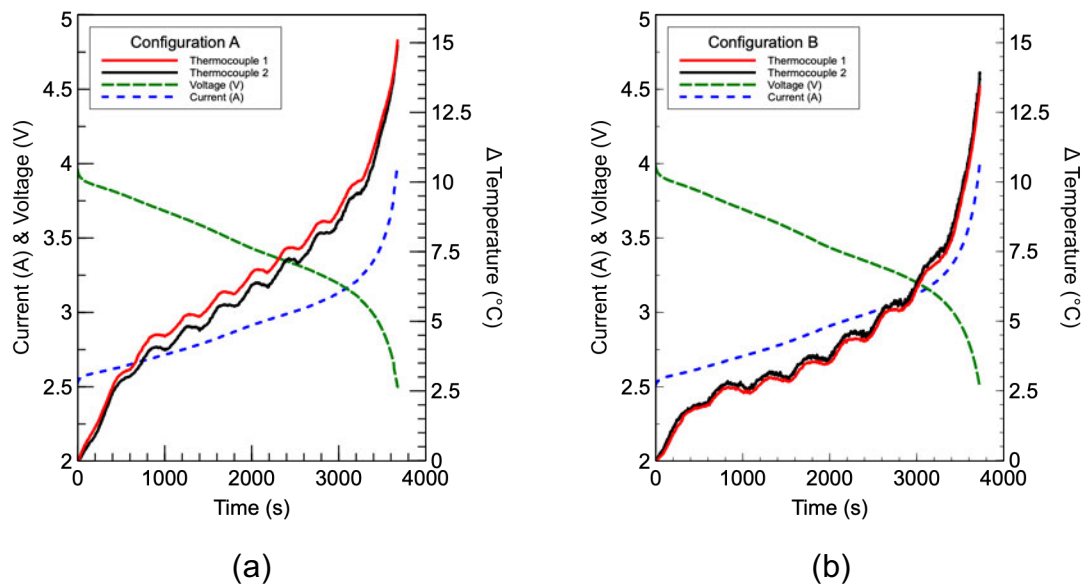
Figure 3.2-6: 10-Watts CW discharge: Voltage and current inflections and comparable thermal variance by thermocouples for sensor configuration A (a); and Sensor configuration B (b).

3.3 Results

To determine the effectiveness of the mounting method's ability to isolate the temperature for reliable readings, the FBG response is compared directly to the thermocouple; however, it is crucial to discuss the temperature variation over

the length of the LIB surface and the accuracy of the thermocouple system before comparing the FBG response with the thermocouples. The mean temperature difference between thermocouples 1 and 2, neglecting the error, is 0.2 °C for sensor configuration A and 0.32 °C for configuration B, both having a standard deviation of 0.09 °C. This shows that the thermocouples i.e. placed at the opposite ends of the LIB surface, respond in a very similar way. Moreover, as the thermo- couples experience only a small temperature variation over the length of the surface during the stated discharge process, it is reasonable to assume the resulting FBG temperature readings do not become distorted by a varying temperature differential over the cell surface for both sensor configurations.

As discussed previously, the accuracy of the thermocouple amplifiers is ± 1.5%.
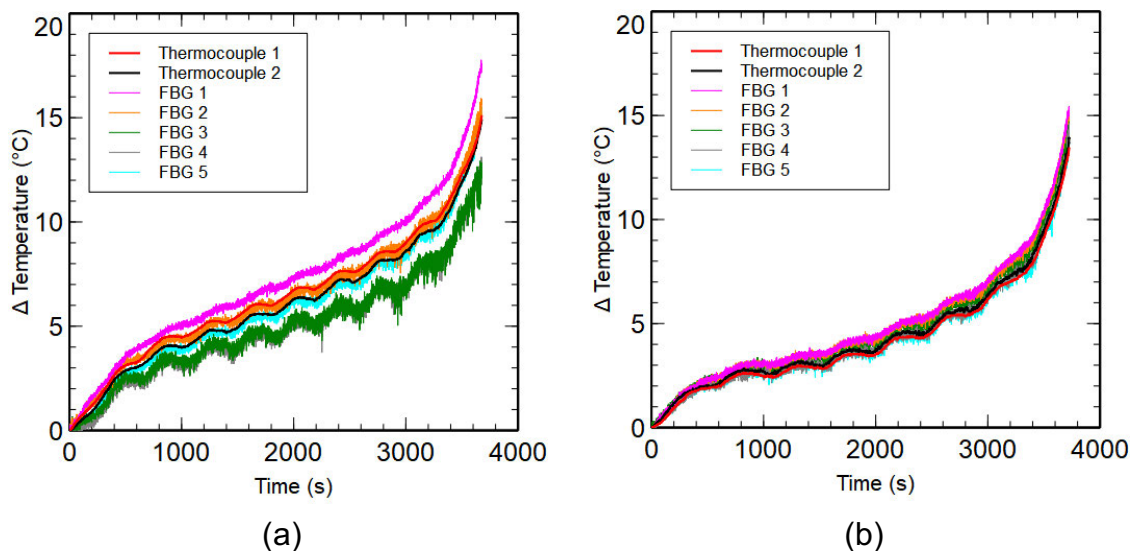
Figure 3.3 1: Temperature response of FBGs during CW discharge for Sensor configuration A (a) and configuration B (b), compared to the measurements obtained by the thermocouples.

Considering this for both the sensor configurations during the LIB discharge; for Sensor configuration A, thermocouple 1 and 2 demonstrates a minimum and maximum error of 0.36 °C and 0.58 °C respectively, with a standard deviation of 0.04 °C. In terms of Sensor configuration B, thermocouple 1 ranges from a minimum error of 0.37 °C to a maximum error of 0.58 °C, with a standard deviation of 0.04°C. Comparatively, thermocouple 2 experiences a minimum and maximum error of 0.38 °C and 0.59 °C respectively, with a standard deviation of 0.04 °C. Figure 3.3 2 shows the response of the thermocouples and

the corresponding temperature error throughout the LIB discharge for both sensor configurations. As can be seen from Figure 3.3 2 (a) and (B), both thermocouples, incorporating allowable error from the thermocouple amplifier, behave in an almost identical manner. This further suggests a uniform temperature variation over the LIB sur- face during discharge. Comparing both sensor configurations, it is evident that mounting techniques play a vital role in the resulting temperature sensing. The resulting variation in temperature (ΔT)
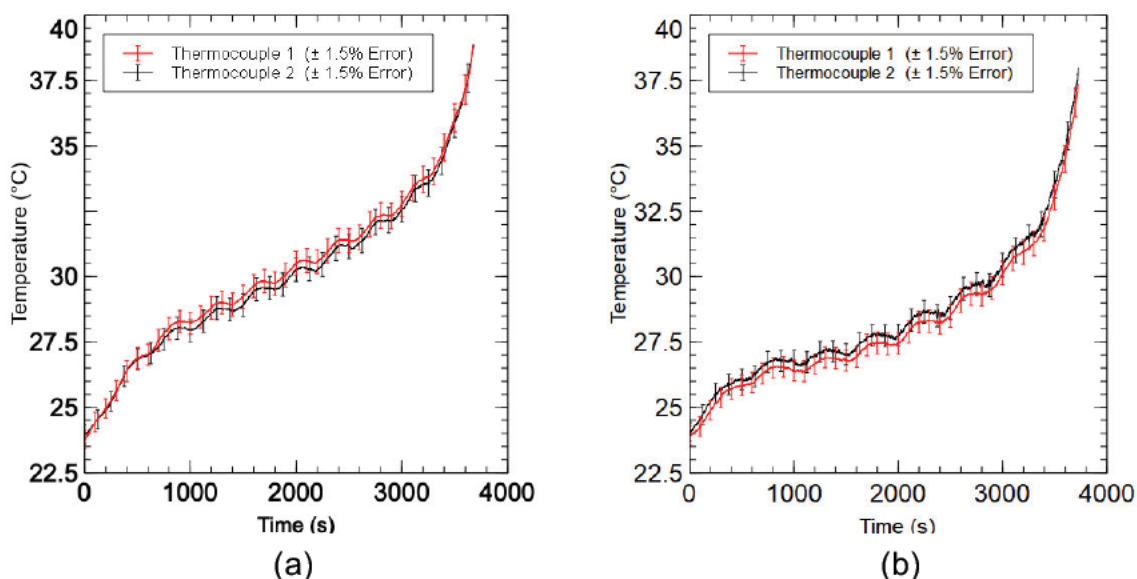
Figure 3.3 2: Temperature response of thermocouples during CW Discharge (a) configuration A (b), configuration B, demonstrating amplifier error of ± 1.5%.

for both sensor arrangements is shown in Figure 3.3 1, and as can be seen, for sensor configuration A, the temperature measurement of each of the FBG signals is not consistent, and indeed, in the most extreme case, a difference of 8.5 °C between FBG3, FBG4 and FBG1, could be observed. On the other hand, sensor configuration B (Figure 3.3 1 (b)) demonstrates a more consistent and uniform measurement of temperature along the LIB surface with a maximum temperature difference of 2.13 °C. In correlation to thermocouples, thus, the use

of the guide tube shows a significant improvement in the ability of the FBG sensors to measure the temperature of the LIB. The variation in temperature
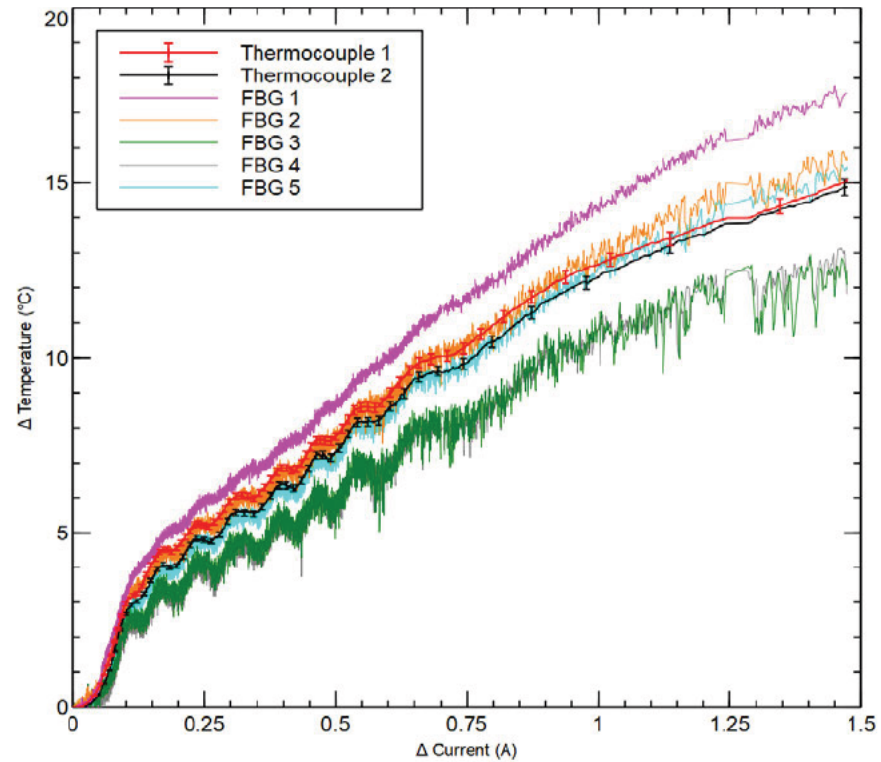
(a)
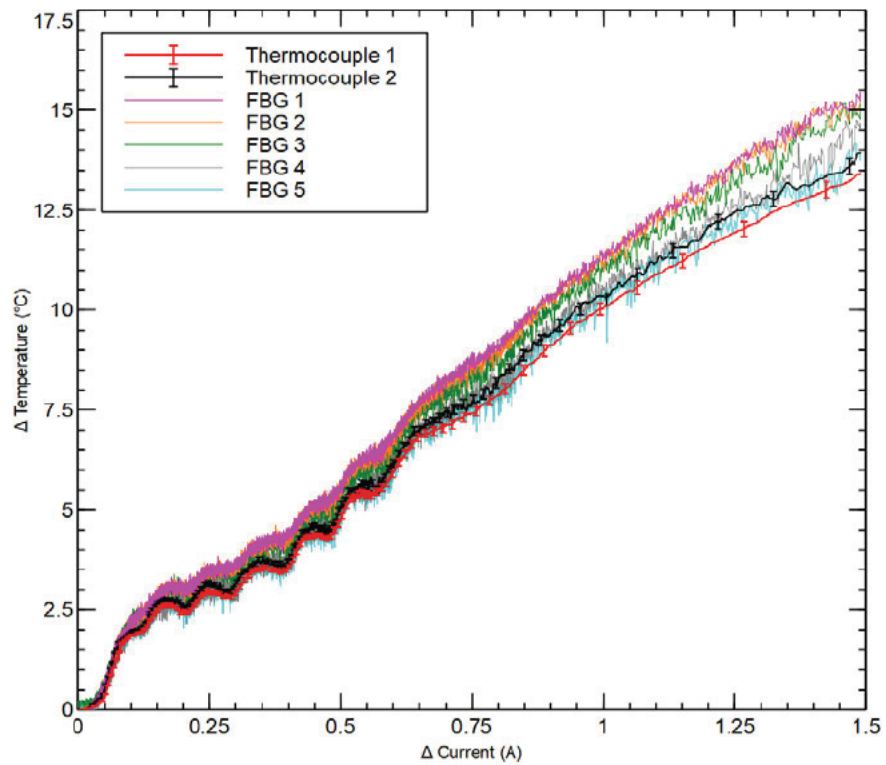
(b)

Figure 3.3 3: FBG temperature variation related to discharge current change for constant power discharge: Sensor configuration A (a), and Sensor configuration B (b), compared to the measurements obtained by the thermocouples.

(ΔT) of the FBG sensors and thermocouples against the discharge current (ΔI) over the discharge period, is illustrated in Figure 3.3 3.

The purpose of the discharge tests is to evaluate the performance of the FOSs, i.e., under the two configurations, concerning discharge current. The change in current (ΔI) of each discharge experiment is consistent, and therefore, it is reasonable to assume similar temperature differentials within the LIB. The analysis demonstrates the increase in temperature differential with increasing load current on the LIB. It is clear from the obtained measurements that enabling free movement with the addition of the 'guide-tube' results in significantly more accurate measurements. The results in both Figure 3.3 1 and Figure 3.3 3 demonstrate that sensor configuration B, i.e., with the guide tube, is more suitable to measure the temperature of the cylindrical LIB surface. When compared to the thermocouples, sensor configuration A generally displays accuracy of ± 4.25 °C (8.5 °C variances), which is reduced to + 2.13 °C (2.13 °C variance) in configuration B with the strain-relief of the guide-tube in place.

These results demonstrate that the behaviour of each FBG is not consistent between the two sensor configurations; both Figure 3.3 1 and Figure 3.3 3 illustrate that configuration A has the highest variation in temperature for FBG1, however, under sensor configuration B, this is not the case, as FBG1 and FBG2 indicate an almost identical response. In both configurations, FBG5 exhibit a similar response, whereas FBGs 3 and 4 exhibit the most considerable difference in measurement, compared to the responses from the thermocouples.

It is reasonable to conclude that sensor configuration A, i.e., with two glue spots on either end of the sensing region, induces sufficient strain on the FBGs and hence influences the temperature measurements significantly; to the point, inaccuracies render the data ineffective analytically. Sensor configuration B, i.e., mounting technique with guide-tube, demonstrates promising results, where the response from the FBGs is closely related to that of thermo- couple sensors, this is due to the guide-tube allowing the optical fibre containing the FBGs to act independently of strain induced by internal pressure fluctuations within the LIB.

It is essential to highlight that although sensor configuration B provides a more accurate representation of the LIB, the recorded temperatures do not come

within the error margin of the thermocouples, except for FBG5, which demonstrates a response across both thermocouples, including allowable error. However, this work aimed to evaluate the suitability of the guide-tube technique to attach the FOSs to the battery surface.

The findings show that the FBG sensors' readings using the guide tube mounting method are comparable with thermocouples that were mounted directly to the LIB. The results demonstrate that submergence of the sensing region with a binding agent is not necessary. This enables multiple benefits including the reduction of the number of chemicals needed, the risk of chemical reaction with the battery and increased ease of handling, i.e., each thermocouple requires separate wiring while all the 5 FOSs were along a single fibre strand of less than 1 cm diameter. However, fine-tuning of the FBG sensors are required to make measurements that are within the acceptable error margin. For example, the physical parameters of the FBG can be optimised, i.e., the length of the FBG could be longer.

3.4 Conclusion

The motivation for this research was to conduct a proof of concept on the guide-tube technique for the measurement of the temperature of LIBs without having to attach the entire length of the fibre with a binding agent. A multitude of literature provides work on such FBG sensors which are submerged in a binding agent, i.e., to attach the sensors to the LIB but are then susceptible to strain. The target for the proof of concept, therefore, was to evaluate the possibility of attaching the FBGs to the LIB in a manner that enables (a) the measurement of temperature without the use of a binding agent on the sensing region, and thus (b) having no susceptibility to strain. The results demonstrate that this is possible with the guide-tube technique that is proposed.

Furthermore, the work presented herein demonstrates the importance of the application of appropriate mounting techniques for optical fibre when used for the measurement of LIB temperature. The strain induced on FBGs is sufficient to render the temperature measurements inaccurate, without careful placement of the fibre. The proposed guide-tube method provides a suitable solution for mounting an optical fibre strand, with multiple FBGs incorporated along its

length, on a LIB, to reduce strain effects and thus more accurately record the temperature and hence improve the overall performance of LIB thermal monitoring. The accuracy of the temperature readings, when compared to thermocouples, is improved from ± 4.25 °C (8.5 °C variations) to + 2.13 °C (2.13 °C variation) when the guide-tube mounting method is adopted.

Chapter 4: FBGs for Individual Cell-Level Temperature Monitoring of a LIB Pack

4.1 Introduction

The importance of temperature measurement of the LIB has been extensively discussed in the previous chapter; this chapter deals with this important concept on a broader scale concerning the measurement of a LIB pack temperature. Individual cell-level temperature monitoring is an important concept for the advancement of the LIB pack, particularly the safety aspect. At present, the LIB temperature is measured at the module level, not the cell level, which is not the optimum scenario for the BTMS. The basic approach for commercial vehicles is to measure the temperature at several select points on the surface or tab of LIB cells [107, 108]. In large format LIBs, this temperature can widely differ from the temperature reached in the LIB core [109], which is the critical temperature in terms of performance and safety [108].

As previously discussed the BMS protects the LIB cells against abuse such as over-voltage, under-voltage, over-current while charging or discharging, over-temperature, under-temperature and cell balancing, however, if abuse conditions occur and a severe temperature gradient is induced, under extreme conditions, the separator will melt, causing an internal short circuit which can lead to uncontrollable temperature rise, thermal runaway, in the cell [29]. There are many LIB cells in a battery pack, for example, Tesla used more than 7000 18650 LIB cells for the Tesla Model S, and Mitsubishi used 88 large prismatic cells for their Mitsubishi i-MiEV vehicle [29]. With the multitude of LIB cells, it is crucial to obtain sensible temperature data, ideally at the individual cell level.

There are numerous works to obtain battery parameters, such as state of charge (SoC), voltage and capacity, however, the literature on individual cell level monitoring of temperature is limited.

It is demonstrated in [110] that a cell-level control approach uses a control algorithm to bias individual cells differently based on their state of charge, capacity and internal resistance to counteract the accelerated ageing effects on weak cells. This research resulted in a longer lifetime for the overall pack. Furthermore, the approach leads to a more homogeneous distribution of cell

capacities at the end of the first life, providing more value in the battery pack for second life use such as grid energy storage.

J. Meyer et al. demonstrate large multiplexing of FBG sensors for use on battery systems. The authors employ 96 FBG over 14 FOS strands to measure the strain and temperature of a 13.8 kWh battery pack. The calibration of the FBG sensors was carried out by placing the whole battery pack into a thermal chamber and subjected to 15 °C, 30 °C and 45 °C temperature levels. Select FBG sensors are mechanically decoupled with a small tube to alleviate the strain on the FBG for temperature measurement, some are directly attached to the cell surface to measure strain. The cells are subject to various abuse conditions such as fast charging, overcharging to force gassing, and cycling at sub-zero temperatures to force lithium plating on the anode. The battery was also subject to short-circuit events by penetrating a cell with a nail, inducing thermal runaway [15].

The authors conclude that they record temperatures up to 750 °K during the thermal runaway experiment. Additionally, it is stated that the fibre optic system can deliver important additional information on the LIB state. It is found that the ability to measure every cell temperature provided a much higher maximum cell temperature than the BMS showed, improving safety, particularly with the ability to measure the temperature between LIB cells [15].

It is clear from the literature that the use of FBGs for temperature measurement is an area of great interest where many researchers have successfully utilised the sensing method for the measurement of a single LIB cell, in some cases multiple measurements across one LIB cell.

The purpose of the works contained herein is to determine the accuracy of the FBG sensors at the individual cell level in comparison to the commercial TC and PT sensors. A FOS strand with five FBGs is laid across a three-cell parallel battery pack and discharged at three different conditions; 0.5 C, 2 C and 40 Watt constant power. This is used to validate the 'guide tube' method, discussed in the previous chapter, as a simplified mounting technique for the Individual cell-level monitoring of LIB temperature. It is important to note that great care has been taken to calibrate the sensors to fully legitimise the FBG temperature measurements.

4.2 Methodologies

The method for the mounting of the FOS strand with five FBGs is discussed, as well as the calibration of the sensor and the experimental setup.

4.2.1 Enhanced Guide Tube Mounting Method

The guide tube technique is revised to provide more contact with the cell surface and reduction in any longitudinal friction in the FOS; this is achieved by implementing a micro-Polytetrafluoroethylene (PTFE) tube as the guiding structure, thus allowing expansion and contraction of the FOS during heating and cooling, decoupling strain and temperature measurements.

As shown in Figure 4.2-1 the FOS strand is placed over the three-cell LIB pack using 3D printed ABS plinths. One plinth is used to glue the FOS at one side of the battery pack, attached to the fibre cladding so as not to interfere with the bare fibre section containing the FBGs. The other side has a plinth with the PTFE 'guide tube' attached, in which the end of the FOS is placed though, thus holding the FOS section with FBGs over the three LIB cells.

The FBG sensors arrangement is shown in Figure 4.2-2 where three FBGs, FBGs 1, 3 and 5 are situated over a battery cell, and FBGs 2 and 4 are situated in the middle of two cells. This provides data for each cell and the temperature variation at the cell intervals. On each cell, a K-type thermocouple, and a class B PT100 sensor is placed for additional measurements of temperature to validate the FBG response.

(a)   (b)
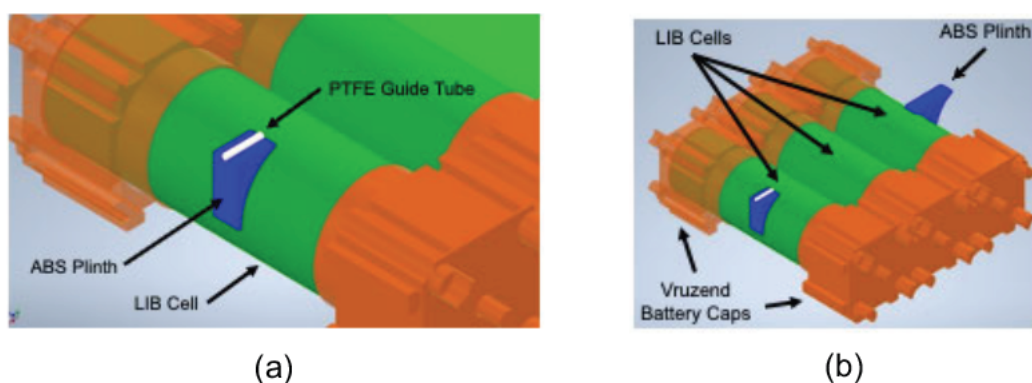
Figure 4.2-1: Guide Tube Mounting Method; (a) ABS Plinth and PTFE Guide Tube Assembly (b) view of the whole assembly.

(a)

(b)
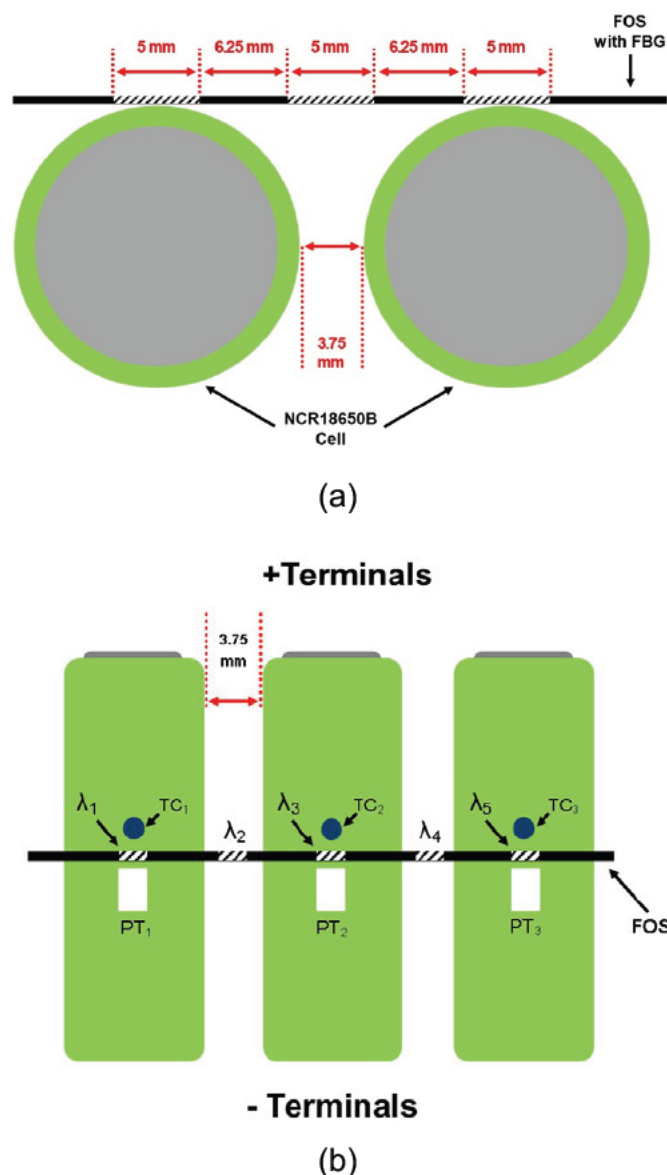
Figure 4.2-2: Diagram of the FOS and FBG Placement: (a) The FOS position in the middle of the four Li-Ion Cells, each cell separated by 3.75 mm, one 4-wire PT-100 sensor (PT) and K-type Thermocouple(TC) placed next to each FBG on a cell and (b); the positioning of FBGs, 5 mm per FBG with 6.25 mm spacing, Li-Ion Cells Spaced 3.75 mm apart.

4.2.2 Data Acquisition Setup

Similar to Chapter 3, shown in *Figure 4.2-3*, the wavelength shifts corresponding to the 5 FBGs over the three-cell LIB pack are acquired using a Micron Optics sm125 FBG interrogator with the ENLIGHT software. A PicoLog TC-08 data logger is used to record the temperature of the thermocouple sensors via the PicoLog 6 software. Platinum resistance sensor temperature response is also recorded in the PicoLog 6 software via a PicoLog PT-104 data logger. A B&K Precision 8610 DC programmable electronic load is used to discharge the LIB;

a B&K Precision©, 9202 multi-range programmable DC power supply is used for charging. Data logging in the ENLIGHT©, PicoLog 6 and the B&K Precision© software is set at 1Hz. PicoLog.

The setup for the experimentation in this chapter now includes the ESPEC LU114 low-temperature chamber, which is a professional chamber used to maintain a stable ambient temperature. The calibration certificate of the chamber is shown in Appendix B, showing ± 1°C accuracy. Additionally, the battery pack is held in a faraday cage to eliminate any outside interference.
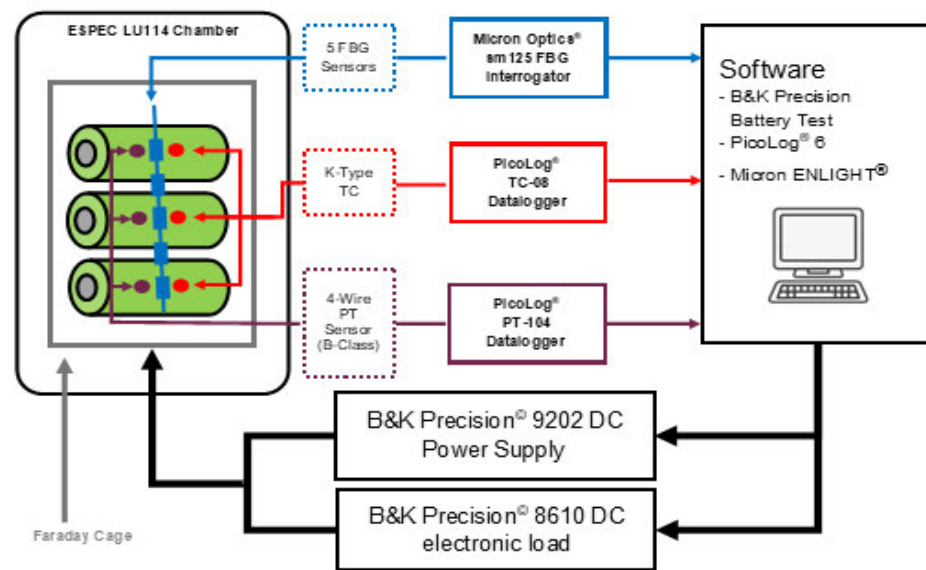
Figure 4.2-3: Experimental setup for battery pack discharging with FBG sensors.

4.2.3 Sensor Calibration

To ensure the FBG response can be compared to the TC and PT Sensors, it is important to establish the accuracy of the testing equipment being used. This will certify the comparison between the sensor types during the analysis of the experimental works carried out in this chapter.

This sub-section details the calibration of the PicoLog TC-08 to establish the correctness of the thermocouple data. The thermocouples and platinum resistance sensors are calibrated at 0 °C using an ice bath, and the FBG sensors are calibrated using a temperature sequence inside the ESPEC LU-114 thermal chamber, like the process outlined in chapter three.

4.2.3.1 Thermocouple Data Logger Calibration

The PicoLog TC-08 allows up to eight TC sensors for simultaneous data logging. The device is used with the Picolog software to display and output the recorded data as CSV files. The data is then synced with the battery data using the timestamp associated with the logged data.

Although purchased brand new for this study, it is important to verify the accuracy of the data logger to ensure the TC sensor results are comparable to the FBG temperature response. The accuracy of the TC-08 logger is conducted with a MICROCAL 2 K-type thermocouple simulator (Figure 4.2-4), which provides a reference voltage to the logger related to a temperature level experienced by the TC sensor. The calibration certificate for the thermocouple simulator is shown in Appendix A.

Figure 4.2-4: MICROCAL 2 Thermocouple Simulator.

Table 2 shows the response from each of the eight channels on the TC-08 device for -20 °C, 0 °C, 10 °C, 50 °C, and 100 °C temperature intervals defined by the MICROCAL device. Each temperature interval is recorded for 10 minutes with temperature logged once per minute. The MICROCAL 2 device can simulate for up to 1000 °C at pre-programmed intervals, however, the range described is suitable for the temperature experienced by the LIB cells under testing, thus temperatures above 100 °C are not considered in the calibration.

Showing 10-minute average data for each channel at each temperature point, and standard deviation of all channels. Table 2 shows an average temperature

within the 0.5°C uncertainty for each channel, thus all temperature data recorded from the TC-08 will adopt a 0.5 °C uncertainty factor.

Table 2: *TC-08 Callibration Data*

	TC-08 Channel Calibration with MICROCAL 2									
Set Temperature (°C)	Channel 1 (°C)	Channel 2 (°C)	Channel 3 (°C)	Channel 4 (°C)	Channel 5 (°C)	Channel 6 (°C)	Channel 7 (°C)	Channel 8 (°C)	Channel Average (°C)	Standard Deviation
-20	-19.85	-19.94	-20.10	-20.29	-20.36	-20.20	-20.05	-19.88	-20.085	0.188
0	0.17	0.04	-0.06	-0.27	-0.31	-0.12	0.04	0.14	-0.046	0.176
10	10.17	10.05	9.95	9.75	9.70	9.89	10.03	10.13	9.957	0.173
50	50.20	50.10	50.01	49.81	49.69	49.92	50.10	50.17	50.002	0.182
100	100.23	100.13	100.06	99.91	99.73	99.96	100.17	100.23	100.051	0.176

Average of 10 minutes recording per channel, standard deviation of all eight channels per set temperature.

4.2.3.2 Thermocouple and Platinum Resistance Sensor Calibration

Shown in Figure 4.2-5, the thermocouples and platinum resistance sensors are checked to obtain their variation at zero degrees Celsius to be certain they function within tolerance. They are subject to zero degrees Celsius for over two hours in an ice-filled vacuum flask. The sensors are housed in a thin glass test tube to avoid moisture contact, they are then fed through a hole in the insulated lid and connected to the relevant data logger (Pico Technology TC-08 and Pico Technology PT-104), the hole is covered with a soft insulating material. Once the sensors reach a stable temperature the data is logged for 60 minutes at 1 Hz, this is used to calculate the mean and standard deviation of the sensor response.

A total of eight K-type TC sensors and three 4-wire B-class PT sensors (manufactured by LAB FACILITY, purchased from Farnell UK) are used for the calibration, where all sensors used for the experimental findings are of identical type. It is found that for the 60-minute duration the PT sensors have a mean of 0.0425 °C, with a standard deviation of 0.0183 °C, while the TC sensors have a mean of 0.0061 °C with a standard deviation of 0.0148 °C. Both sensor types have a very similar standard deviation over the 60-minute duration, however, it is shown that the TC sensors hold closest to zero degrees.

(a)   (b)
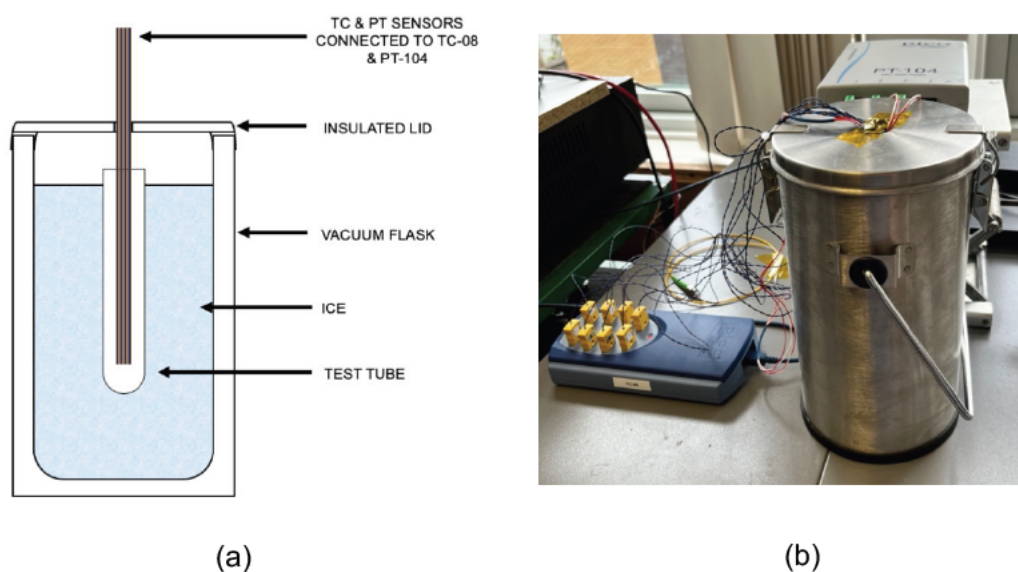
Figure 4.2-5: Sensor Callibraton at 0 °C (a) schematic of setup witth Ice Bath in Vaccum Flask, and (b) picture of setup with the PicoTech TC-08 Data logger.

Figure 4.2-6 (a) shows the response of the eight TC sensors and Figure 4.2-6 (b) shows the response of the three PT sensors. The sensors fall within their respective error margins of 0.5 °C and 0.3 °C for TC and PT respectively. It is important to note that the PT sensors' uncertainty changes from 0.3 °C at zero degrees Celsius to 0.8 °C at 100 degrees Celsius, thus the data in this chapter will show the maximum uncertainty of 0.8 °C for all PT sensor data.

(a)

(b)
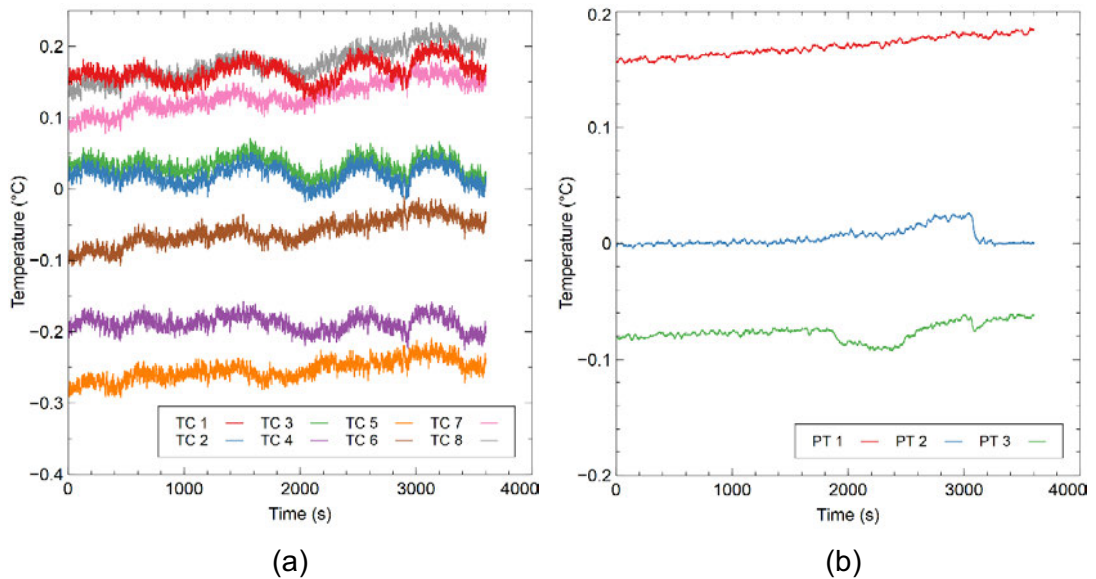
Figure 4.2-6: Sixty minute data for zero degrees callibration of (a) eight K-type TC sensors and (b) Three 4 wire class B PT sensors.

4.2.3.3 In-Situ Fibre Bragg Sensor Calibration

The FOS with five FBG sensors attached to the battery pack with the 3D printed plinths is subject to a variable temperature sequence in the ESPEC LU-114 low-temperature chamber. The temperature is increased from 20 °C to 55 °C at 5 °C increments, and the temperature is held at each temperature increment for a minimum of 30 minutes, during this time, the wavelength shift (nm) is recorded at a rate of 1 Hz, this data is then used to obtain an average wavelength shift for each temperature increment, plotted in graphical form (Figure 4.2-7), this shows the response of each FBG sensor along the FOS strand. It shows a good correlation with FBG response to the exposure temperature.

If the response of the FBGs for this calibration is compared to the response seen from the previous calibration i.e. comparing Figure 4.2-7 to Figure 3.2-3 (a), it is seen that the chamber used in this chapters calibration is less volatile when

holding a constant temperature. This is due to the ESPEC LU-114 temperature being purpose-built and designed for this application. Whereas the chamber used in the previous chapter is a DIY chamber made from a benchtop freezer using off-the-shelf parts.

As detailed in Chapter 3, equation 9 is used to obtain the temperature change experienced by the FBG sensors. In this case, the resultant sensitivities of 9.463 pm, 9.562 pm, 9.623 pm, 9.688 pm, and 9.721 pm for FBG 1, FBG 2, FBG 3, FBG 4 and FBG 5 respectively. The reference Wavelength is 1523.157 nm for FBG 1, 1536.11 nm for FBG 2, 1546.062 nm for FBG 3, 1553.229 for FBG 4 and 1563.103 for FBG 5.
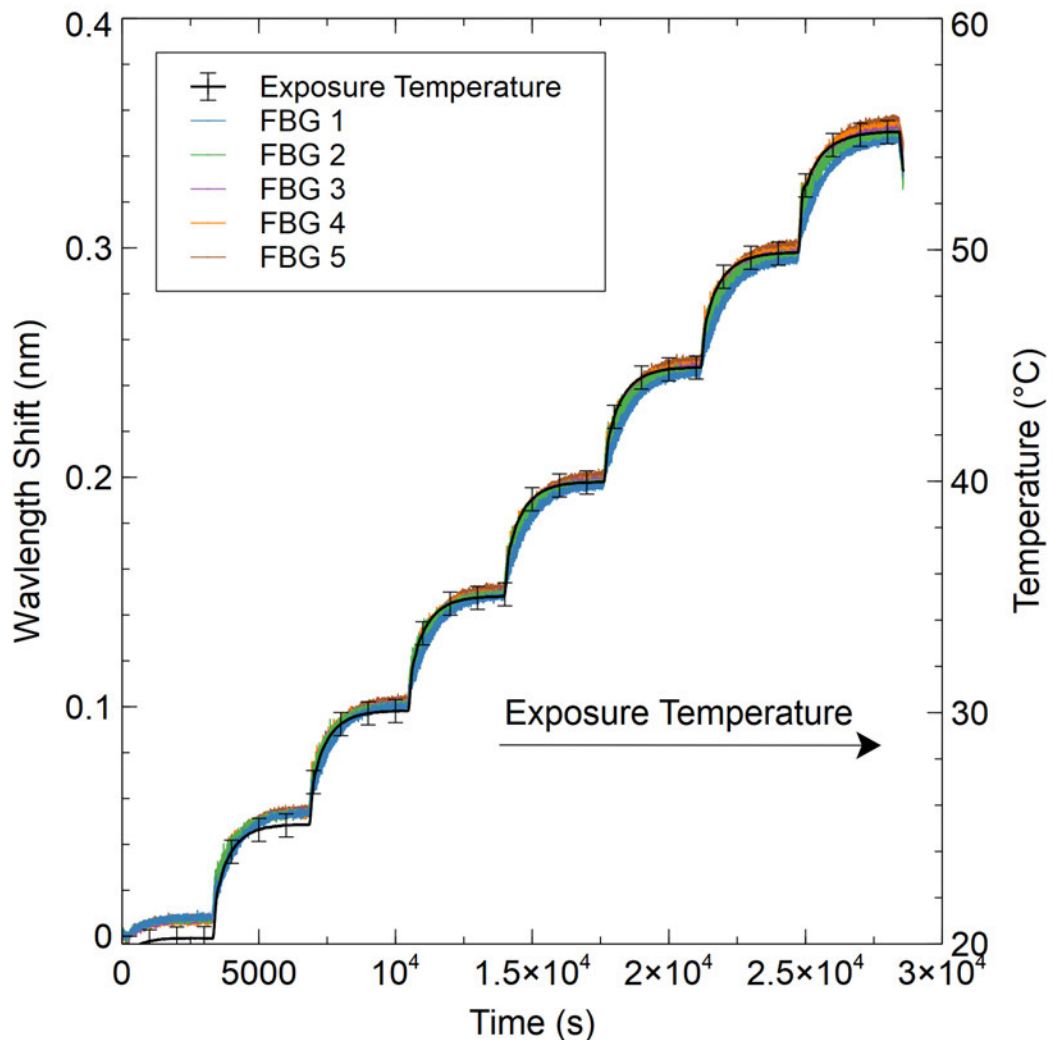
Figure 4.2-7: Wavelength shift over the calibration temperature variaton. Showing exposure temperature and each FBG wavelength shift. nm = nanometers.

4.2.4 Testing Regime

The three-cell battery pack with attached sensors is discharged at 0.5 C, 2 C and 40 CW until the 2.5 V cut-off voltage is reached. The 0.5 C and 2 C discharge conditions will induce a different level of heat generation as 2 C has a higher constant current draw, whereas the constant power discharge will induce an increasing current change during the voltage decrease, as discussed in the previous chapter.

The three discharge conditions will induce a different temperature change in the cells in the battery pack. It is expected that the 2 C discharge at a constant high current discharge will induce the highest temperature change, whereas the 0.5 C will induce the lowest and the 40CW test will show a temperature change somewhere in between the 0.5 C and 2 C discharge. This will provide suitable data to assess the effectiveness of the FBG sensors against the traditional sensors for individual cell level monitoring.

4.3 Results

The response of the FBGs is directly compared to the TC and PT sensors to determine their ability to record the cell temperatures of the battery pack successfully and accurately with the guide tube and plinth mounting method. The results of the testing regime are presented, where each test is analysed individually, and a discussion of all experiments is presented.

4.3.1 0.5 C Discharge

A 0.5 C discharge is conducted where a constant draw of 4.8 A induces an average temperature change of 9.33 °C, 9.24 °C and 8.41 °C for cell 1, cell 2, and cell 3 respectively. Figure 4.3-1 shows the temperature change response from each sensor as the capacity increases throughout the discharge. Generally, the sensors follow the same temperature change pattern over the three cells.
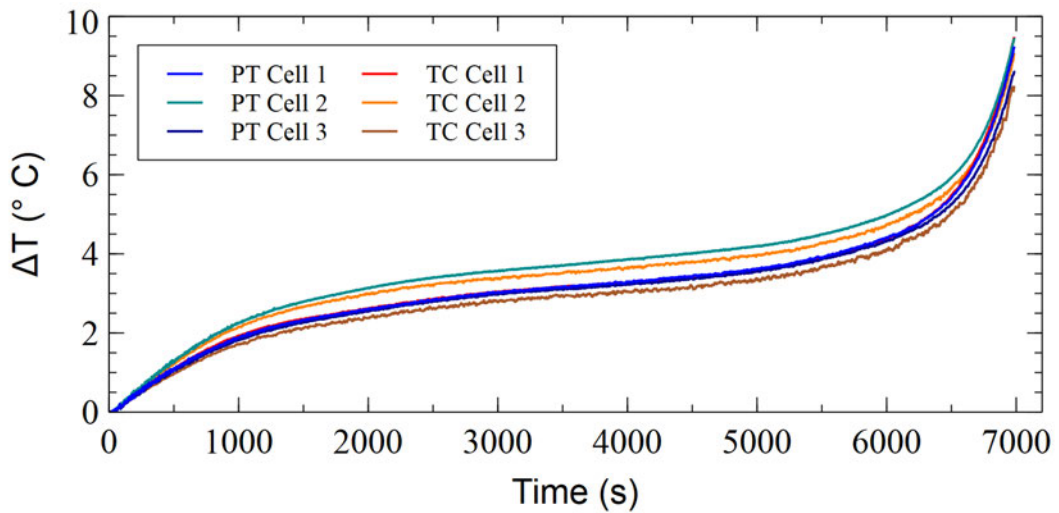
Figure 4.3-1: TC and PT temperature differential induced by 0.5 C discharge, Achieved Capacity = 9.302 Ah.

Figure 4.3-2 presents the difference in final temperature and temperature change (ΔT) experienced by the respective sensors of the cells at the end of the discharge. The TC sensors show an error bar of 0.5 °C uncertainty and the TC sensors 0.8 °C, relating to the specific accuracies of each sensor, as discussed earlier in this chapter.

It is shown in Figure 4.3-2 (a), that in the case of cell 1 and cell 3, the FBG response sits within the uncertainty of both traditional sensors. It is shown for Cell 1 that FBG 1 is almost identical to the PT sensor with a 0.012 °C differential,
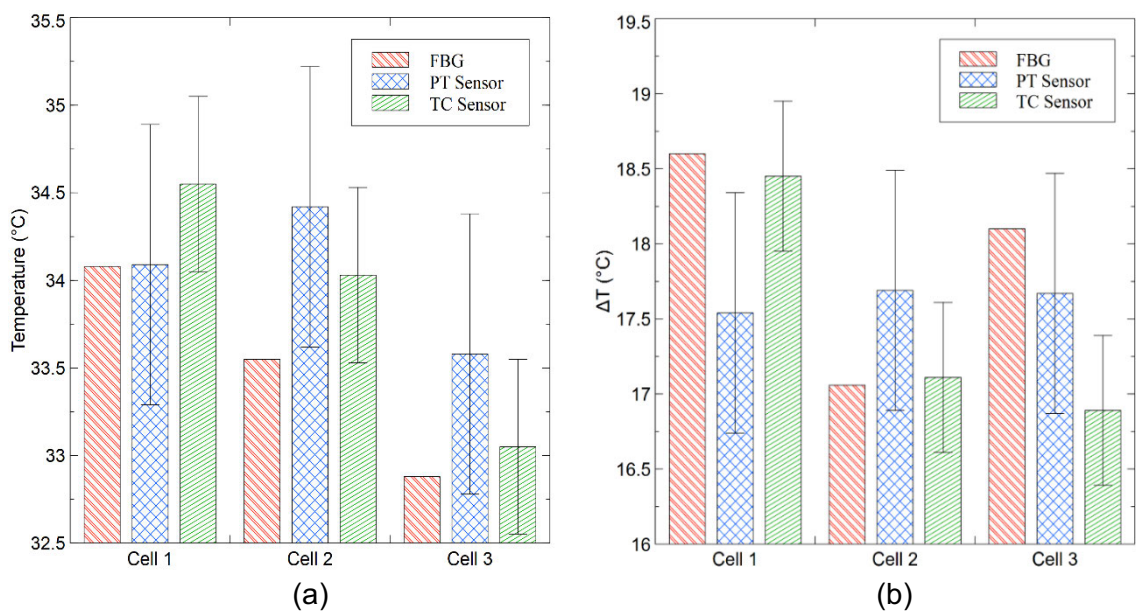
Figure 4.3-2: 3-Cell Battery Pack Discharge at 0.5 C; (a) Final recorded temperature for each of the sensor types, and (b), temperature change experienced by each sensor over the discharge period. Uncertinty of 0.8 °C and 0.5 °C for the PT and TC sensors respectively.

and is marginally off the lower TC error by 0.029 °C. The response of FBG 5 situated on cell 3 compares well to the TC and PT sensor, reaching a final value of 32.87 °C compared to 33.04 °C and 33.58 °C for the TC and PT sensors respectively. It is shown, however, that the response of FBG 3 situated on cell 2 is lower than the PT sensor, 0.071 °C from the lower PT uncertainty and is marginally within the lower TC uncertainty by 0.025 °C.

A comparison of the temperature change is shown in Figure 4.3-2 (b), which negates any temperature differential experience at the start of the discharge, showing the temperature change over the discharge period. It is shown that two FBG sensors are within the error margins of at least one of the traditional sensors, and for cell 2, FBG 3 is within the error margins of both the TC and PT sensors.

Regression analysis results are shown in **Table 3**, comparing each FBG with the corresponding traditional sensor on each of the three cells. In all cases, the analysis shows an excellent correlation between the FBG and respective sensors, with R^2 values upward of 0.98. The standard error does show higher for cell 3 for both sensor types when compared to cell 1 and cell 3.

The response of each sensor for each of the battery cells is shown in Figure 4.3-3 where capacity is shown on the x-axis, it is shown that for each cell, there is a good agreement between the FBGs and respective TC and PT sensors. It is shown that all the FBGs sit close to the uncertainty of the PT sensors which

Table 3: Regression Analysis for 3 Cell LIB pack at 0.5 C Discharge

	Regression Data (R^2)		
Sensor	FBG 1 (Cell 1)	FBG 3 (Cell 2)	FBG 5 (Cell 3)
Thermocouple (TC)	0.997	0.987	0.993
Platinum Resistance (PT)	0.996	0.986	0.991
	Regression Data (Standard Error)		
Thermocouple (TC)	0.203	0.438	0.308
Platinum Resistance (PT)	0.232	0.478	0.349

is also confirmed by the standard error from the regression analysis.

In addition to the three FBG sensors located individually at each cell, there is an FBG located between each cell, FBG 2, located between cell 1 and cell 2, and FBG 4, located between cell 2 and cell 3. Figure 4.3-4 shows the response of these FBGs, It is shown that they have a much larger deviation from the PT and TC sensors on the adjacent cells. This not only shows the temperature variation between the cells but the effectiveness of the FBGs located on the cells. As when compared to the respective sensors, these FBGs do not stay within the uncertainty factor associated with the sensors.
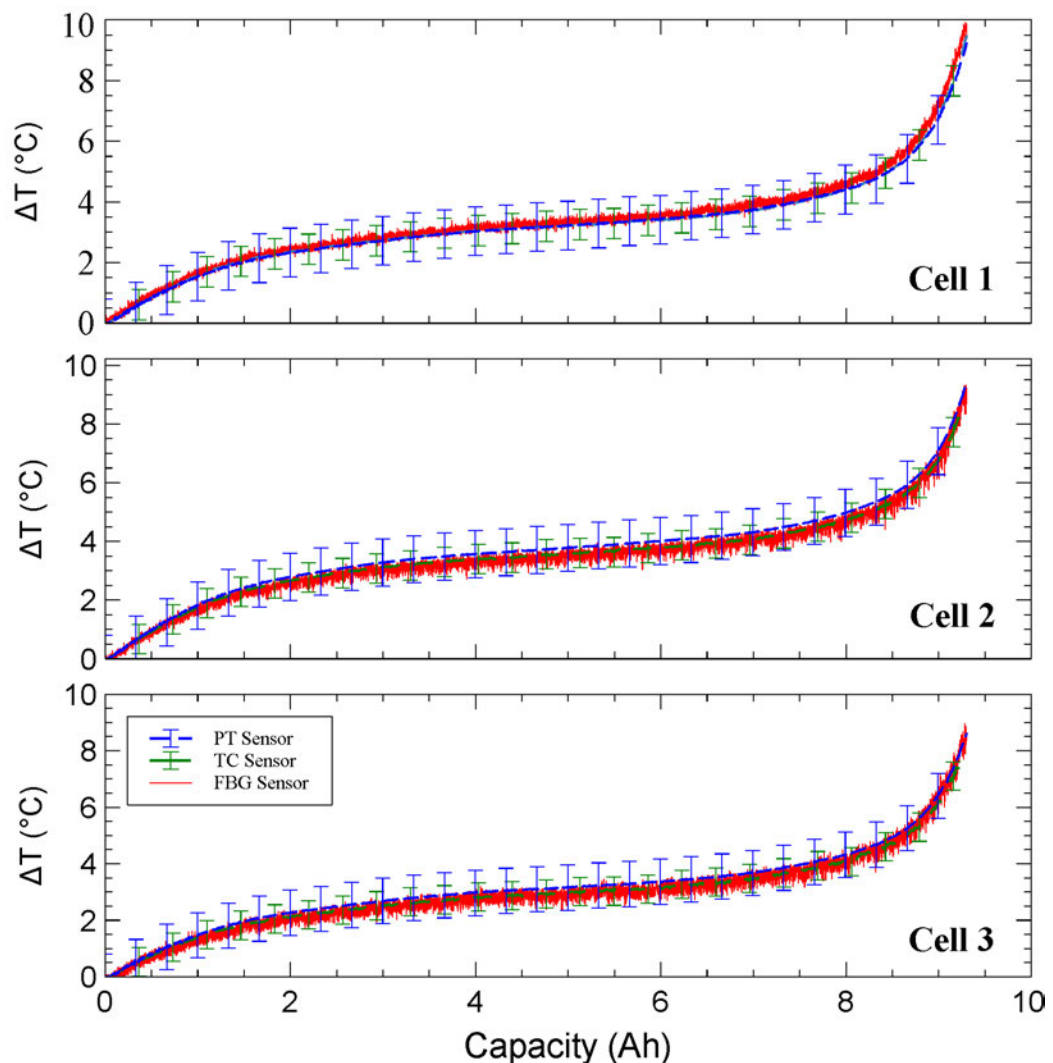
Figure 4.3-3: Comparison of sensor response for 1 C. Plotted against capacity, showing each cell individualy, where FBG1, FBG 2, and FBG 3 are relted to cell 1, cell 2 and cell 3 respectively
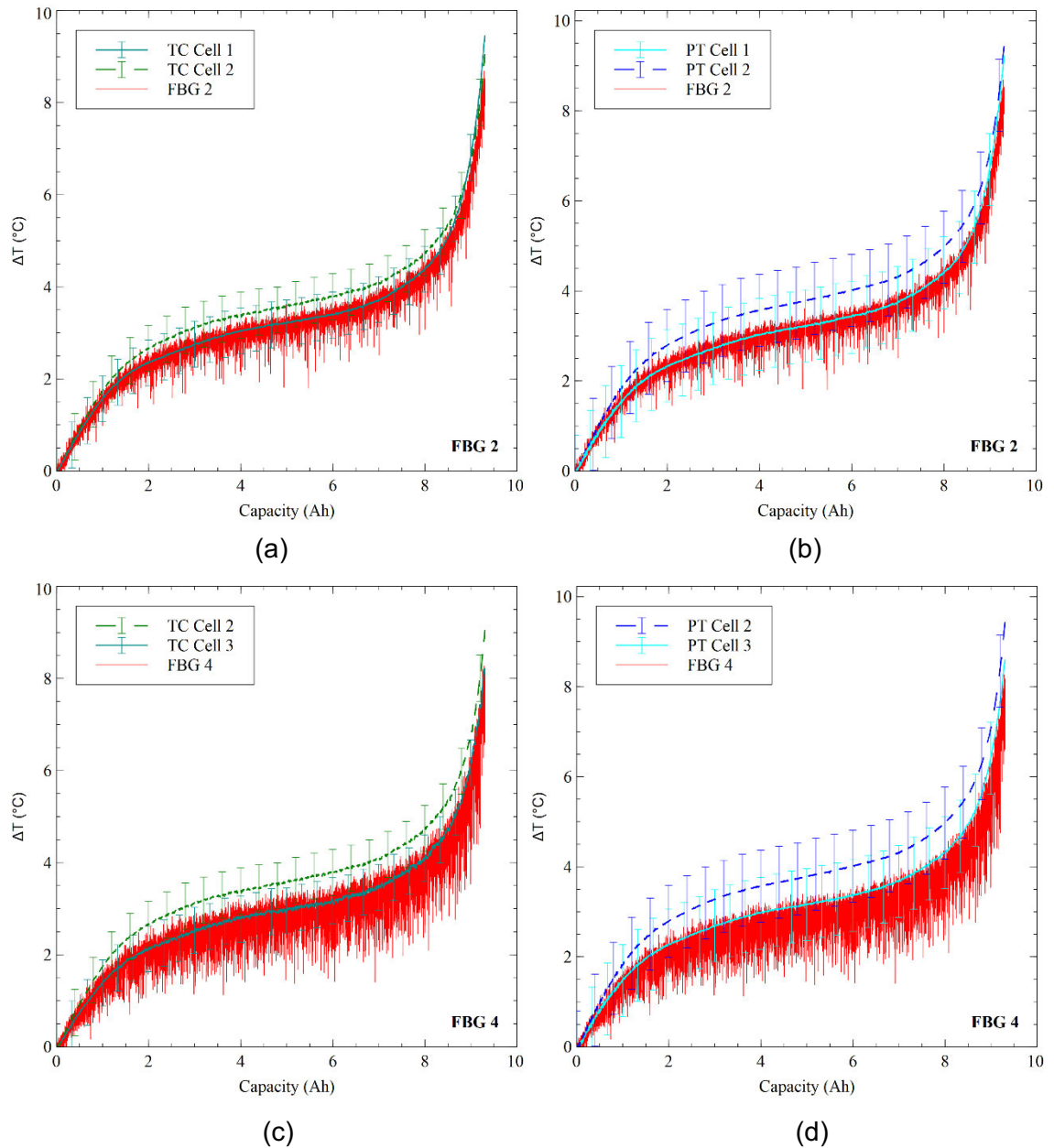
Figure 4.3-4: Comparison of FBG 2 and FBG 4 and relevant traditional sensors during 0.5 C discharge; (a) FBG 2 with TC sensors on cell 1 and cell 2, (b) FBG 2 with PT sensors on cell 1 and Cell 2, (c) FBG 4 with TC sensors on cell 2 and cell 3, and (d) FBG 4 with PT sensors on cell 2 and cell 3. Where FBG 2 is situated between cell 1 and cell 2, and, FBG4 situated between cell 2 and cell 3.

4.3.2 2 C Discharge

The 2 C discharge with a constant current of 19.2 A induces an average temperature change of 40.05 °C, 47.07 °C and 41.37 °C respectively for cell 1, cell 2, and cell 3 of the battery pack. Which is an increase of 30.72 °C for cell 1, 37.83 °C for cell 2 and, 32.96 °C for cell 3, compared to the 0.5 C discharge conditions. Figure 4.3-5 shows the responding temperature change from each sensor as the discharge capacity increases. Similarly, to the 1 C discharge

(Figure 4.3-1) the TC and PT sensors generally show the same response throughout the discharge.

The 2 C discharge shows that cell 2 has the largest overall final temperature and temperature change during the discharge period. Figure 4.3-6 (a) shows the final temperature of each cell recorded by the three sensing methods, moreover, Figure 4.3-6 (b) shows the temperature change for each cell. The FBG sensors show good response in line with the traditional sensors, for example, cell 1 and cell 2 are lower than cell 3, and the corresponding FBG sensors also reflect this pattern.
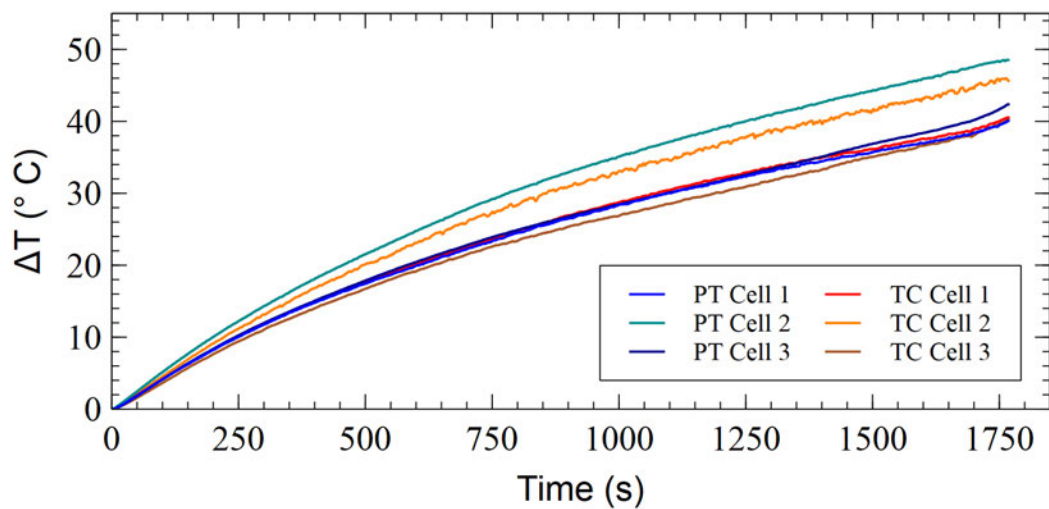
*Figure 4.3-5: TC and PT temperature differential induced by 2 C discharge, Achieved Capacity = 9.424 Ah.*

Figure 4.3-6: 3-Cell Battery Pack Discharge at 2 C; (a) Final recorded temperature for each of the sensor types, and (b), temperature change experienced by each sensor over the discharge period. Uncertinty of 0.8 °C and 0.5 °C for the PT and TC sensors respectively

Cell 2 has the highest response seen in the FBG sensors, reaching 72.53 °C with a temperature change of 47.53 °C recorded at the cell. The FBG sensor (FBG 3) shows to be 0.19 °C from the lower uncertainty of the PT sensor, however, it overshoots the upper TC uncertainty by 1.40 °C. The other two cells are more agreeable where FBG 1 at cell 1 overshoots both the TC and PT sensors' uncertainty by 0.30°C and 0.77 °C respectively.

The FBG sensors show agreeability with the traditional sensors on each cell throughout the discharge, which can be seen further in Figure 4.3-7 where each sensor is plotted against capacity. The FBG response shows excellent alignment with the other sensors for cell 1 and cell 3, for cell 2 however, there is a greater deviation in the response, which corresponds with maximum and delta temperatures shown in Figure 4.3-6 (a) and (b).

Table 4: *Regression Analysis for 3 Cell LIB pack at 2 C Discharge*

Regression Data (R^2)			
Sensor	FBG 1 (Cell 1)	FBG 3 (Cell 2)	FBG 5 (Cell 3)
Thermocouple (TC)	0.999	0.993	0.994
Platinum Resistance (PT)	0.999	0.992	0.994
Regression Data (Standard Error)			
Thermocouple (TC)	0.284	0.748	0.546
Platinum Resistance (PT)	0.284	0.820	0.595

Regression analysis (**Table 4**) shows a high correlation between the FBG response and the respective sensor on each battery cell. The R^2 values show a minimum of 0.992 however a greater standard error is shown in comparison to the 1 C discharge. Similarly to the 1 C discharge, it is shown that FBG 3 has the higher error out of the three FBGs.
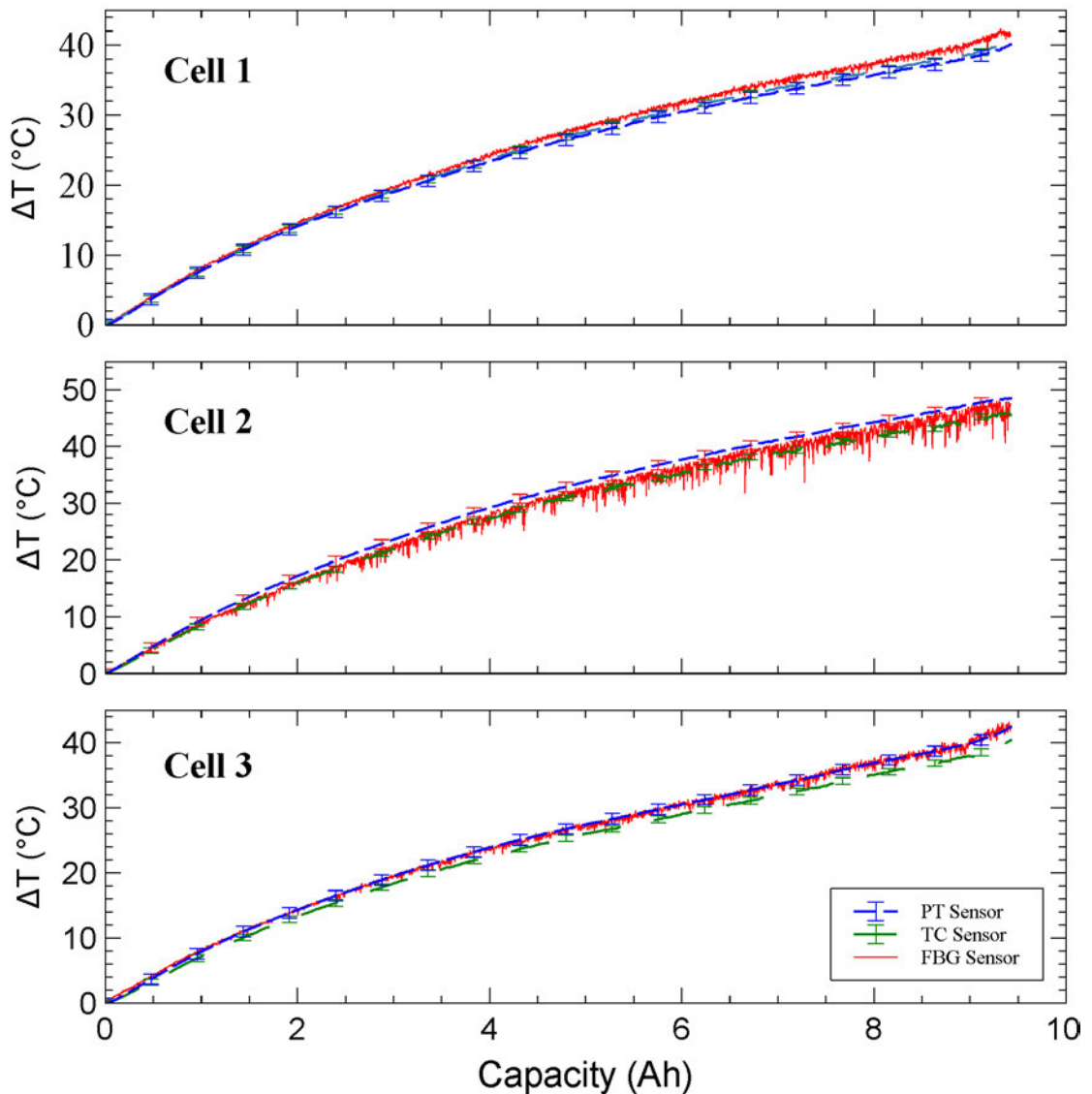
Figure 4.3-7: Comparison of sensor response for 2 C. Plotted against capacity, showing each cell individualy, where FBG1, FBG 2, and FBG 3 are relted to cell 1 , cell 2 and cell 3 respectively.

The FBGs between the cells, FBG 2, and FBG 4 show a more drastic deviation at the higher 2 C discharge compared to the response from the 1 C discharge. Due to the much higher temperature change at 2 C, it is shown that the median between the cells reaches 32.84 °C and 34.64 °C for FBG 2 and FBG 4 respectively. This reduced temperature can be seen against both the TC and PT sensors shown in Figure 4.3-8. Again, this shows that the FBGs located at the cell LIB cell surface are working as expected.
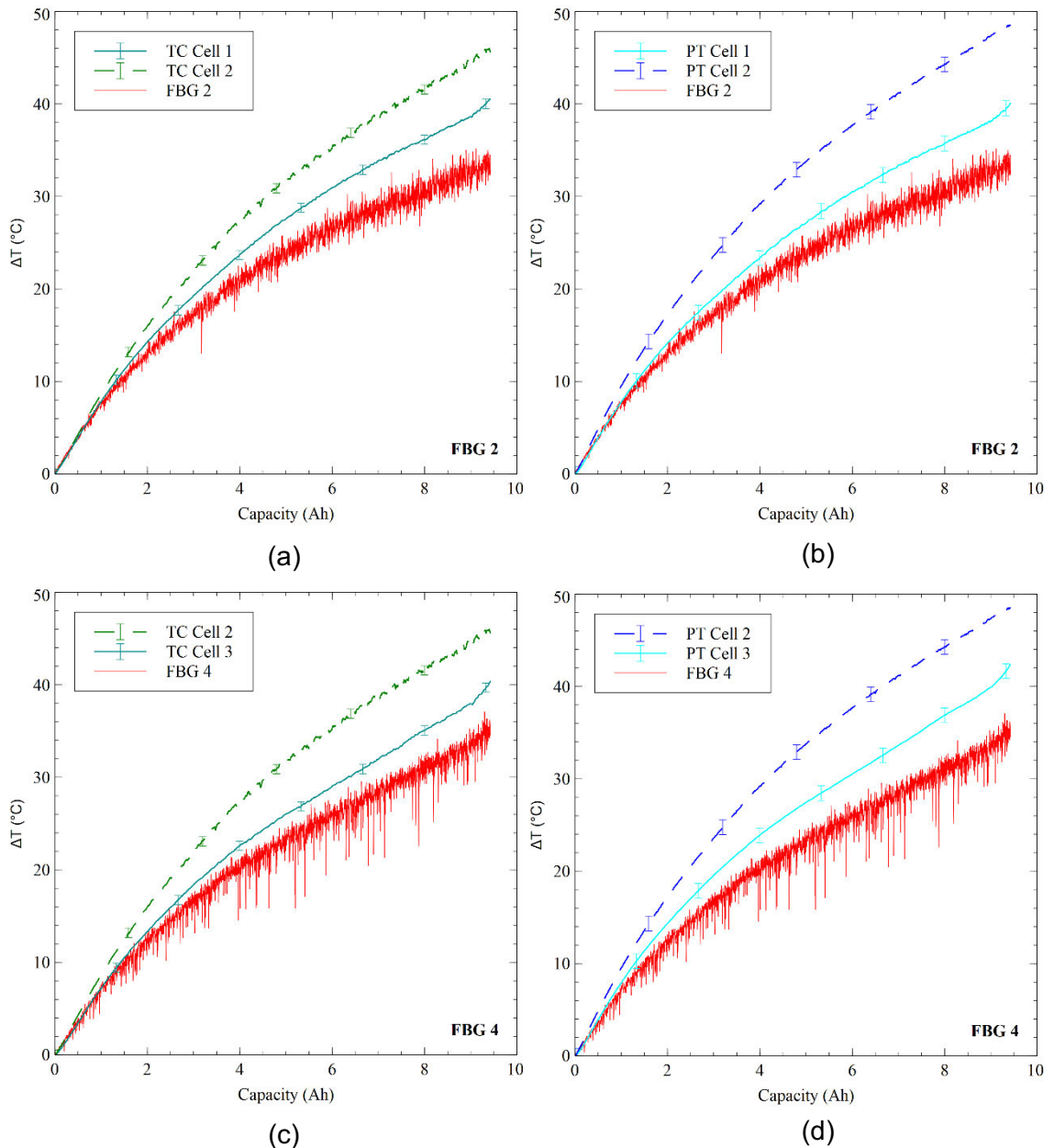
Figure 4.3-8: Comparison of FBG 2 and FBG 4 and relevant traditional sensors during 2 C discharge; (a) FBG 2 with TC sensors on cell 1 and cell 2, (b) FBG 2 with PT sensors on cell 1 and Cell 2, (c) FBG 4 with TC sensors on cell 2 and cell 3, and (d) FBG 4 with PT sensors on cell 2 and cell 3

4.3.3   40 Watt Constant Power Discharge

The 40 Watt CW discharges with an increasing current draw from 10.55 A to 16.12 A induce an average temperature change of 26.41 °C, 29.34 °C and 26.41 °C respectively for cell 1, cell 2, and cell 3. The CW discharge shows an increased temperature change when compared to 1 C discharge but does not reach the same level as 2 C. As discussed in the previous chapter, CW testing is crucial to understanding the behaviour of the battery cell at a constant power output with increasing current output.

Figure 4.3-9 shows the temperature change from each sensor as the current increases throughout the discharge. Similarly to 1 C discharge (Figure 4.3-1) the TC and PT sensors generally show the same response throughout the discharge.

The 40CW discharge shows similarities to the 2 C discharge i.e. cell 2 shows the highest temperature change and final temperature. This can be seen in Figure 4.3-10 (a) and (b), when comparing each sensor type across three cells. During this discharge, it is shown that the FBG response, FBG 1, is the only one to fall within the uncertainty of the traditional sensors, moreover, in this case only within the PT sensor uncertainty. FBG 1 shows a final temperature differential of 0.49 °C when compared to the PT sensor for cell, however, when compared to the TC sensor it shows a 2.96 °C differential, where the TC registers the higher temperature. For cell 2 and cell 3 it is shown that both the traditional sensors register a higher temperature than the respective FBG
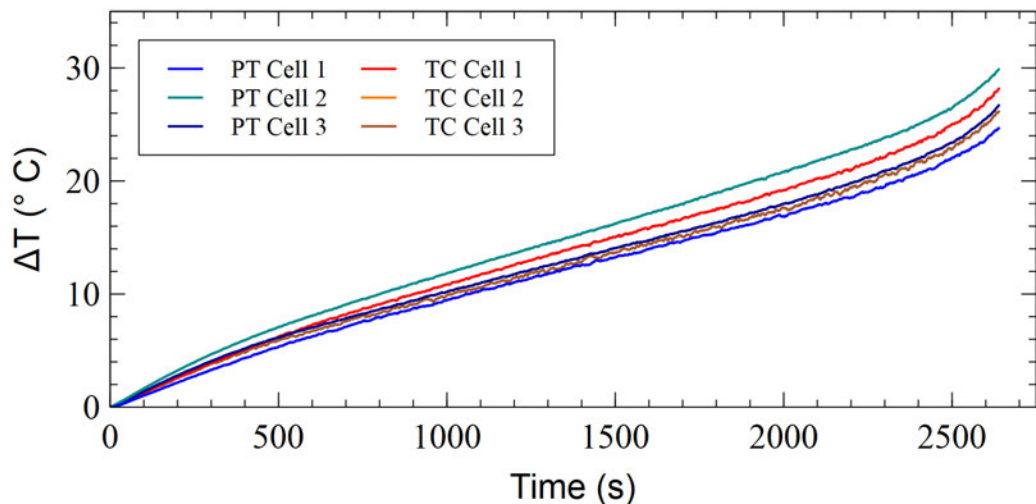
Figure 4.3-9: TC and PT temperature differential induced by 40 Watt CW discharge, achieved capacity = 9.059 Ah.

sensors. In all cases, the FBGS respond similarly to the traditional sensors i.e show higher temperature when the traditional sensors show higher and vice versa.

The regression analysis (**Table 5**) shows good comparability with the sensors and associated FBG with an R^2 value showing no less than 0.98, additionally, the standard error shows cell 2 to be higher than the adjacent cells within the battery pack.
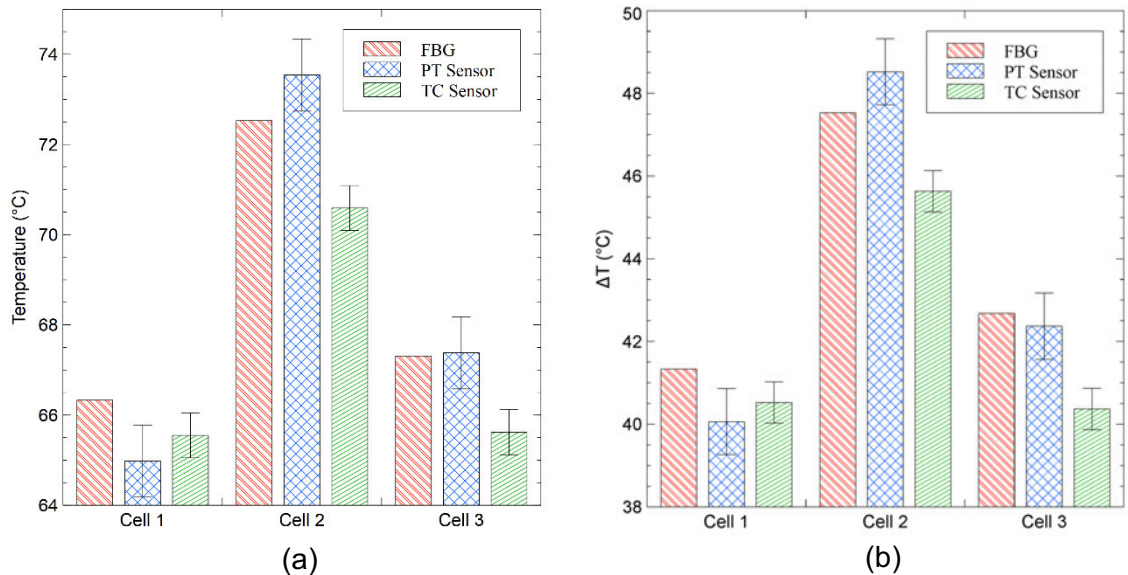

(a)   (b)
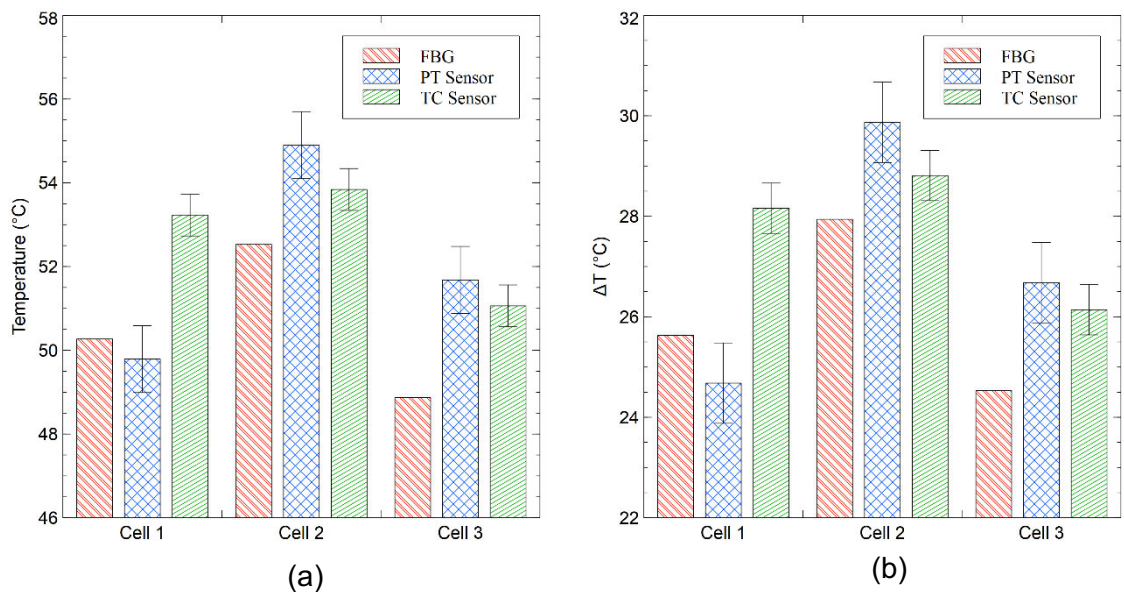
Figure 4.3-10: 3-Cell Battery Pack Discharge at 40 Watts CW; (a) Final recorded temperature for each of the sensor types, and (b), temperature change experienced by each sensor over the discharge period. Uncertinty of 0.8 °C and 0.5 °C for the PT and TC sensors respectively.

Table 5: Regression Analysis for 3 Cell LIB pack at 40W CW Discharge

Sensor	Regression Data (R^2)		
	FBG 1 (Cell 1)	FBG 3 (Cell 2)	FBG 5 (Cell 3)
Thermocouple (TC)	0.989	0.981	0.999
Platinum Resistance (PT)	0.989	0.981	0.999
	Regression Data (Standard Error)		
Thermocouple (TC)	0.220	0.494	0.344
Platinum Resistance (PT)	0.221	0.520	0.374

The overall response of the FBGs during the discharge period, Figure 4.3-11, shows that FBG 5 located on cell 3 has the least variation, whereas FBG 3 on cell 2 shows variation below both of the traditional sensors, and FBG 1 on cell
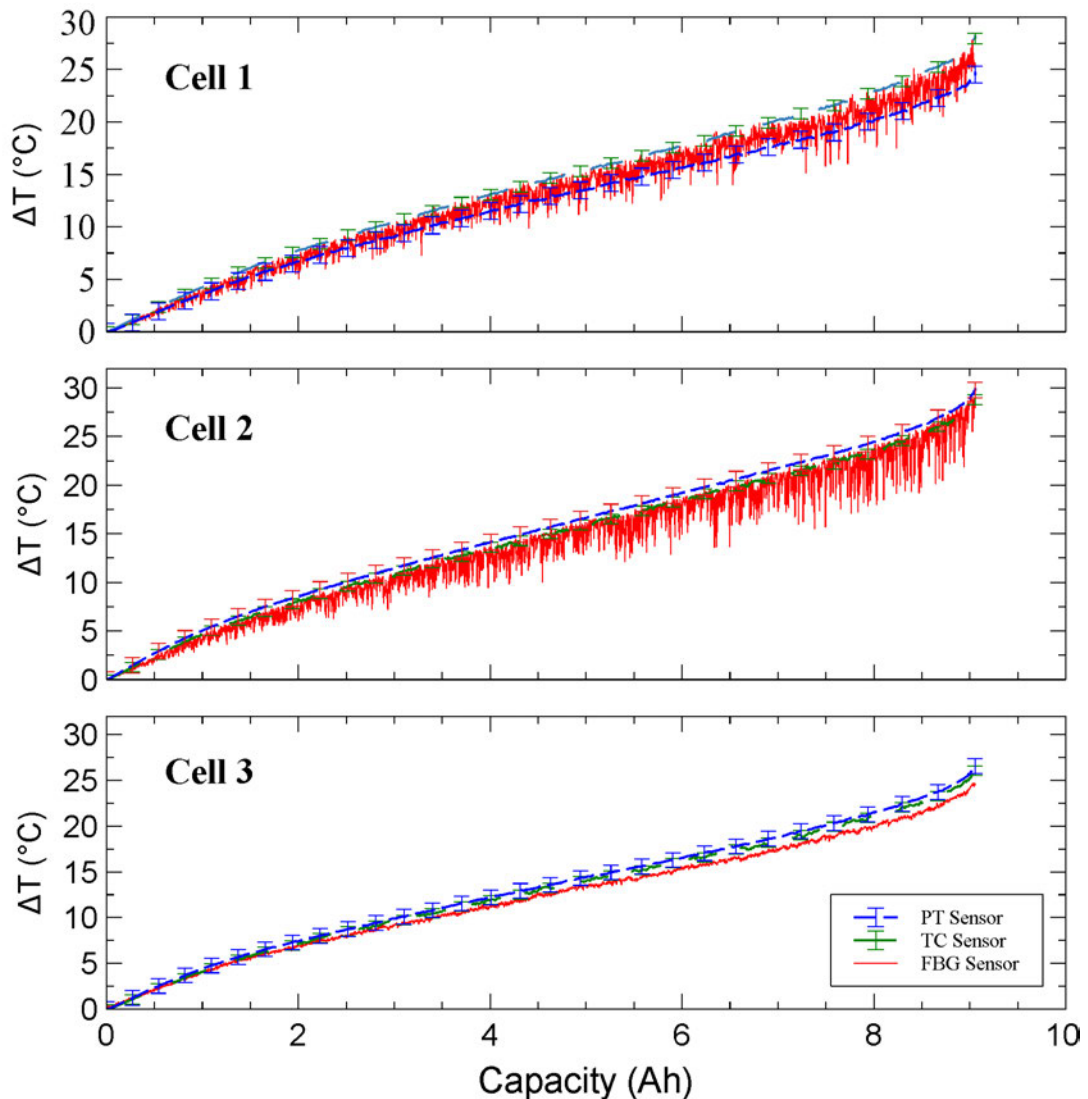
Figure 4.3-11: Comparison of sensor response for 40 Watt CW. Plotted against capacity withdrawn from the battery pack, showing each cell individualy, where FBG1, FBG 2, and FBG 3 are relted to cell 1 , cell 2 and cell 3 respectively.

1 shows the variation of FBG response to generally fall between the PT and TC sensors.

The FBG sensors between the cells, FBG2 and FBG 4, show again there is a discrepancy between the FBG temperature and the temperature of the cells on either side. It is seen that in most cases when compared to the traditional sensors, the FBGs sit within the two cells, however, there is a large variation seen. Similar to the response seen during the other two discharge conditions.

This can be seen in Figure 4.3-12, where the FBG response is compared to the traditional sensors on the cells on both sides.
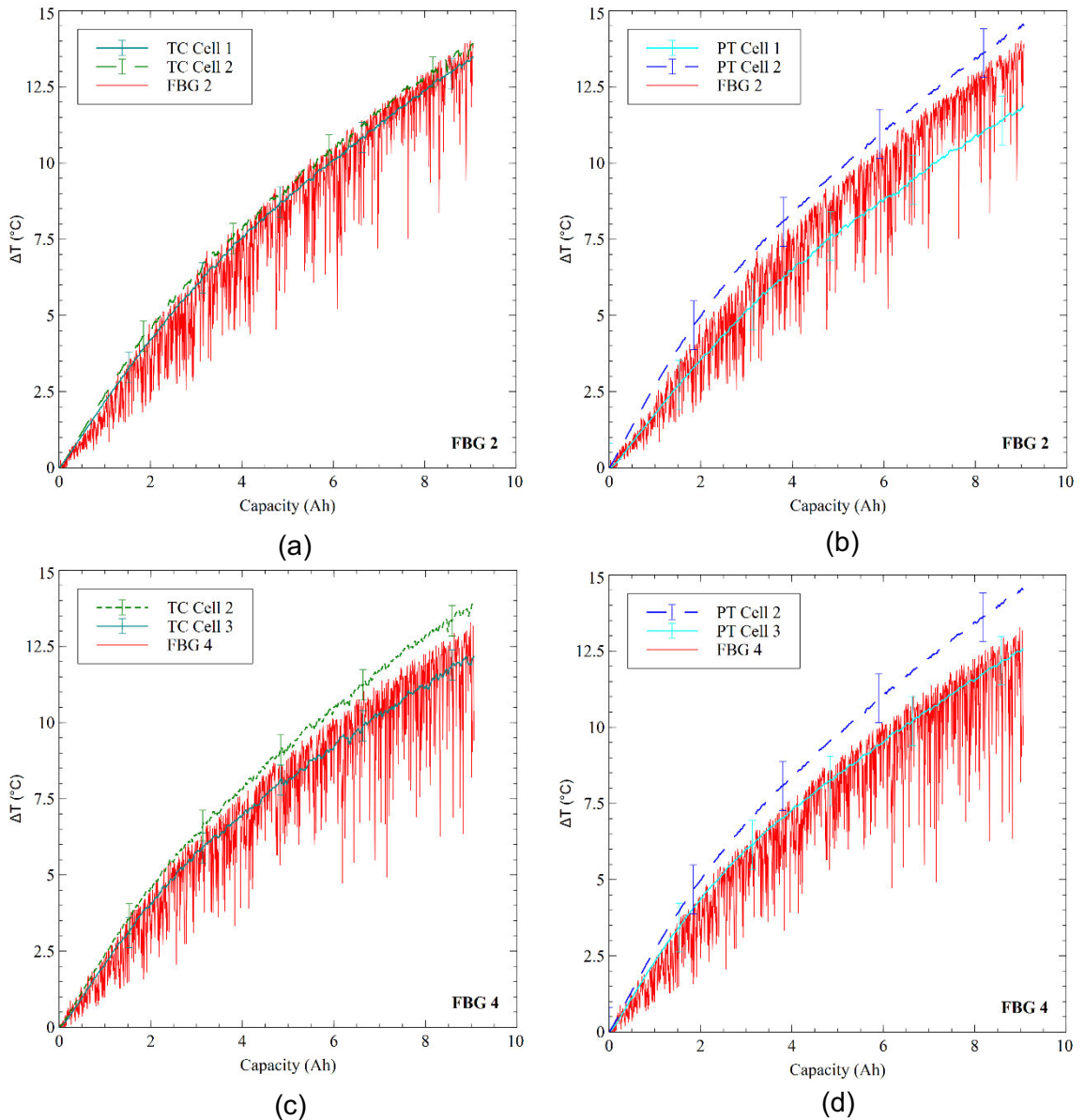
Figure 4.3-12: Comparison of FBG 2 and FBG 4 and relevant traditional sensors during 40 Watt CW discharge; (a) FBG 2 with TC sensors on cell 1 and cell 2, (b) FBG 2 with PT sensors on cell 1 and Cell 2, (c) FBG 4 with TC sensors on cell 2 and cell 3, and (d) FBG 4 with PT sensors on cell 2 and cell 3.

4.3.4 Overall Discussion

When the FBGs are compared to the traditional sensors in each discharge condition, it can be said that there is a good correlation between the sensor types, as can be seen by the linear regression, where over the three discharge conditions the lowest R^2 value is 0.981.

It is shown that during the 1 C discharge, the sensors are well-matched i.e. all FBG sensors across the three LIB cells are within, or very close to the uncertainty of the PT and TC sensors. The 2 C and 40CW discharge conditions provide more varied results due to the larger discharge current producing higher thermal gradients for each cell within the LIB pack. Due to the varied responses, it is important to analyse the maximum temperature recorded by each sensor during each discharge condition, as up to this point only the final temperature is analysed.

(a)

(b)

(c)
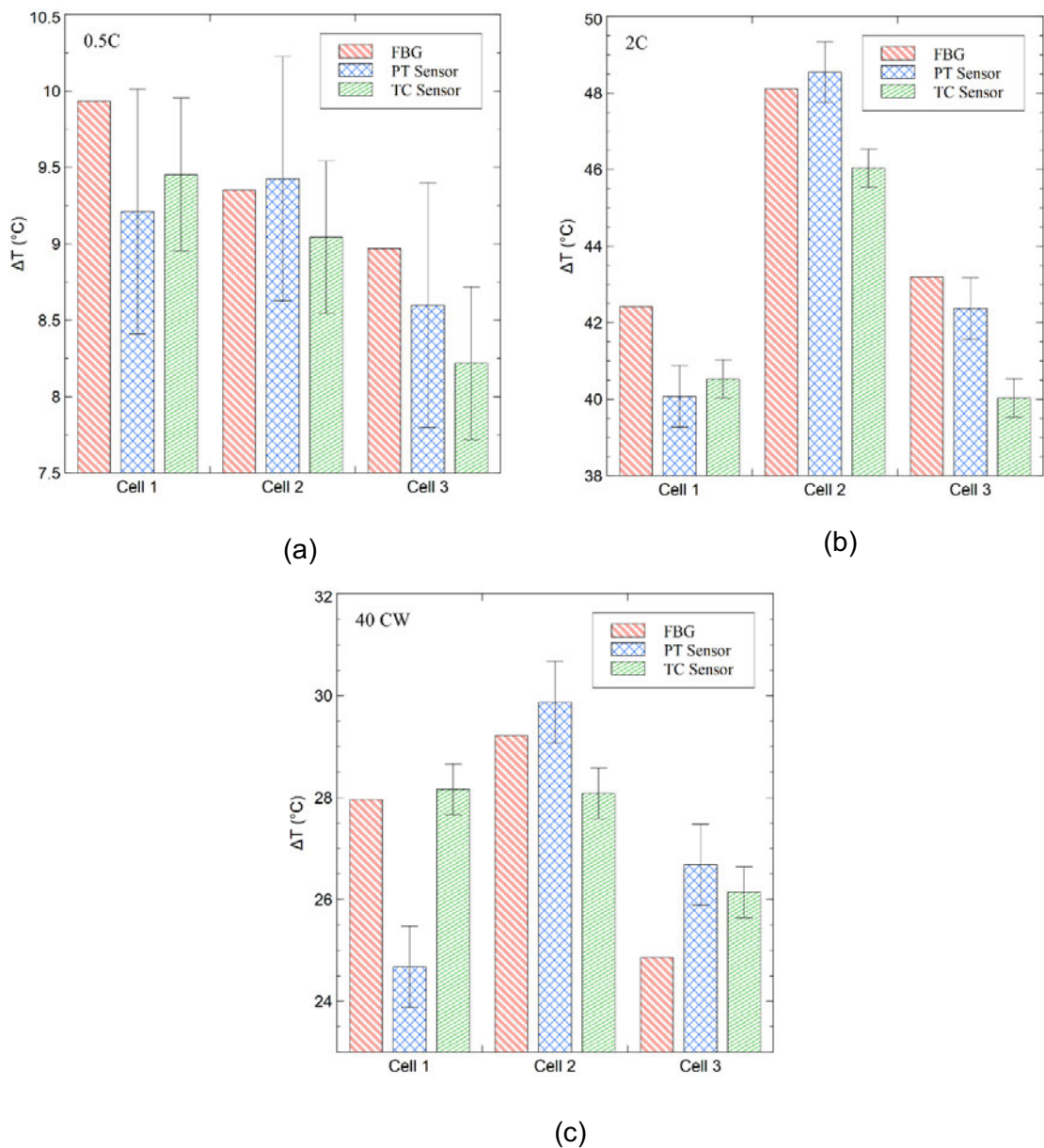
Figure 4.3-13: The maximum recorded temperature change over the three discharge conditions, (a) 0.5 C discharge, (b) 2 C discharge, and (c), 40 Watt CW discharge. Where each sensor on each of the three cells is compared. Showing the uncertianty factor of 0.5 °C and 0.8 °C for the TC and PT sensors respectiviely.
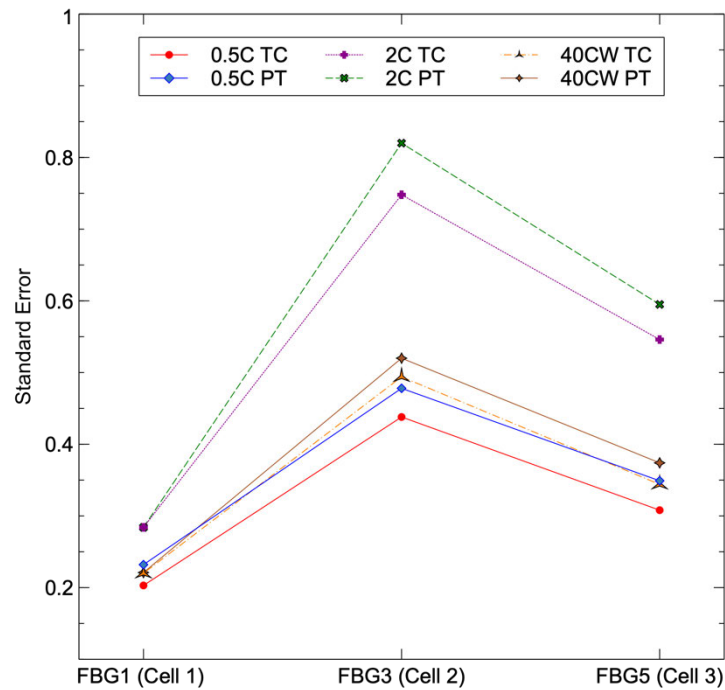
Figure 4.3-14: Linear Regression Analysis Standard Error, each sensor compared to respective FBG.

Figure 4.3-13 shows the maximum temperature recorded for each sensor over the three discharge conditions. It is shown that there are only 2 occurrences where the respective FBG sensor is not within the uncertainty of at least one of the traditional sensors; FBG 1 on cell 1 during the 2 C discharge (Figure 4.3-13 (b)), and FBG 5 on cell 3 during the 40 CW discharge (Figure 4.3-13 (c)). This provides enough certainty that the described mounting method with guide tube is sufficient to provide accurate temperature data for individual cell level monitoring.

To fully scrutinise the technique, it is important to discuss the standard error generated from the linear regression conducted for each discharge condition. Figure 4.3-14 shows the standard error for the PT and TC sensors in correlation to their respective FBG. It is shown that for the lowest discharge the relative error is minimal when comparing across the three cells individually, however, this cannot be said for the 2 C and 40CW discharge. It is evident that during higher discharge conditions the standard error is increased when there is an increased temperature differential. It is shown that in both the 2 C and 40CW discharge cell 2 has the highest standard error, thus it can be hypothesised that FBG 3 is more susceptible to deviation potentially caused by the slack in the FOS strand over the battery cells. As FBG 1 and FBG 5 have the plinths to

provide localised support, the middle FBG, FBG 3, does not have this support, thus the lack of FOS strand support in this region could interfere with the temperature readings, as is documented in the literature, bending of the FBG can induce strain. As this section of the fibre does not have a microtube encapsulating it to keep the FBG level, it is reasonable to assume this is the case.

In each discharge it is shown that the FBGs placed at the cell spaces show a reduced temperature reading, this demonstrated the effectiveness of the FBG placed at the cell as they are experiencing higher temperature deviations. This further demonstrates the effectiveness of the FBG sensors' suitability for individual cell level monitoring, furthermore, it is possible to use FBGs for measurements beyond the cell to gather more information surrounding the battery pack.

The overall maximum temperature readings for each sensor per discharge condition are summarised in **Table 6** (below). Comparing the FBGs to both traditional sensors over the three discharge conditions It is calculated that the

Table 6: Maximum Recorded Temperature from each Sensor.

0.5 C Discharge			
Sensor	Cell 1	Cell 2	Cell 3
FBG	34.08	33.55	32.88
PT	34.09	34.42	33.05
TC	34.55	34.03	33.58
2 C Discharge			
Sensor	Cell 1	Cell 2	Cell 3
FBG	66.33	72.53	67.31
PT	64.98	73.54	67.38
TC	65.55	70.59	65.62
40 CW Discharge			
Sensor	Cell 1	Cell 2	Cell 3
FBG	50.27	52.53	48.87
PT	49.97	54.90	51.06
TC	53.23	53.84	51.68

All temperature data in degrees Celsius (°C).

average deviation for FBG 1 is 0.97 °C, with a minimum and maximum deviation of 0.01°C and 2.96 °C respectively. For FBG 3 at cell 2, it is calculated that the

average deviation is 1.33 °C, with a minimum and maximum of 0.48 °C and 2.37 °C respectively, while FBG 5 at cell 3 has an average deviation of 1.27 °C with a maximum and minimum deviation of 0.17 °C and 2.81 °C respectively. When considering the average deviation this is a significant improvement compared to the guide tube mounting method described in the previous chapter with a deviation of 2.15 °C, thus it is possible to acknowledge that the use of PTFE as a guide tube is significantly more effective than PVC when combined with the plinth mounting method.

4.4 Conclusion

This chapter successfully details the implementation of a FOS strand with five FBG sensors for the individual cell level monitoring of a 3-cell LIB pack. The use of the PTFE guide tube and ABS 3D printed plinths shows improved accuracy compared to the PVC guide tube detailed in the previous chapter, with an average error of 0.97 °C, 1.33 °C, and 1.27 °C for FBG1 on cell 1, FBG 3 on cell 2 and FBG 5 on cell 3 respectively, compared to 2.15 °C for the PVC guide tube.

It is shown that in addition to temperature measurement at the cell level, it is possible to capture temperature data between cells as demonstrated by the temperature response of FBG 2 and FBG 5 for each discharge, where a lower temperature was recorded in comparison to the FBGs situated at the cell surface. The higher variation seen in these FBGs could be used in the future to assess and investigate the radiating heat from cells within a battery pack. Due to the small dimensions and minimally invasive nature of FBG sensors, it is possible to situate FBGs within the small gaps between cells.

It is evident from the regression data, specifically the standard error that the FBG 3 response, situated in the middle of the mounted FOS strand shows a more varied response. It is possible to hypothesise that the larger error seen over the three discharge tests indicated a slack in the FOS which is minimally interfering with the temperature measurements. A possible solution for future work would be to apply a method to support the FBG around the cell without interfering with the FBG situated at the cell surface, additionally, a mechanical method to apply slight tension to the FOS strand across the cells would minimise

slack in the FOS, however, this must be able to allow expansion and contraction for the whole FOS strand to decouple the strain and temperature.

Chapter 5: Copper Plated Polymer Foam for Battery Thermal Management

5.1 Introduction

As discussed previously, in order to decrease and restrict the incidence of battery degradation and maximise LIB lifetime, it is recognised that the temperature gradients created by the use of a LIB must be regulated. Usually accomplished in industrial settings, such as in electric vehicles, by using forced air or indirect liquid cooling techniques. Phase change material and foam are increasingly explored for passive techniques for producing improved thermally conductive PCM/foam composites.

As previously stated, the research in this field typically uses copper, nickel, or aluminium foam for the fabrication of PCM/foam composites. Furthermore, there are few examples of plated polymer foam structures utilised with PCM materials, and at the time of writing this thesis, there are no known peer-reviewed research studies addressing the use of copper-plated polymer foams with PCM for thermal management of LIBs.

The most relevant studies avaiable in the literature related to this study show promising results when using a depsotion methodologies on foam structures, for example, A. Hussain et.al. present a study of graphene coated nickel foam saturated with paraffin as a novel material for thermal management of Li-ion batteries, resulting in 17% less surface temperature rise than with plain nickel foam [111].

Additionally, S. Inazawa et al. investigate the benefits of using a titanium redox process as a pure nickel electroless plating method compared to the conventional hypophosphite method. This study focuses on the development of an eco-friendlier method of nickel plating and details the process of plating urethane-based structures for applications in batteries.[112].

In order to address gaps in the literature due to the absence of research papers on polymer foam plating, particularly for the application of LIB thermal management, the following are suggested:

- Copper deposition of polyurethane foam for PCM impregnation using the electroless plating technique, which has not been documented for polymer foam substrates.
- This novel composite material will be employed for the passive thermal management of a LIB.
- As solid commercial foam has been employed in previous studies, the copper deposition mass will be adapted and examined in comparison to commercially available copper foam.

This will offer a solid proof of concept study for the application of PCM composts made from cooper-deposited polymer foam to the passive thermal management of LIBs.

5.2 Materials and Method

The following sub-sections describe the processes and methods used to manufacture the configurations of PCM/Foam composites. Additionally, the methodology of the experimental works carried out is detailed herewith.

5.2.1 Cell Thermal Characterisation and Monitoring

The battery cell used in this chapter is the EEMB Li-ion Polymer LP963450-PCM-LD Battery, this cell has a rated capacity of 1800 mAh and 3.7V nominal voltage.   Full battery specifications can be found in Appendix C: EEMB LP963450-PCM-LD Battery Data Sheet.

It is important to quantify the temperature gradient generated from this cell under various discharge conditions to select an appropriate discharge for the experimental study of Cu-P foam composites, the highest temperature being preferable.

The temperature of the cell is obtained by two K-type TCs, one glued to each side of the battery cell, as shown in Figure 5.2-1 (a) and (b). The temperature data is obtained using the Pico Technology TC-08 data logger, with the Picolog software, recording at 1 Hz. Figure 5.2-2 shows the temperature change (ΔT) of the battery cell during 1 C and 1.5 C discharge, it is shown that 1.5 C induces a
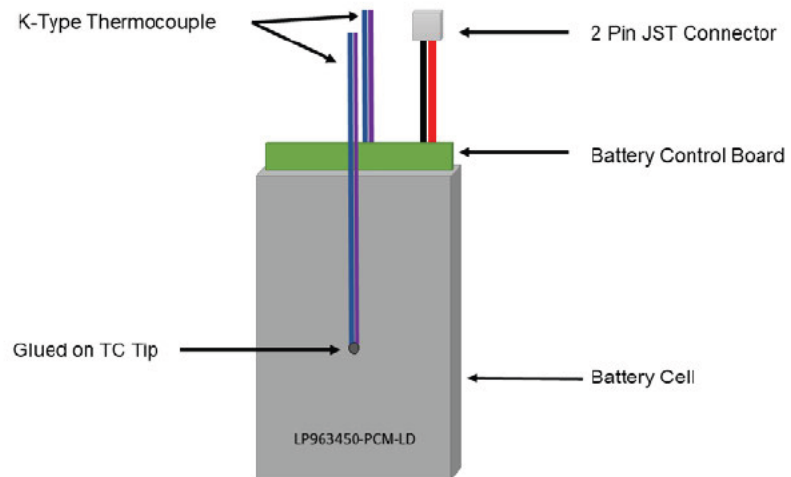
(a)

(b)

Figure 5.2-1: EEMB LIB (a) schamtic of the cell with K-type TC attached, identical at the reverse side, and (b) photograph of actual cell showing length of cell.
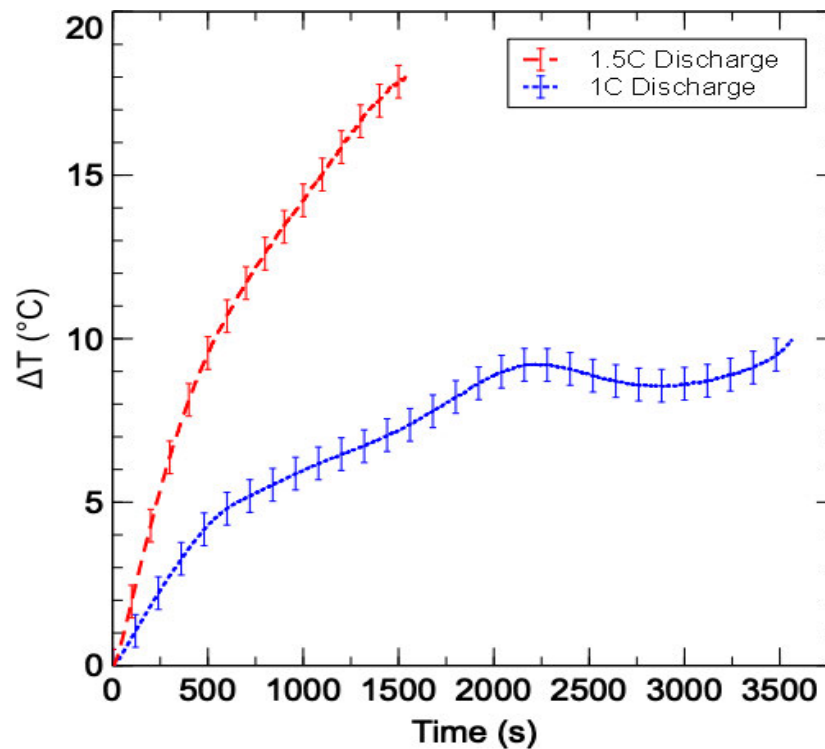
Figure 5.2-2: Thermal performance of Li-ion Polymer Battery at 1 C and 1.5 C discharge

more significant temperature change compared to 1 C, however as the current is increased, the discharge time reduces.

The 1.5 C discharge induces an 18 °C temperature change, whereas 1 C induces a 10 °C change. The data shown in Figure 5.2-2 shows the average of both TC sensors glued to the battery cell, the discharge occurs in the ESPEC LU114 low-temperature chamber at 25 °C, as detailed in the previous chapter.

As 1.5 C induces an 8 °C higher temperature change, this discharge rate is used for further tests to assess the effectiveness of the copper foam composite samples.

5.2.2 Phase Change Material Selection

Two commercial phase change materials obtained from Rubither GmbH, RT31 and RT42, are evaluated for use in the PCM foam composites. Since the battery cell begins discharge at 25 °C and concludes 18 °C higher, at 42 °C when discharged at 1.5 C, the PCM must function within this temperature range in order to absorb the heat produced by the cell. The specification described by Rubitherm GmbH, states the melt range of the RT31 PCM is 29 °C to 34 °C with
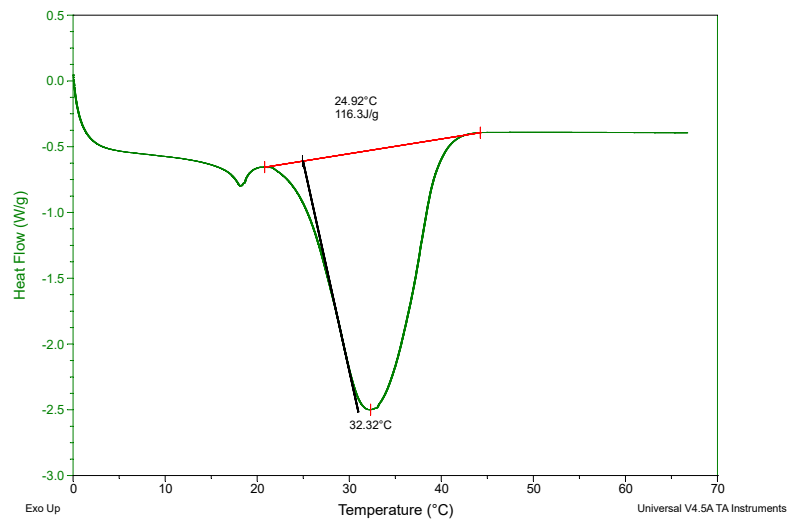
(a)
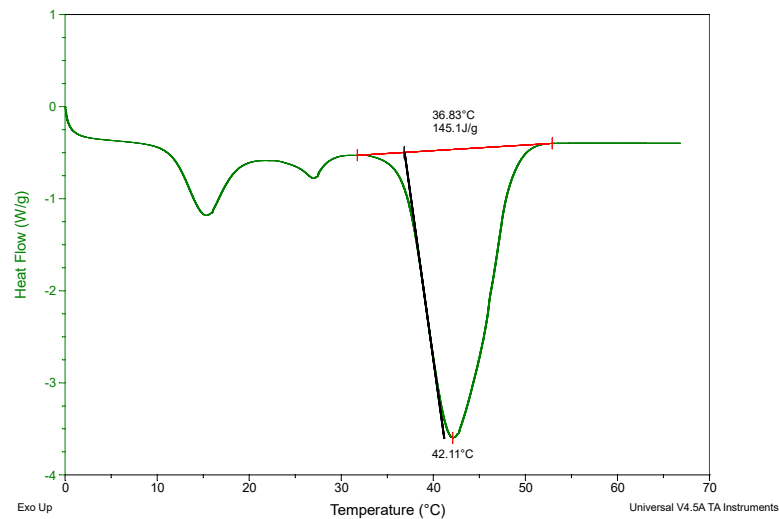
(b)

Figure 5.2-3: DSC curve for (a) RT31 and (b) RT42 Phase Change Materials.

a main peak at 31 °C, whereas the RT42 PCM is stated as a having a melt range of 38 °C to 43 °C with a main peak at 42 °C.

Conducted using a TA Instruments Q2000 Differential Scanning Calorimeter (DSC), Figure 5.2-3 shows the heat absorption of both of the PCM samples. The RT42 variation has a transition onset temperature of 36.83 °C and a peak transition temperature of 42.11 °C, whereas the RT31 sample has a transition onset temperature of 24.92 °C and a peak transition temperature of 32.32 °C.

The RT31 variation is better suited for the application, as the onset transition temperature is close to the discharge start temperature and the transition peak temperature is below the expected end temperature of the 1.5 C discharge, allowing the PCM's full capacity to be utilised. When examining the RT42

variant, the transition peak temperature is marginally higher than the expected final temperature of the battery, resulting in uncertainty whether the PCM will fully transition during a discharge, thus the RT31 PCM is used in the experimentation.

5.2.3 Foam Selection

The foam substrate employed in this study is made of Polyurethane (PU), which has a relatively low thermal conductivity (0.29 W/m·K), especially when compared to other polymers such as low density polyethylene (0.33 W/m.K), hight density polyethylene (0.45 – 0.54 W/m.K), [113, 114]. Furthermore, the PCM selected has a thermal conductivity of 0.2 W/m.K, therefore the similarities in thermal conductivity will contribute to a better understanding of the effect of the copper deposition layer and its purpose of enhancing heat transfer.

5.2.4 Electroless Plating for Polymer Substrates

As the PU substrate, in its raw form, is non-conductive, it is not possible to electroplate, it must be electroless plated to achieve a thin layer of copper over the surface. The principle of electroless copper deposition is to use the chemical reaction between a reducing agent and a copper salt in a liquid solution so that the copper ion can be reduced to a copper atom, the reaction should be continuous so that sufficient copper can form a film and cover the substrate [115].

The methodology used for electroless copper plating is combined from various sources [115-117]. Since formaldehyde is carcinogenic, glyoxylic acid-based solutions are commonly utilised instead of formaldehyde-based solutions.

Wang et al. (2011) created an electromagnetic interference shield using electroless copper deposition on Fraxinus mandshurica veneers (plywood), which served as the starting point for the plating bath used in this investigation [116]. Wang et al. employed chitosan to build a layer on which a thin palladium coating was formed, followed by copper deposition. Chitosan is not employed in this work since it is a viscous solution that does not fully penetrate the pores of the PU foam; nevertheless, a 2 g/L sodium hypophosphite solution is used to generate a thin layer of palladium for copper deposition.

The chemical concentrations utilised in the plating bath in the study for copper deposition are the same quantities used in [116], detailed in **Table 7**. It is critical to observe the presence of 2-mercaptobenzothiozole (2MBT) in the plating bath. As copper plating baths are notoriously unstable and prone to decomposition, this is added to the solution as a stabiliser [117].

Table 7: Electroless Cu Bath Composition

Chemical	Concentration (g/L)
$CuSO_4 \bullet 5H_2O$	20
$EDTANa_2 \bullet 2H_2O$	40
Glyoxylic Acid (50% wt)	21
2MBT	0.002

Bath Temperature = 55 °C, pH 12-12.5

F. Hanna et.al., investigates the use of different stabilisers in copper plating baths [117]. It is found that all stabilisers considered significantly increase the lifespan of the plating baths, and 2MBT at an optimum concentration of 2mg/L increases the deposition rate. It is stated that the EDTA-based bath with 2mg/L 2MBT can operate for 80 minutes before decomposing [117].

5.2.4.1 Substrate Preparation

The samples for electroless copper plating are prepared as follows;

1) Cleaning and conditioning – 5% wt Sodium Hydroxide solution is used at 60 °C for 10 minutes to ensure the substrate is clean from any contaminants.

2) Rinse – The substrate is then rinsed in deionised water at room temperature for one minute.

3) Etching – 30% wt Potassium Hydroxide at 60 °C is used to roughen the PU surface for the adhesion of the deposition. The substrate is immersed for four minutes.

4) Rinse – The substrate is then rinsed in deionised water for one minute.

5) Catalysing – the palladium-tin colloidal solution is used to catalyse the substrate for plating, at 60 °C for ten minutes. This solution is made from PHP A salt and PHP B solution.

6) Pd(0) Promotion – 2 g/L concentration sodium hypophosphite is used to promote Pd(0) on the substrate surface.

At this point, the samples are dried with hot air and weighed to obtain the pre-plating mass. The preparation of the samples removes small quantities of PU from the surface, thus altering the mass. The substrate is then ready to be placed in the plating solution for the desired time to achieve the desired plating mass

The catalyst solution (UNIPHASE PHP) supplied by Schloetter consists of UNIPHASE PHP A salts and UNIPHASE PHP B solution. The solution is made as follows.

Conducted in a fume cupboard, a clean one litre beaker is filled with half way with deionized water, in which 100 g of PHP A salt was dissolved. Then 20 ml of 37% hydrochloric acid was added and mixed well prior to addition of 20 ml UNIPHASE PHP B. The volume is then made up to 1 litre with deionized water. The solution is kept in a Winchester bottle to avoid chemical degradation due to UV light. Deterioration of the catalyst is visible when the dark brown colour weakens and the solution becomes slightly transparent, thus a new fresh solution needs to be prepared. Generally if stored in a cool dark environment the solution keeps for around 1 month and can be reused if no degradation is present.

5.2.4.2 Electroless Bath Preparation

A one-litre batch of a base solution is prepared in advance of substrate plating, the base solution is prepared in this way as a small quantity (0.2 mg/L) of 2-Mercaptobenzothiazole (2 MBT) is used as a stabiliser to prolong the life of the plating bath, one-litre quantity ensures accurate addition of the 2MBT. A RADWAG MYAS precision balance is used to measure out the small quantity. As copper electroless baths have a limited life, and can decompose once the reducing agent is added, the reducing agent is not added until 200 ml is removed from the base bath solution and plating is about to commence.

The copper bath is prepared following the procedure outlined in [115], the chemical quantities are per those detailed in [116] and 2 MBT is added as a stabiliser following the optimum concentration outlined in [117].

The procedure is as follows;

1) Add 2 MBT to 1 litre of deionized water.

2) Mix EDTA into the solution, EDTA is very hard to dissolve in water, so white precipitates of EDTA will remain in the deionised water.

3) Continuously add potassium hydroxide (KOH) to the solution; stir until the white precipitates disappear. The solution is now a dipotassium-EDTA solution. By using potassium hydroxide in glyoxylic acid solution, the Cannizzaro reaction rate is reduced, and the mechanical properties are improved.

   The Cannizzaro reaction involved in electroless copper plating using glyoxylic acid as a reducing agent consumes additional hydroxyl and glyoxylic acid.

4) Carefully add copper sulphate pentahydrate crystals into the solution in several separate goes.

5) Add potassium hydroxide until the white precipitates disappear.

The base solution does not contain the glyoxylic acid-reducing agent so can be stored in a cool dark place until required.

5.2.4.3 Electroless Cu Deposition Method

The Cu deposition is conducted with around 200 ml of the plating solution base, in which 4.2 g of glyoxylic acid is added and mechanically stirred until the
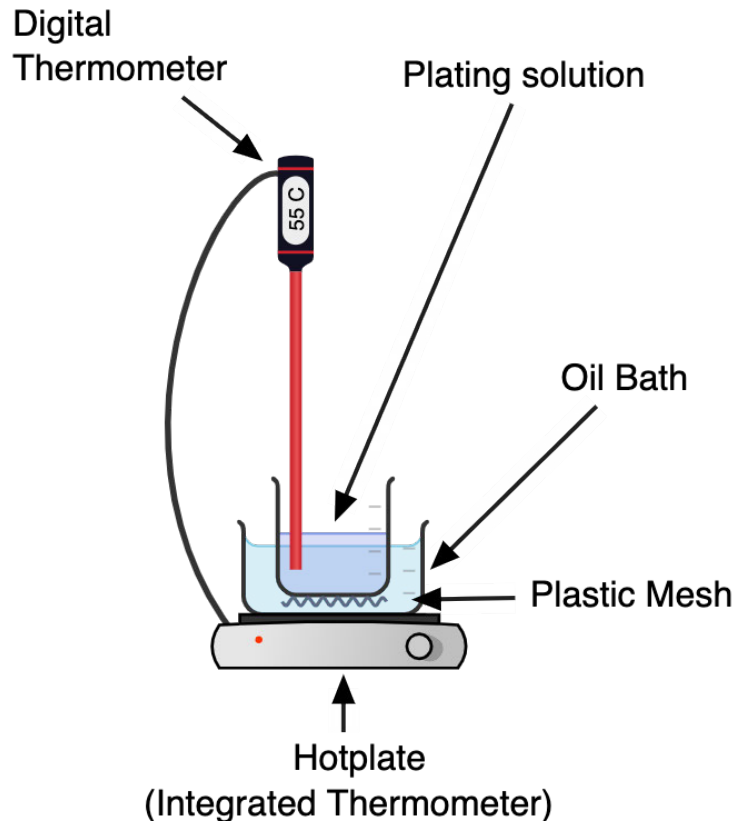
Figure 5.2-4: Plating Solution Setup

solution is at 55 °C, and potassium hydroxide is added until the solution reaches between pH 12 and pH 12.5, checked with a Fisher Scientific Accumet AE150 pH meter. The timing of adding glyoxylic acid is not critical, but the final pH values of the plating solutions must be controlled with potassium hydroxide.

Figure 5.2-4 depicts the setup for the plating process, in which the polymer substrates are inserted. To provide uniformity in heating the solution, the beaker of the plating bath is placed into an oil bath (Heidolph MR Hei-Standard, with Heidolph 504, 1 Litre oil bath attachment), the beaker rests on a plastic mesh, separating the bottom from the heating element. A digital thermometer is placed into the plating solution, the thermometer controls the heating of the oil bath to maintain a solution temperature of 55 °C. This process is like that deployed by W. Sha et. al. for their investigation of copper and nickel-phosphorus plating [115].

With the addition of 2MBT to stabilise the plating solution, foam substrates are electroless plated for 20 minutes, 40 minutes and 80 minutes. It is detailed by F. Hanna et.al. that the addition of 2MBT can provide up to 80 minutes of stability once the reducing agent is added to the plating bath [117].

It was found that this was the case and foam substrates were plated for this duration, it is important to note however that the plating rate dropped throughout the 40-minute and 80-minute plating sessions. This was observed due to the visible reduction of hydrogen bubbles in the solution. Once the samples were weighed after the plating sessions it was found that there is an increase in copper mass between the different durations, as shown in Table 9 for 10 PPI and **Table 9** for 20PPI.

Table 9: 10 PPI Foam Electroplating Results.

Plating Time (minutes)	Prepared Mass	Copper Mass
20	0.563	0.379
40	0.544	0.483
80	0.524	0.616

All mass values are in grams.

Table 9: 20 PPI Foam Electroplating Results.

Plating Time (minutes)	Prepared Mass	Copper Mass
20	0.563	0.438
40	0.491	0.482
80	0.526	0.610

All mass values are in grams.

5.2.4.4 Electro Plating

The method of copper electroplating is straightforward, as shown in Figure 5.2-5, an electrically conductive specimen is submerged into an electrolyte bath, and a current is applied, resulting in the migration of copper ions which will deposit onto the pre-existing metal layer of the submerged specimen [118].

The electrolyte bath used in this study contains two primary inorganic components; Copper sulfate ($CuSO_4$) which provides a source of copper ions, and sulfuric acid (H_2SO_4) which makes the bath conductive and acts as a charge carrier.

The method of electroless copper plating for this work was conducted using 1A current at 4V, where both faces of the foam structure were held in place for 10 minutes, resulting in 20 minutes of total plaiting.
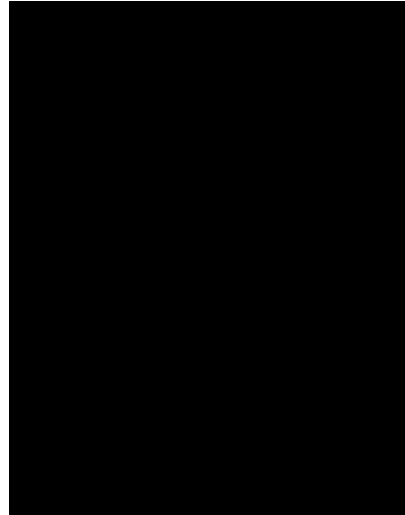
Figure 5.2-5: Electroless copper plating method [118]

5.2.5 Cu Foam Composite Manufacture

A series of foam samples are impregnated with the chosen PCM, RT31, to create foam composites to increase thermal storage within the PCM. These are three types, solid copper foam (Cu-S), Polyurethane foam (PU) and electroless copper-plated foam (Cu-P). The Cu-P samples are plated in the aforementioned process for twenty minutes achieving a copper mass of 0.342 g and 0.400 g, for 10PPI and 20PPI foams respectively, examples are shown in Figure 5.2-7.

The foam samples are impregnated with RT31 PCM under vacuum, where the samples are placed in a glass Petrie dish, melted PCM is poured into the dish to cover the foam, and the dish is then placed into the vacuum chamber (Figure 5.2-9 (a)) until the PCM solidifies. The dish is then placed into the Binder FD23

(a)

(b)
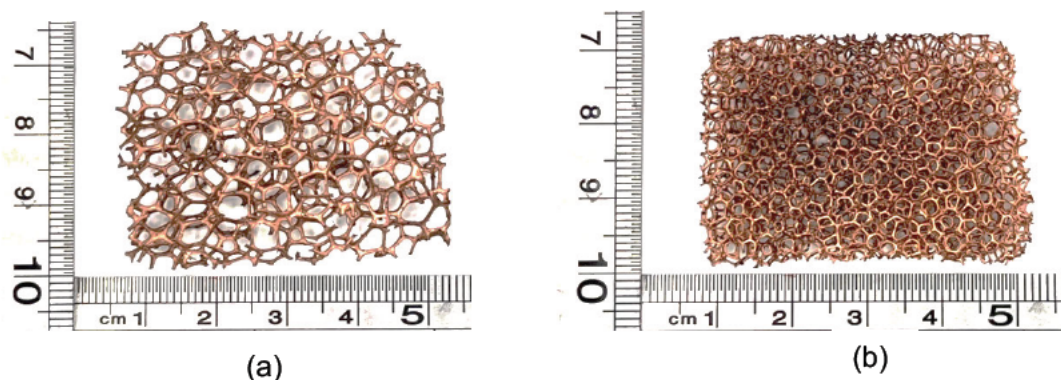
Figure 5.2-7 Example of 20 minute electroless plated PU foam (a), 10 PPI and , (b) 20 PPI.

(a)

(b)
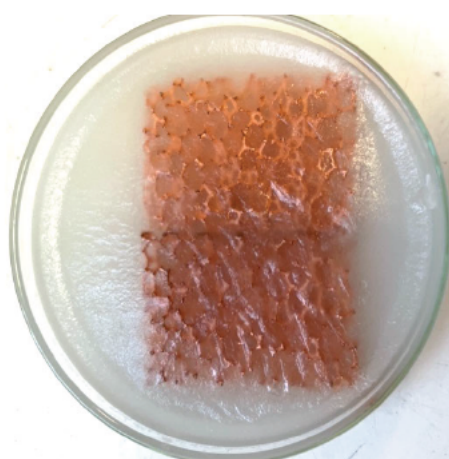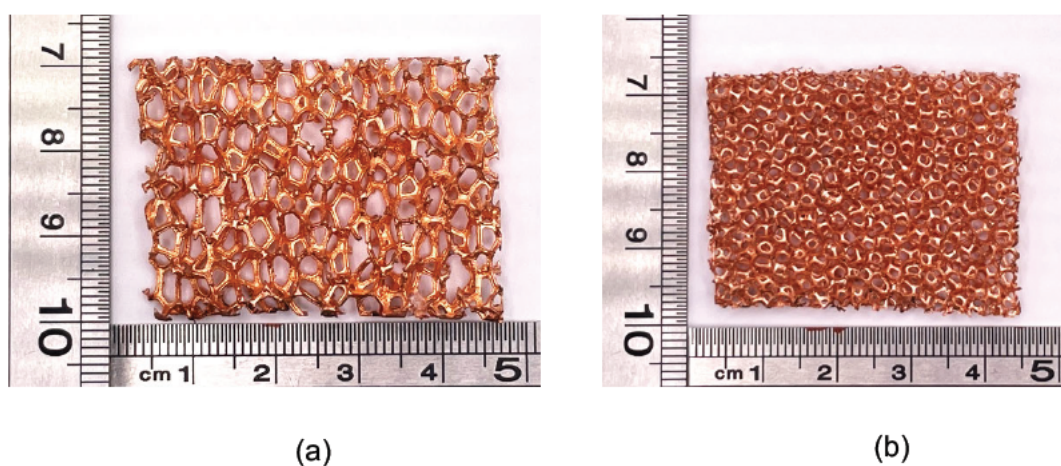
(c)

Figure 5.2-7: Solid Foam Samples, 10 PPI Cu-S (a), 20 PPI Cu-S (b), and (c), foam sample impregnated with RT31 PCM after three times heat and vaccum cycle.

oven (Figure 5.2-9 (b)) at 45 °C until fully melted (approximately 30 minutes). The dish is then placed back into the vacuum chamber, the cycle is repeated a total of 3 times. When the chamber achieves a consistent vacuum, the air exiting the foam is seen as visible bubbles on the surface; this is replaced by the PCM permeating the foam structure.

Once the PCM foam composites are manufactured, they are placed into a 3D-printed case. The case is manufactured out of polylactic acid (PLA) using a Prusa Research Mini Plus, with 100% infill to ensure the case is solid and will not allow PCM to pass through the PLA layers when liquid. The case is designed for the 5 mm and 10mm thickness of PCM across the entire face of the LIB cell on both sides. The impregnated PCM foam composites are installed into the case void between the cell surface and the case wall. Additional RT31 PCM is added to fill around the cell and PCM foam composites. The case is intentionally designed taller than required to provide room for PCM expansion as there is a 12.5% volume expansion coefficient.

| (a) | (b) |
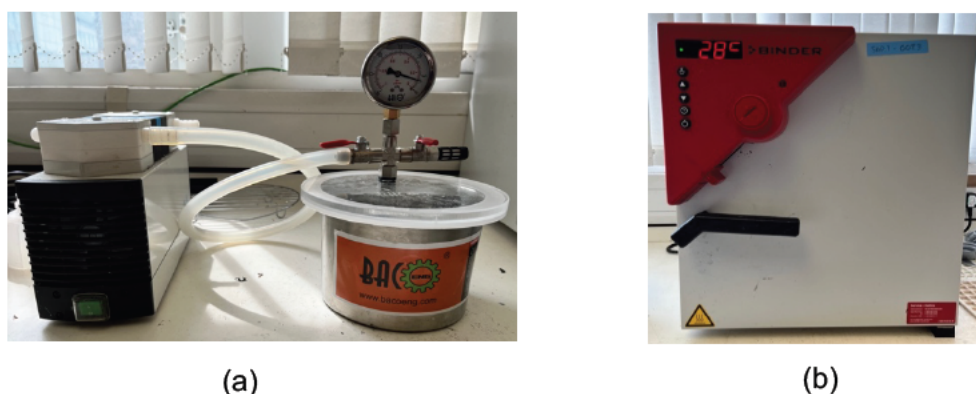
Figure 5.2-9: Equipment used for foam impregnation with PCM, (a) baco vaccum chamber and, (b), Binder FD23 forced convection drying oven.

| (a) | (b) | (c) |
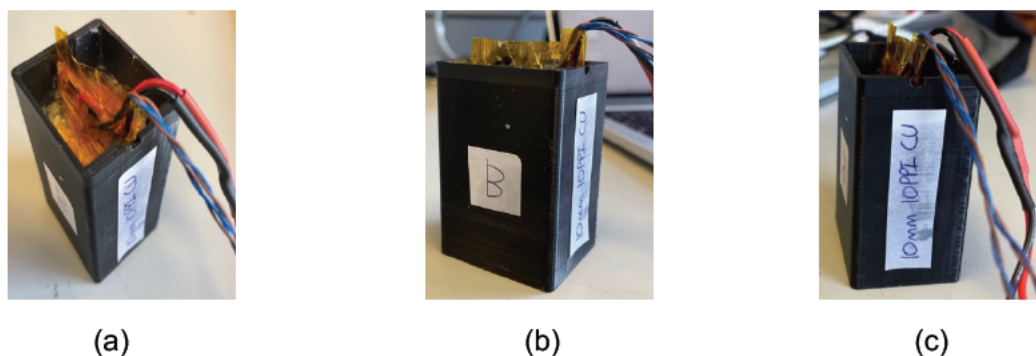
Figure 5.2-9: Configuration for battery testing, PLA 3D priinted box containing the battery cell, PCM and PCM foam composites, (a) top view where the surface of PCM is visible, (b) side view showing height of the box with labels to identify battery side and , (c), front view showing label to identify sample contents.

Table 10: *Foam Composites Configuration Details*

Sample	Copper Mass (g)	Impregnated Mass (g)	PCM Mass (g)	Total Mass (g)
5mm PCM	-	-	15.16	65.56
10mm PCM	-	-	26.53	81.83
10PPI PU	-	20.06	25.49	83.10
20PPI PU	-	21.85	26.63	83.71
10PPI - Cu-S	17.40	37.30	26.49	99.78
20PPI Cu-S	12.70	30.40	26.62	95.62
20 Min-10PPI Cu-P	0.379	24.40	26.87	83.73
20 Min-20PPI Cu-P	0.435	19.96	26.16	84.08
40 Min-10PPI Cu-P	0.483	24.42	26.45	84.30
40 Min-20PPI Cu-P	0.482	20.85	26.73	83.46
80 Min-10PPI Cu-P	0.616	24.58	26.91	84.35
80 Min-20PPI Cu-P	0.610	21.01	25.80	83.36
10PPI Cu-EP	1.531	24.15	26.49	84.78
20PPI Cu-EP	1.512	21.30	26.38	84.60

PPI = Pores Per Inch, PU = Polyurethane, S = Solid, P = Electroless Plated, EP = Electroplated. Total mass includes case, battery, TCs, PCM and Foam where appropriate.

Figure 5.2-9 shows a fully constructed configuration from various sides, **Table 10** details all configurations analysed in this chapter. It is important to note that the total mass of PCM is around 26g, except for 10PPI-PU which is 0.51g under 26g due to an error while manufacturing the configurations. It is also important to highlight that the Cu-P configuration copper mass is 97.82 % and 96.62% reduced for 10PPI Cu-P and 20PPI Cu-P respectively when compared to the Cu-S configurations. A single cell is discharged without any PCM or PCM foam composites, this will act as a control to distinguish the effectiveness of the configuration outlined in **Table 10**.

5.2.5.1 Scanning Electron Microscope Imaging

A Hitachi S-4800 Scanning Electron Microscope (SEM) was used to analyse the electroless plating surface of the foam. The SEM shows a detailed image of the surface of the foam, to the point where the copper grains are visible, thus showing that all plating times provides a full covering of copper on the polyurethane skeleton.

Firstly, the surface of the plain polyurethane foam is inspected. The use of palladium sputter coating was deployed to make the surface conductive for the SEM. Figure 5.2-10 shows a whole pore and the triangular strut profile of the 20PPI PU foam. In general, the foam surface is smooth with PU artefacts over the surface.

It is shown that the polymer foam is solid in its structure which is contradictory to the commercial copper foam. In Figure 5.2-11 it is shown for both the 10PPI

(a)   (b)
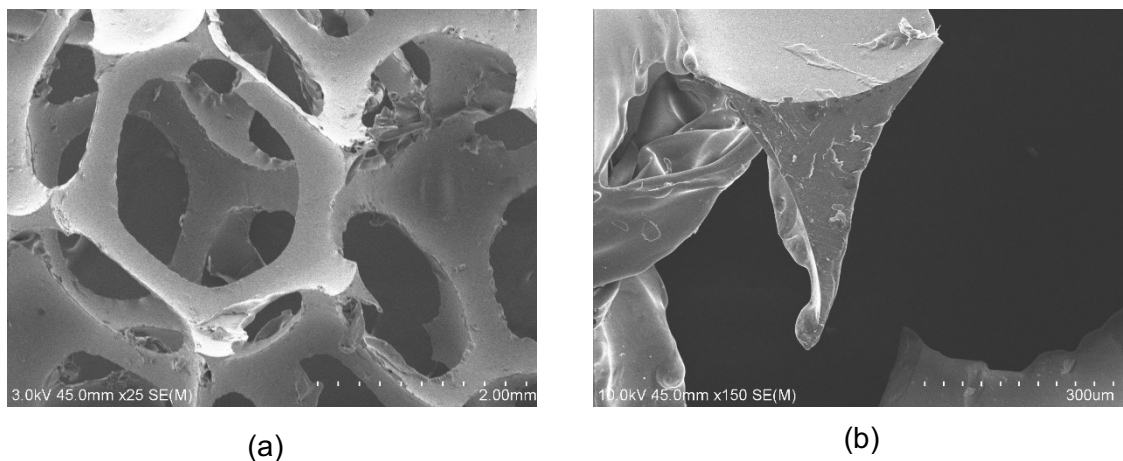
Figure 5.2-10: SEM Imaging of 20PPI PU Foam, (a) whole pore with struts, and (b) Strut cross section.
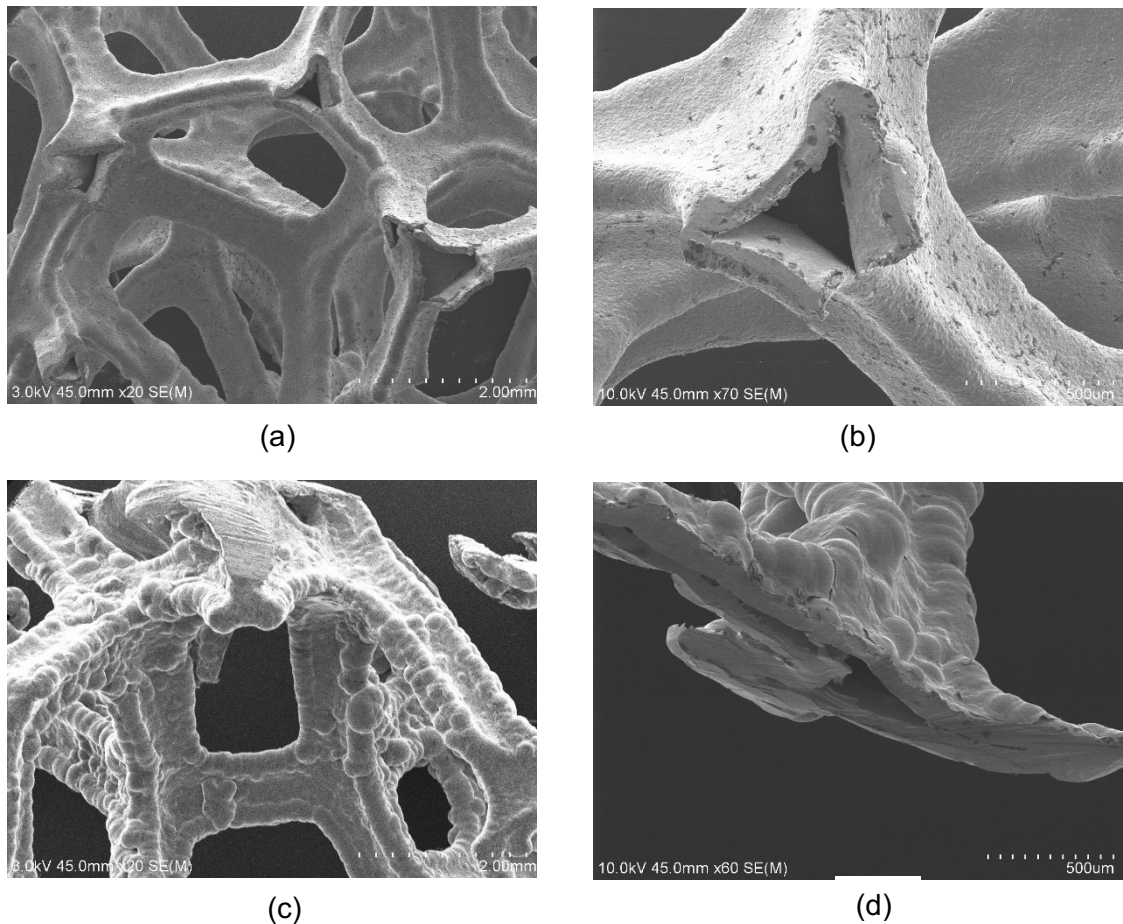
Figure 5.2-11: SEM imaging of commercial foam; (a) 20PPI pore structure, (b) 20PPI strut cross section, (c) 10PPI pore structure, and (d) 10PPI strut cross section.

and 20PPI that the copper structure is hollow. It is reasonable to assume that under vacuum the PCM will infiltrate the internal structure as the foam is cut to size, leaving open strut cross sections.

The electroless copper plating is presented in Figure 5.2-12 for each of the three plating times. It is generally seen that there are no major differences in the structure of the copper layer on the PU skeleton, additionally it appears that there is consistent layer over most of the pieces. However, it is seen for all three samples used for SEM analysis that there is cracking on the surface. It is not known if this is due to handling the sample or a result of the plating method. Generally, the plated surface looks consistent for each plating duration and overall, a consistent copper surface is present.
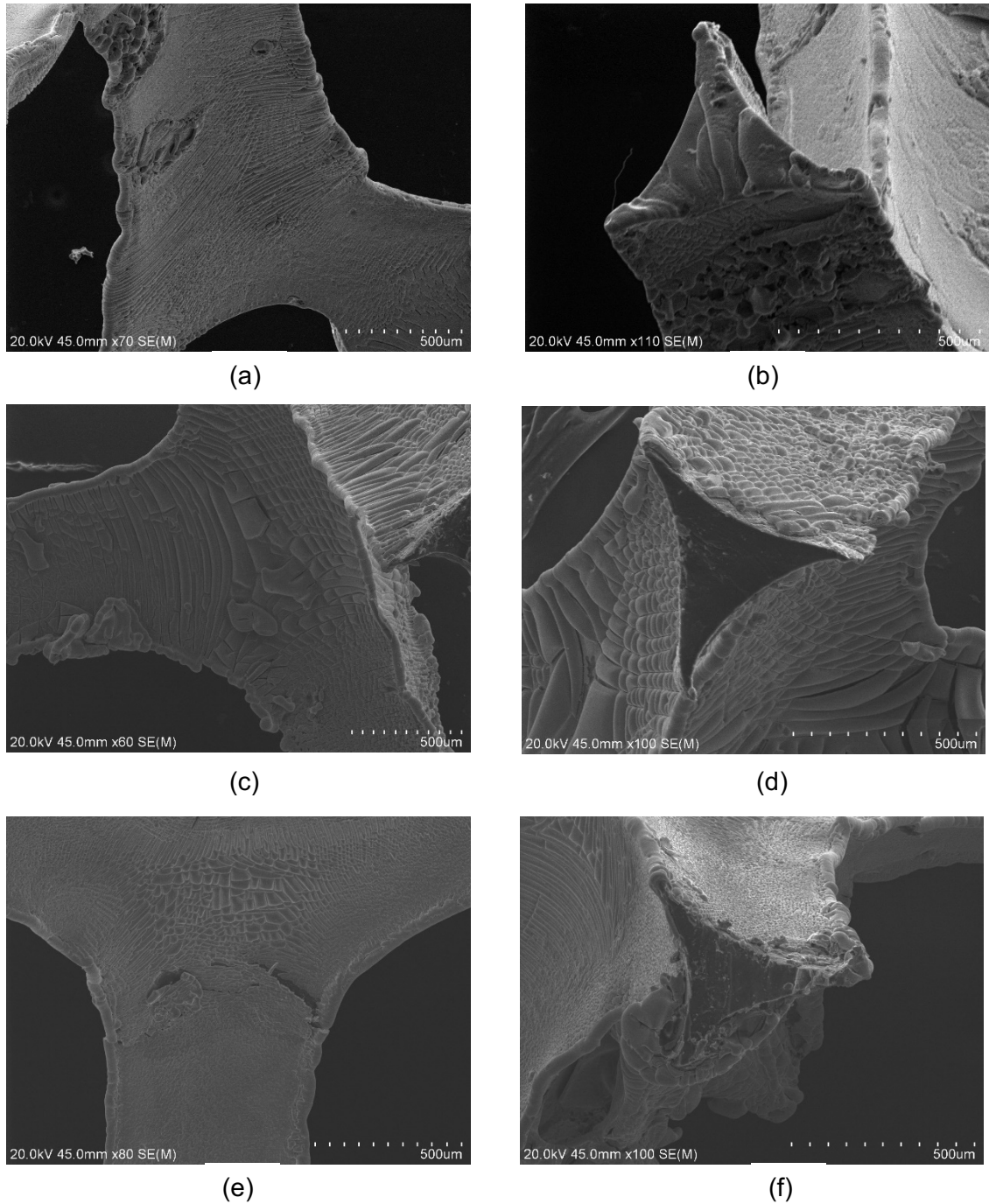
Figure 5.2-12: SEM imaging of electroless copper PU foam, (a) 20 minute plating surface, (b) 20 minute plating strut cross section, (c) 40 minute plaitng surface, (d) 40 minute plaitng strut cross section, (e) 80 minute plating surface, and (f) 80 minute plating strut cross section.

5.2.6 Thermal Conductivity of PCM Foam Composites

The Thermal conductivity is calculated for the Cu-S configurations by the method set out by X, Xiou et. al [83] who based their work partially on the work of Bhattacharya et. al. [119].

The bulk porosity (ration of solid mass to pore size) of the solid foams is calculated as follows.

$$\varepsilon_b = 1 - \frac{m_{fo}}{\rho_{sk} V_t} \tag{10}$$

where m_{fo} is the mass of the metal foam, V_t is the total volume of the metal foam piece, ρ_{sk} is the density of the skeleton material.

The impregnation ration α_i, which is a dimensionless parameter to evaluate the compatibility between the PCM and the metal foam structure, is calculated as follows;

$$\alpha_i = \frac{m_{actual}}{m_{ideal}} = \frac{\Delta m_i}{\varepsilon_b V_t \rho_{pcm}} \tag{11}$$

Where Δm_i is the difference in mass between the impregnated foam composite and the mass of the foam and ρ_{pcm} is the density of the PCM during the solid phase, in this case for RT31, 0.88 g/litre. It is calculated that the impregnation ratio for the Cu-S configurations is 0.81 for 20 PPI and 0.88 for 10 PPI foam variants.

The theoretical thermal conductivity can be calculated as follows.

$$\lambda_e = A_c \left(\varepsilon_b \lambda_{pcm} + (1 - \varepsilon_b) \lambda_{sk} \right) + \frac{1 - A}{\left(\dfrac{\varepsilon_b}{\lambda_{pcm}} + \dfrac{1 - \varepsilon_b}{\lambda_{sk}} \right)} \tag{12}$$

Where λ_{pcm} is the thermal conductivity of the PCM, in this case, 0.2 W/m.K for RT31, λ_{sk} is the thermal conductivity of the skeleton material, in this case, copper which is taken as 390 W/m.K, the same value used in [120], and A_c is the

correlation coefficient, found to be 0.35 by Bhattacharya et. al. [119] for foams of 5–40PPI and porosities 90.5–97.8%, which these metal foams fall within.

It is found that the theoretical thermal conductivities are 10.28 W/m.K and 7.55 W/m.K for 10PPI Cu-S and 20PPI Cu-S respectively, this compares well to the findings in [120].

As shown in **Error! Reference source not found.**, the thermal conductivity of the skeleton material (λ_{sk}) is required to calculate the theoretical thermal conductivity of the foam composite. With a copper-plated PU substrate, it is not accurate to use the conductivity of the PU or the conductivity of pure copper for this value and a combination of the two materials adds complexity beyond the scope of this work as a proof-of-concept investigation, thus the thermal conductivity is not calculated for all configurations, the performance of the configurations is compared using heat change recorded at the battery cell surface.

It is important to note that it is possible to experimentally obtain the thermal conductivity of foam composite samples using the hotdisk method.

The well-established Hot Disk method, or Transient Plane Source (TPS) method invented by Hot Disk founder Dr Silas E. Gustafsson in 1986, allows rapid, accurate and non-destructive testing of thermal conductivity, thermal diffusivity and specific heat capacity of most material types, all in a single measurement. A key aspect of the TPS method is that it is absolute i.e., there is no need for repeated calibrations or the use of standard samples, as is common with other approaches. The TPS method requires one or two pieces of the sample to test, each needing no more than one flat surface where the Hot Disk double spiral sensor can be applied [121].

Many peer-reviewed papers explaining and evaluating the technique have been published in scientific journals. Since 2008 the method is standardised in ISO 22007-2, and over the years thousands of publications featuring results acquired with Hot Disk instruments have been published [121].

Unfortunately, the university does not own this equipment, The University of Edinburgh was contacted by a member of the technician staff to enquire if there was a system available for use, unfortunately, the contact at the University of Edinburgh was not aware of the required apparatus at the institution.

5.2.7 Experiment Setup

All of the configurations detailed in **Table 10** are subject to 1.5 C discharge via the B&K Precision electronic load. The cell is charged with the B&K precision power supply at 1 C until the cut-off current of 0.36 mA is achieved. During all testing, the sample under test is rested in the chamber at a 25 °C constant temperature until all sensors indicates a uniform temperature as close to 25 °C as possible, generally around 60 to 90 minutes, ensuring thermal equilibrium. After charge and discharge, the samples under test are rested for at least 30 minutes for chemical equilibrium to occur within the battery cells.
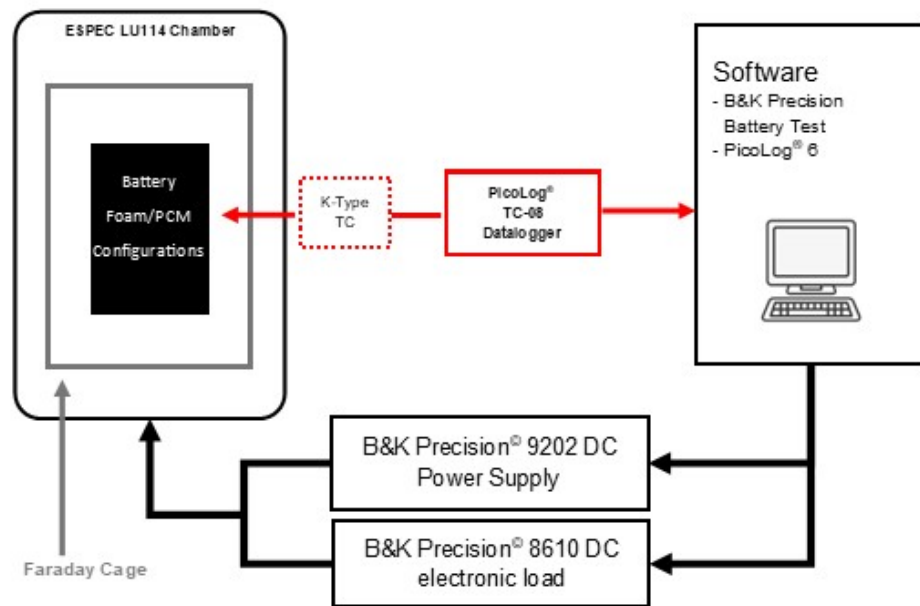
Figure 5.2-13: Testing Regime Setup for PCM and PCM Foam composites.

The experimental setup is shown in Figure 5.2-13, which is similar to the previous setup, where the ESPEC LU114 chamber is used to maintain a constant ambient temperature, and the Pico Technology TC-08 and the Picolog software are used to acquire the thermocouple temperature response. The samples under test are held in a Faraday cage inside the ESPEC chamber to eliminate any noise or interference.

5.3 Results

The results and discussion will initially discuss only the 20-minute plating configurations, named Cu-P in the graphs in section 5.3.1, thus any reference to plating in this section refers to only 20 minutes electroless plating. Then all configurations detailed in **Table 10** are discussed in section 5.3.2 onwards.

5.3.1 Initial Copper Deposition Analysis

The following section details and discusses the results of the testing regime set out previously in this chapter. Firstly, it is important to consider starting temperature when discussing temperature change. All tests must be started within a reasonable range to ensure conformity in the results. Figure 5.3-1 (a) shows that the average start temperature for discharge tests is relatively linear, around 24.75 °C. Moreover, it is shown in Figure 5.3-1 (b) that the standard deviation for the start temperature is no more than 0.263 °C, with the majority below 0.15 °C. It is demonstrated that an effort was taken to ensure a relatively even starting temperature for the discharge tests to ensure comparability of the final results.
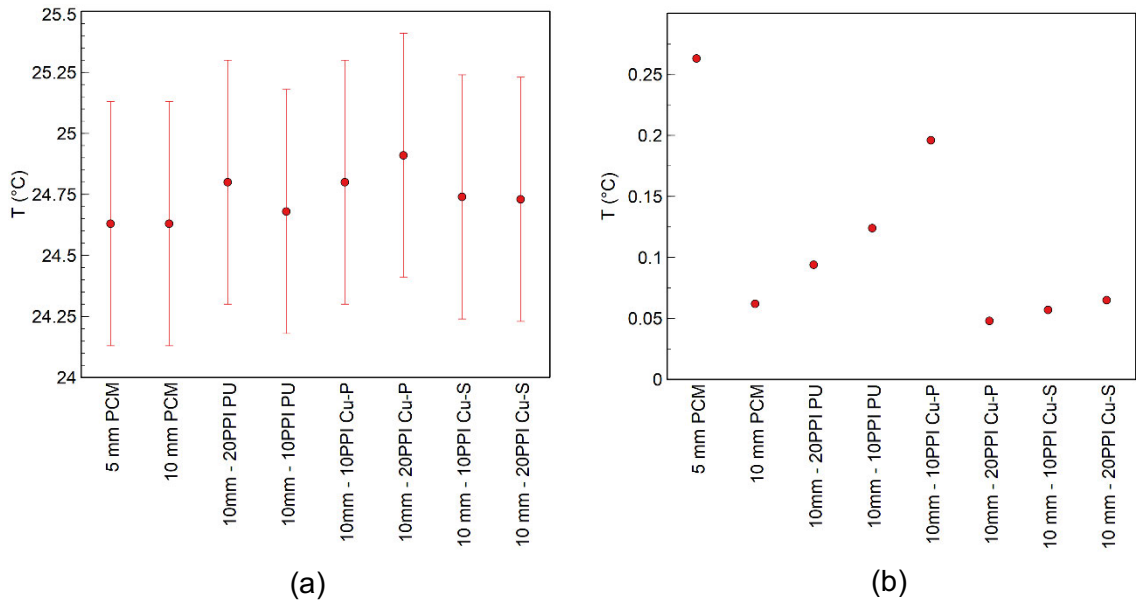
Figure 5.3-1: Testing start temperature, (a) an average of three tests showing 0.5 °C uncertainty for K-type thermocouples, and (b), standard deviaiton of three tests per sample.

All of the samples with PCM and PCM/foam composites are initially directly compared to the discharge of a LIB cell with no passive cooling method applied, then a comparison of the samples alone, to fully investigate and discuss the comparability of the configurations.

Figure 5.3-3 shows the average temperature change for the discharge tests of all considered configurations. It is shown that as soon as PCM is incorporated into the case there is a dramatic reduction in final temperature at the battery cell surface. It is shown that for 5 mm PCM thickness, a reduction of 8.54 °C, equates to a 49.39% reduced temperature change in the cell, however, the doubling of the PCM only adds a further 2.35% reduction to 51.42%, which can be seen for the 10mm PCM configuration. It is demonstrated that simply
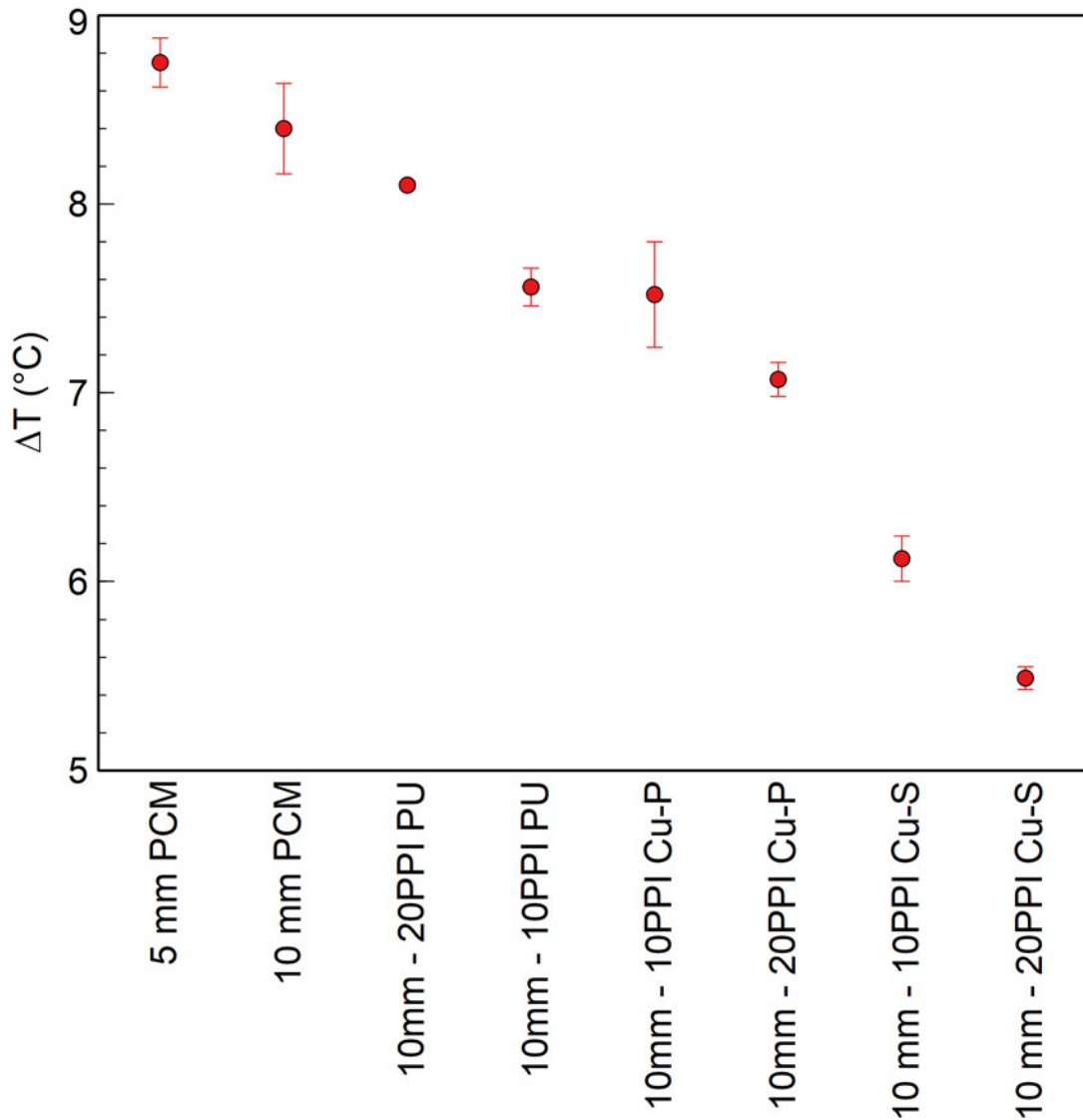
Figure 5.3-2: Final battery temperature change, average of three dischaege tests, showing standard deviaiton.

doubling the PCM thickness does not result in the doubling of thermal storage, this is due to the low thermal conductivity of the PCM as discussed previously it is shown that the 10mm PCM thickness with 20PPI solid copper (10mm 20PPI Cu-S), shows the most reduction in cell temperature with an additional 18.86% to achieve a total reduction of 68.28% when compared to the cell alone.

Figure 5.3-2 shows the incremental decrease over the configurations tested. In this case, the standard deviation is represented as error bars, to show the variation in the final results. It is shown that 5 mm PCM shows the highest temperature change, then incremental reductions to the best performing
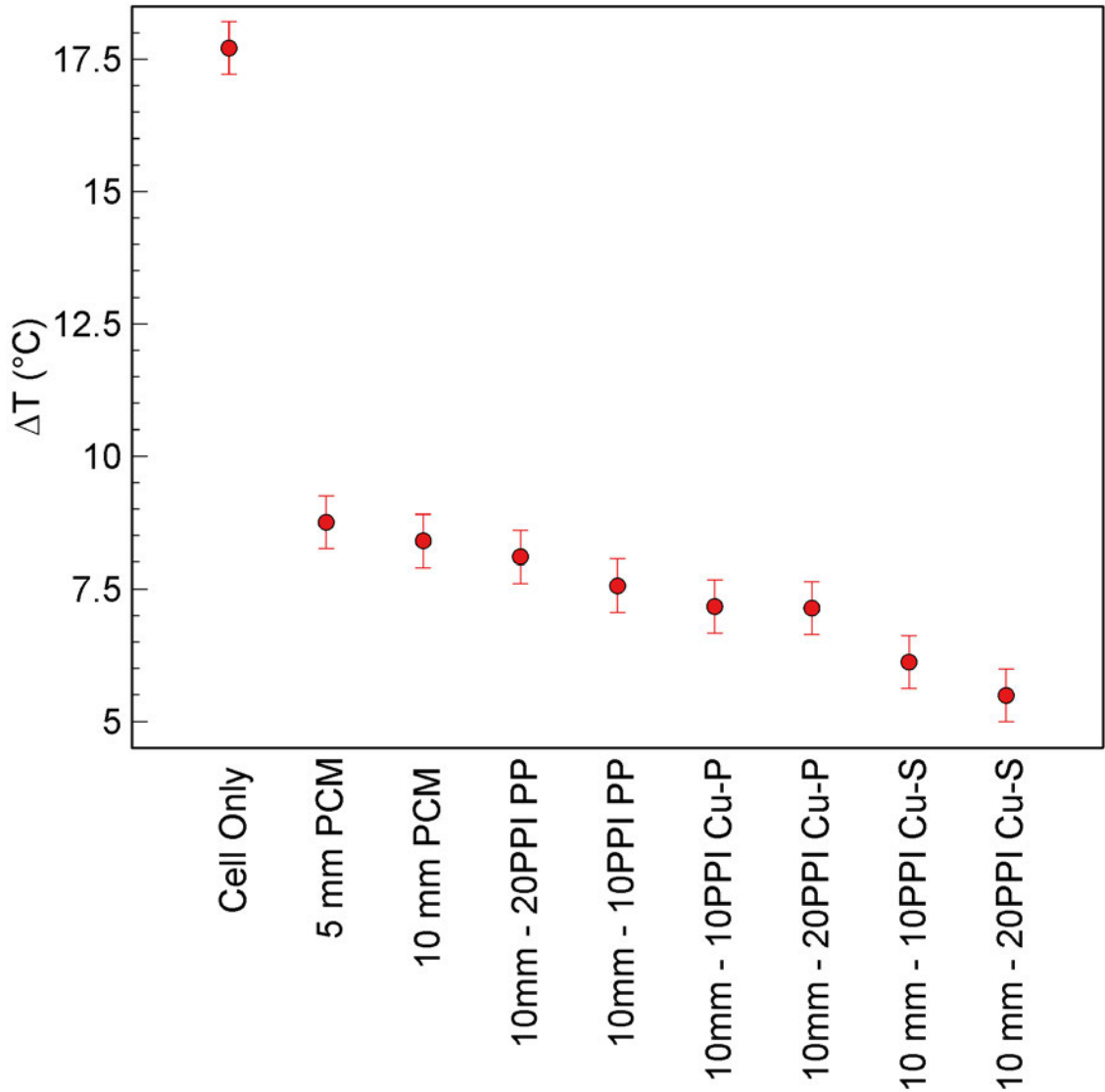
Figure 5.3-3: Temperature change of a LIB cell, PCM samples and PCM/Foam composites. showing 0.5 °C uncertainty for K-type thermocouples.

configuration, 10mm 20PPI Cu-S. It is shown that there is a 37.26% reduction in temperature change between the 5 mm PCM-only sample to the 10mm 20PPI Cu-S. The plated samples, 10mm 10PPI Cu-P and 10mm 20PPI Cu-P show a reduction of 14.06% and 19.20 % respectively. Between the two plated samples, it is shown that when considering the mean result, the 20PPI variant is 5.98% more effective at lowering the temperature gradient and 10mm 10PPI Cu-P shows a higher standard deviation. If the lower error for 10PPI Cu-P and higher

error for 20PPI Cu-P are considered, it is shows that there is only a 0.08 °C difference between the two configurations.

Figure 5.3-4 shows the plated and solid foam configurations together, shown is the reduction in maximum temperature change of 5.98% when the 20PPI foam is used. The density of foam also shows to be important as the solid foam demonstrates the same findings as the plated foam, however, the solid 20PPI foam shows 10.29% more effectiveness. It is also shown that there is a gap
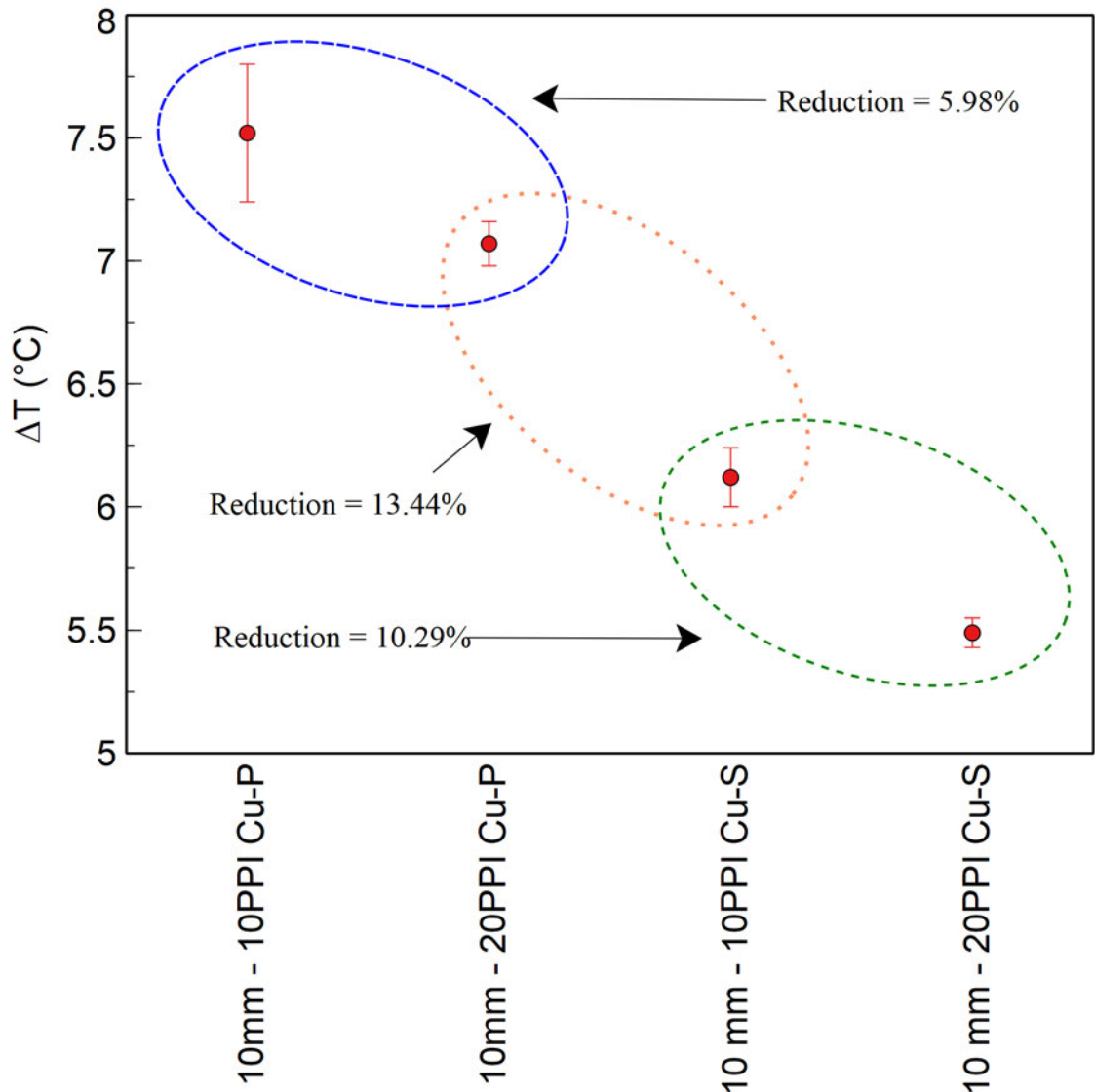
Figure 5.3-4: Plated and solid foam samples with 10 mm PCM, showinf percentage drop between both plated samples, solid samples and 20PPI plates against 10PPI Solid foam.

between the Cu-P and Cu-S configurations, averaging 13.44%.

Comparing the Cu-P to 10 mm PCM, it is shown in both the 10PPI and 20PPI configurations, there is a significant reduction in the temperature change (Figure 5.3-5 (a) and (b)), for the 10PPI Cu-P there is a 10,48% temperature

reduction and for 20PPI Cu-P, 15.83%. This shows that the addition of the thin layer of copper to the PU foam substrate aids the transfer of heat into the PCM, however, in comparison to the commercial solid copper foam there is still a significant gap. In the case of 10PPI Cu-P, 18.62%, and 20PPI, 22.35% when comparing the Cu-P to the Cu-S configurations.

(a)   (b)
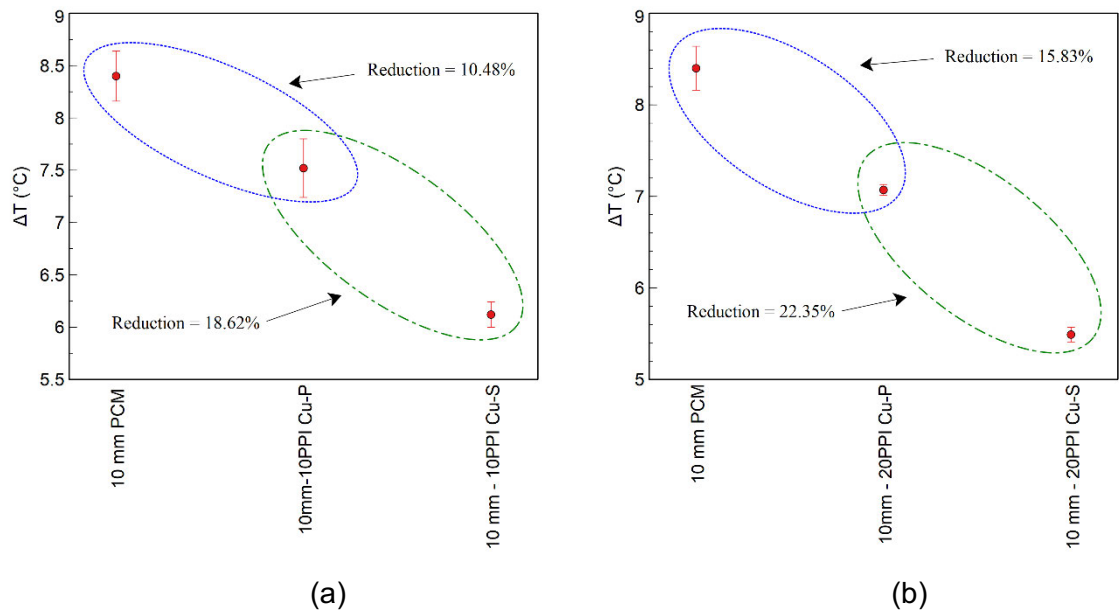
Figure 5.3-5: Temperature delta of discharge considersing (a) 10PPI configuraitons, and (b), 20PPI configurations.

5.3.2 Varied Copper Plating Mass

The following section details and discusses the results of the 1.5 C testing of the configurations with various foam plating masses, as detailed in **Table 10**. The start temperature of each test is discussed to ensure the comparability of the results. Figure 5.3-6 (a) shows the average start temperature of the three tests conducted on each configuration, showing 0.5 °C uncertainty. It is shown that they all begin between 24.5 °C and 25 °C, Figure 5.3-6 (b) shows the standard deviation of the three tests for each configuration, it is shown that the majority show less than 0.2 °C with nothing above 0.21 °C, showing that there is good consistency of the start temperature.

(a)

(b)
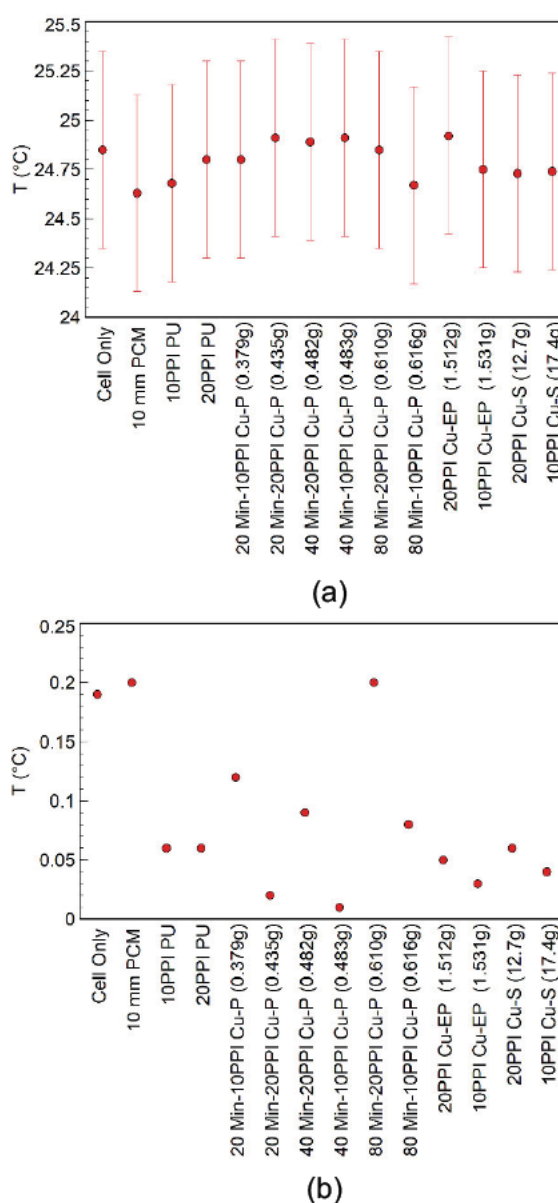
Figure 5.3-6: 1.5 C discharge test (a) Start temperature with 0.5 °C uncertainty as error bars, and (b), standard deviation of the three discharge tests for each configuration.

Figure 5.3-7 shows the average temperature change (ΔT) at the cell surface from the two attached thermocouples. It is shown, similarly to the previous section, that as soon as PCM is introduced, a significant drop is achieved, furthermore it's shown that there is a gradual drop as the copper mass of the foam increases, with some exceptions. The pore density of the foams will be discussed individually, then the foam densities will be compared to each other, and conclusions will be made regarding the effectiveness of the foams and the role in which the copper mass plays in the cooling effect of the battery cell.
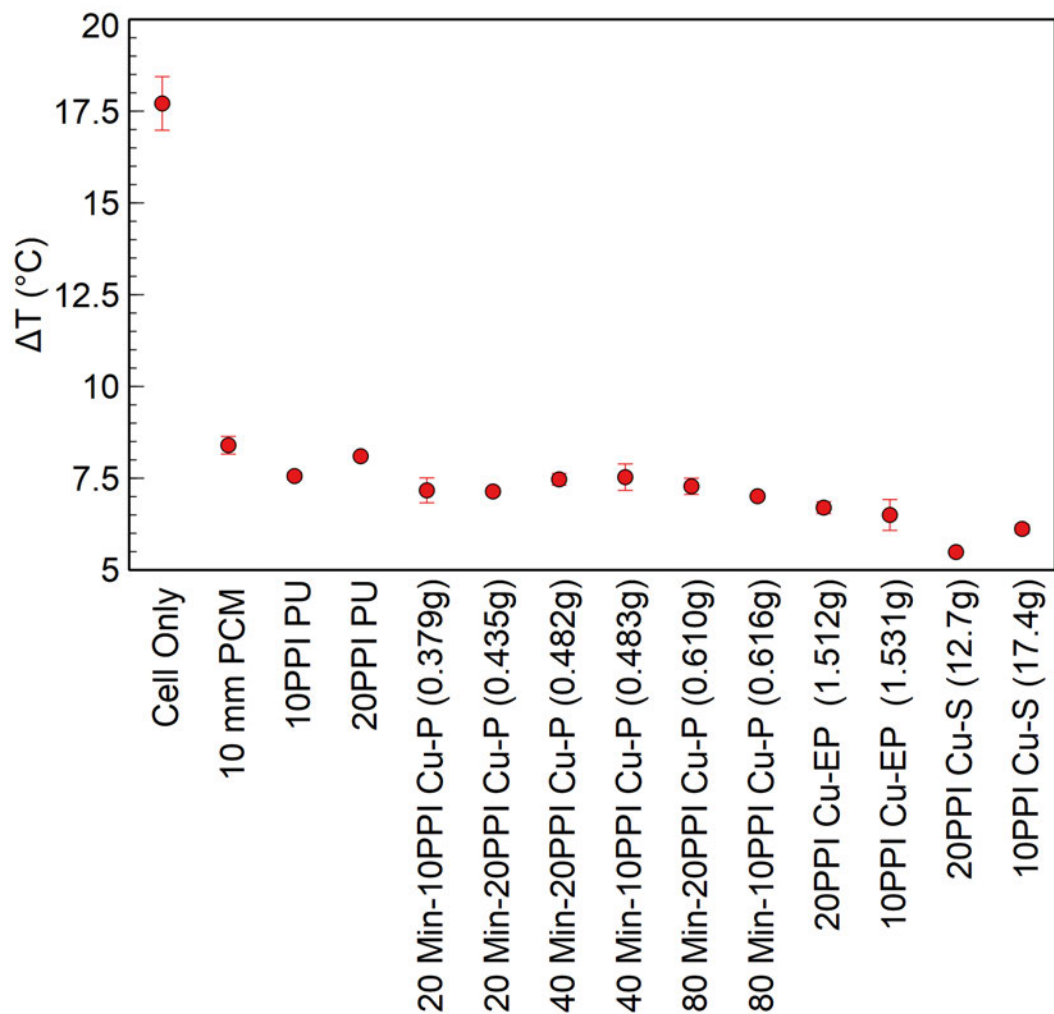
Figure 5.3-7: All configurations, temperature change at the cell surface.

5.3.2.1 10PPI Configurations

The 10PPI configurations are compared directly with each other to understand the effectiveness of the 10PPI foam with various plating mass. Figure 5.3-8 shows all 10PPI configurations against the 10mm PCM only configuration, it is found that as soon as any type of foam is added to the PCM a temperature reduction at the cell surface is seen, however, it is also evident that the plain PU foam performs very similarly to the 20 and 40 minute plating configurations with 0.379 and 0.483 grams of copper respectively, it is only in the 80 minutes plating with 0.616 grams of copper where a slight reduction is seen. It is important to note the larger standard deviation of the 20 and 40-minute plating configurations compared to the plain PU foam configuration, which suggests the foam is not aiding the heat transfer consistently. It is shown that the electroplated configuration, 10PPI Cu-EP is closely comparable to that of the 10PPI Cu-S configuration, all be it with a larger standard deviation.
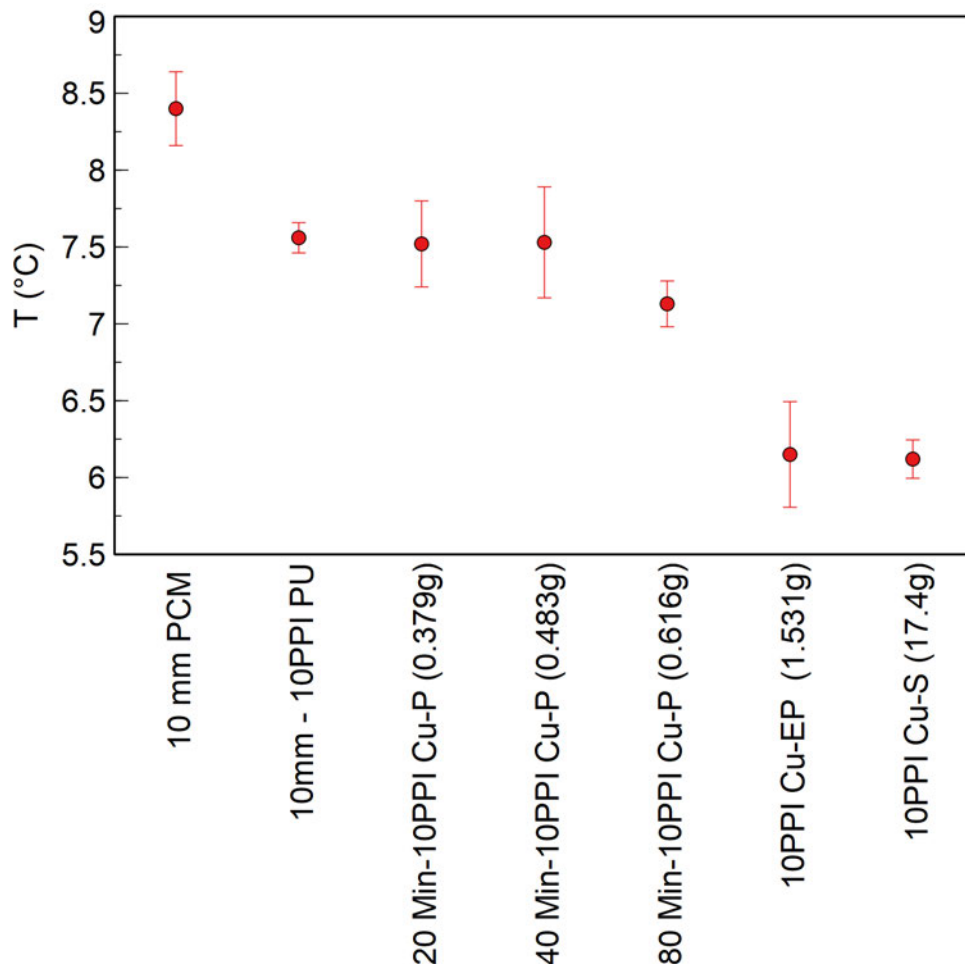
Figure 5.3-8: 10PPI Configurations with 10mm PCM only

Figure 5.3-9 further compares the plating configurations, showing an inconsistent reduction when looking at the electroless plated configurations. If the 0.5 °C were placed on the 20, 40, and 80-minute configurations it would show that there are effectively no distinguishable values over the three configurations. It can be proposed that in this case, the electroless plating shows to be as effective at 20 minutes as it is at 80 minutes, with 0.237 grams more copper on its structure. When the copper mass on the foam skeleton is increased, a difference is shown, this is the case for the Cu-EP configuration with an extra 0.915g of copper aided by electroless plating. It is shown that there is a 13.74% reduction in the average temperature change between the Cu-EP and the 80-minute electroless configurations. This is also significant as the Cu-EP configuration shows a small 0.33% variation from the Cu-S commercial foam, showing comparability with the commercial foam variant, with a larger standard deviation, however.
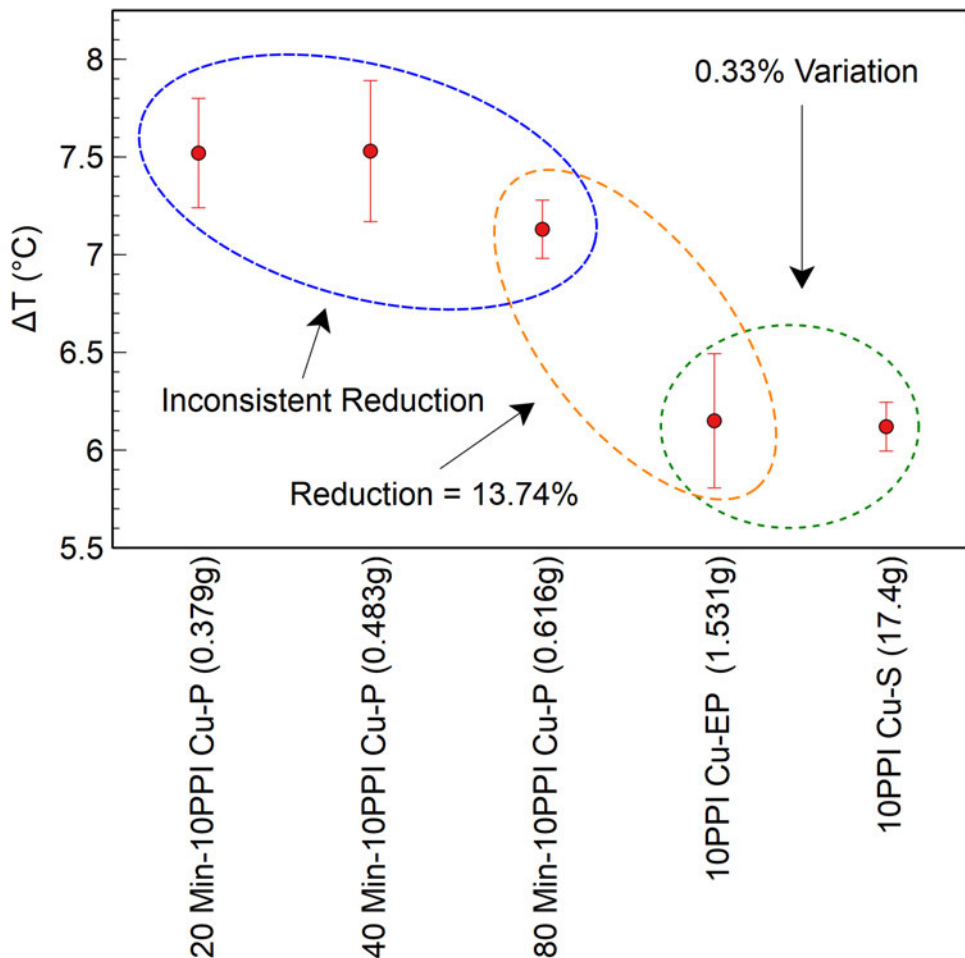
Figure 5.3-9: Temperature change of 10PPI Plated Samples

While the electroless plated configurations for the 10PPI foam density do not show significant change with increased plating time and Cu mass increase, it is shown that with the 80-minute acting as a base layer it is possible to achieve sufficient electroplating on the foam skeleton to directly compare with the commercial foam with over 91.47% more copper mass.

When comparing the best two configurations i.e., the 10PPI Cu-EP and 10PPI Cu-S configurations, to the cell only, it is shown that these configurations provide a substantial reduction of the cell surface temperature. It is calculated for the 10PPI Cu-EP configuration, there is a 63.23% decrease in the cells' average surface temperature, while the Cu-S Configuration only provides a further 2.21% achieving a temperature reduction of 65.44%.

5.3.2.2 20PPI Configurations

The 20PPI configurations show different results from the three discharges per configuration. As shown in Figure 5.3-10, there is still a drop in the temperature
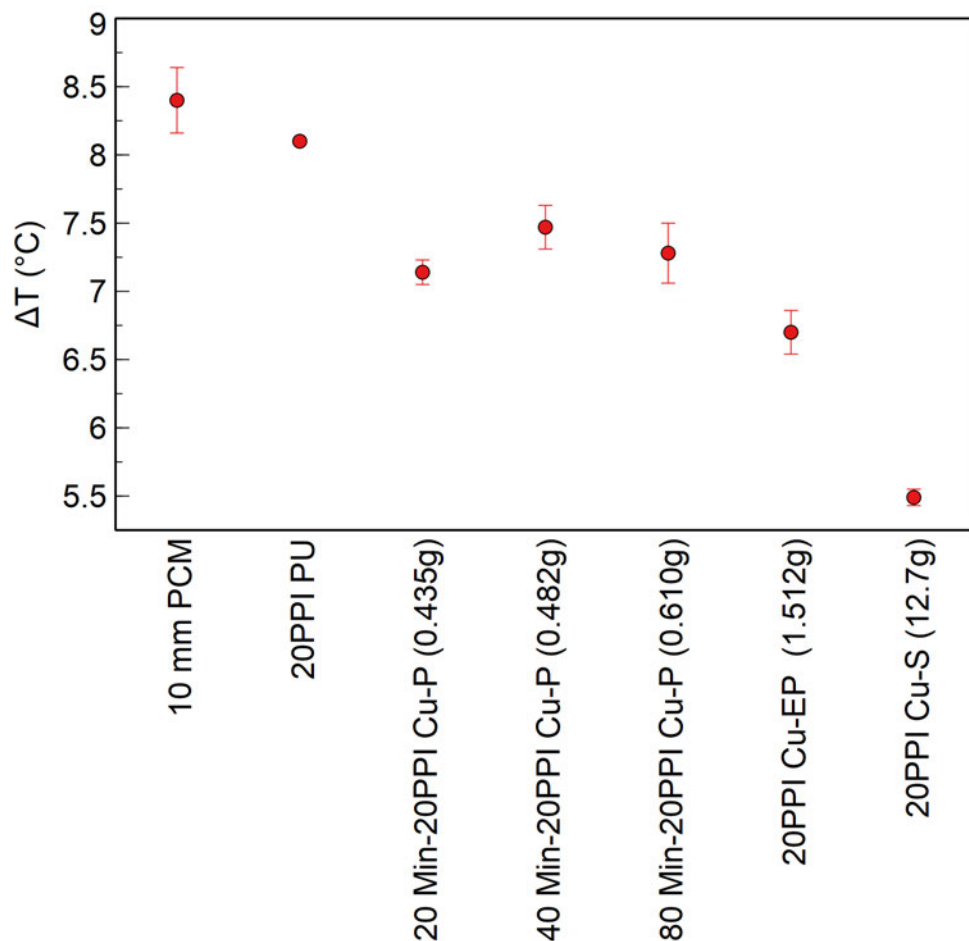
Figure 5.3-10: 20PPI Configurations with 10 mm PCM configuraiton

change as soon as foam is added into the PCM, as seen with the 10PPI configurations, however, the plain PU foam in the 20PPi density shows to be higher than that seen in the 10PPI configuration, with a very small standard deviation not visible in Figure 5.3-10. It is shown that the electroless plated configurations show a similar trend to the 10PPI configurations where there is no consistent change between the 20, 40 and 80-minute plating configurations. When the electroplating is introduced, there is a shift downwards, however in this case it does not match the levels of the 20PPI Cu-S configuration. The error bars, showing standard deviation are more compact when compared to the 10PPI configurations, suggesting that the 20PPI plated foams act more consistently than the 10PPI configurations.

Again, it is seen in Figure 5.3-11 that there is no significant reduction of temperature change at the cell surface when the electroless plating configurations are compared, if all three showed the 0.5 °C uncertainty rather than the standard deviation, it would be hard to distinguish the three apart.
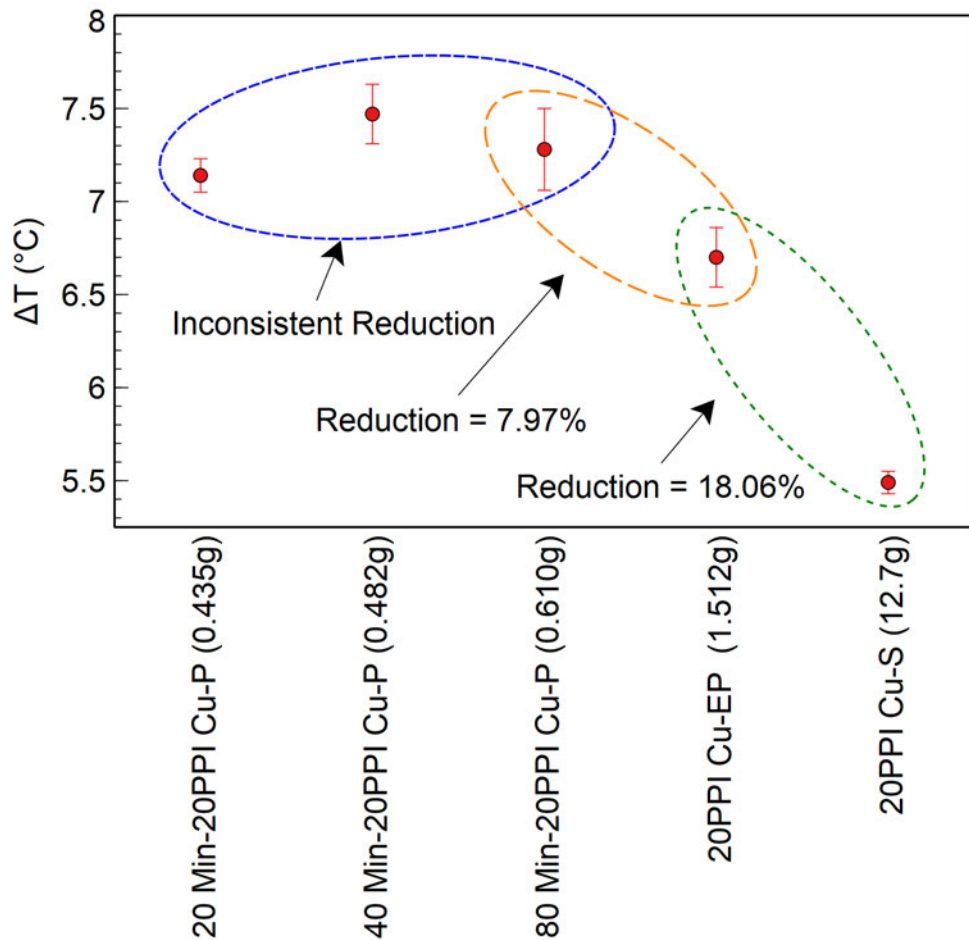
Figure 5.3-11: Temperature change of 20PPI Configurations

The electroplated configuration shows to be 7.97% lower than the 80-minute electroless plated configuration, which is a significant result as it shows that the elector plating on the electroless plated foam skeleton further aids the heat transfer into the PCM, as seen in the 10PPI configuration. There is still a significant gap between the Cu-EP configuration and the Cu-S configuration, 18.06%, which contrasts that of the 10PPI configurations, however, it is shown that the 20PPI Cu-S is more effective at reducing the temperature change compared to the 10PPI configuration.

When comparing the best two 20PPI Configurations i.e., the 20PPI Cu-EP and 20PPI Cu-S configurations, to the cell only, it is shown that these configurations also provide a substantial reduction of the cell surface temperature, similar to the 10PPI variants. It is calculated for the 20PPI Cu-EP configuration, there is a 62.17% decrease in the cells' average surface temperature, only 1.06% variation compared to the 10PPI equivalent, while the Cu-S Configuration provides a further 6.83% achieving a 69% temperature reduction.

5.3.2.3 Foam Density Comparison

All plated configurations the solid foam configurations are shown in Figure 5.3-12 with 10mm PCM configuration. It is shown in the order of plating time for the Cu-P configurations, then the electroless plated foam configurations, and finally the solid copper foam configurations. It is visible that as the plating time increases and subsequently the plated copper mass, the temperature delta doesn't decrease as expected.

The 20-minute configurations show a lower value more in line with the 80-minute configurations. As discussed in the 10PPI and 20PPI sub-chapters previously, the electroless plating and plated mass do not induce a significant temperature change when compared to each other, it is only when electroplating configurations is used where a more significant drop of temperature at the cell surface is seen. The remainder of this section will discuss and compare the difference in the foam densities at each copper plating time and configuration.
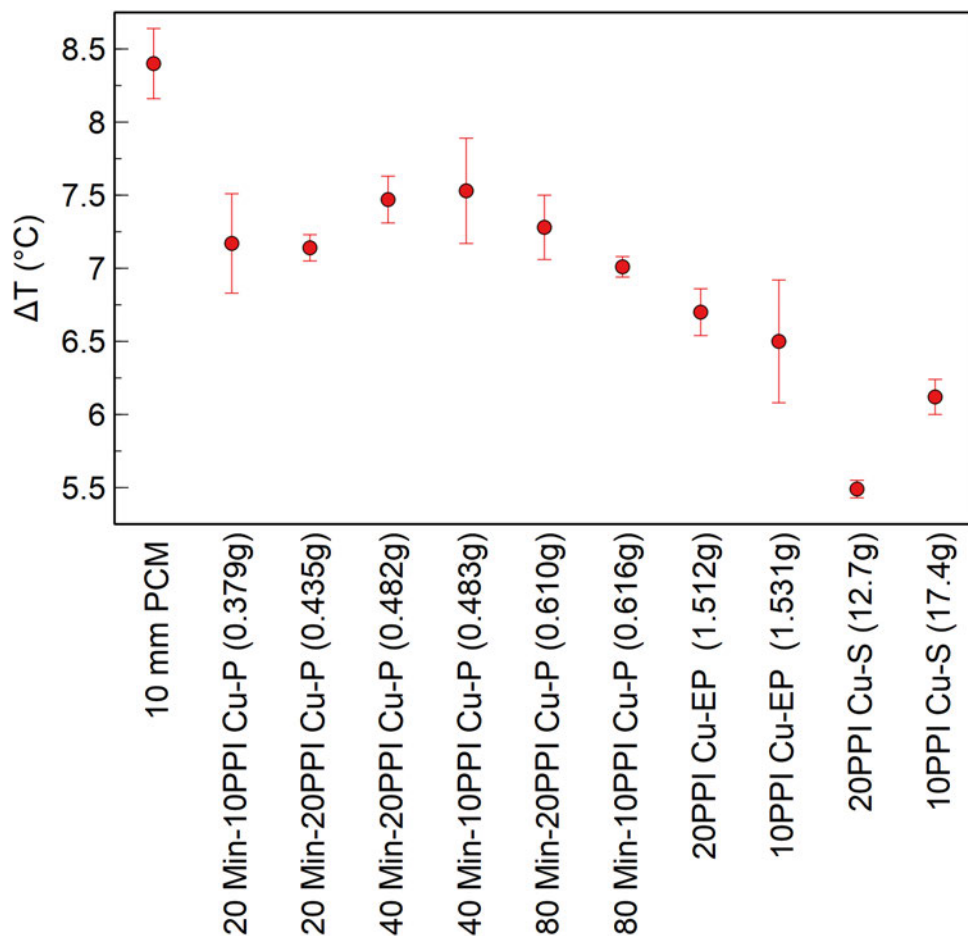
Figure 5.3-12: All configurations with copper foam, shown with 10mm PCM configuration.
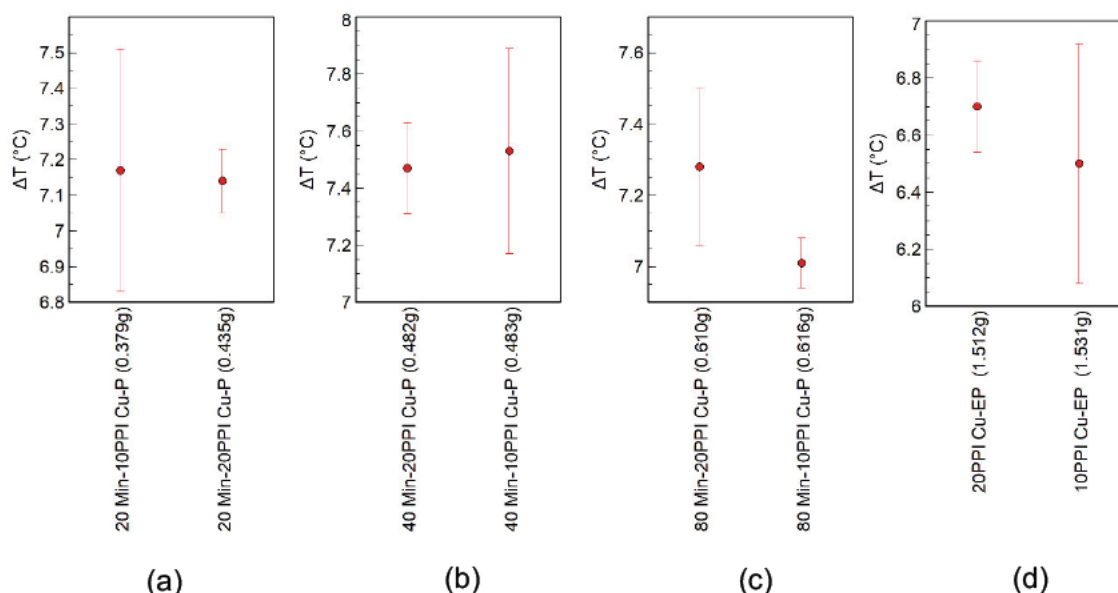
Figure 5.3-13: Comparisons of pore density (a) 20 minutes plating time, (b) 40 minutes plating time, (c) 80 minutes plating time, and (d) electroplating.

Figure 5.3-13 (a) shows the comparison of the 20-minute plating process, the two configurations, 10PPI Cu-P and 20PPI Cu-P show to be very similar at around 7.15 °C, however, the 10 PPI variant shows a much larger standard deviation, almost in line with the 0.5 °C uncertainty of the TC-08 data logger. However, apply the 0.5 °C uncertainty and these two configurations look to be almost identical. The 10PPI variation shows 0.056g less copper mass. As these configurations show similarities in thermal response, it further demonstrates that the electroless plating is not sufficient to show any major variation at this quantity.

Figure 5.3-13 (b) shows that there is virtually no difference between the 10PPI and 20PPI not only in the temperature change but also in the mass of plating achieved with there being only a 0.001g difference between the samples. It is shown that the 10PPI variant has a larger standard deviation. The 40-minute configurations show to have a marginally higher temperature change over the 20-minute configurations, however as discussed, these are all within the same area and are all within the 0.5°C uncertainty.

The 80-minute configurations begin to show more deviation, Figure 5.3-13 (c), where the 10PPI variation shows to be around 0.2 °C lower than the 20PPI variation, however as with the previous two plating durations, as soon as a 0.5°C uncertainty is in place for the error bars it would show a strong overlap and these two configurations would show to be very similar. Additionally, if a 0.5 °C error

was placed at 7 °C it would capture all the electroplated configurations, thus it can be determined overall that the electroplating at this scale does not add a significant quantity of copper onto the substrate between the 20 and 80 minutes to influence the temperature change beyond the 0.5 °C uncertainty.

When electroplating is introduced a more significant drop in temperature change is seen, Figure 5.3-13 (d), where 10PPI Cu-EP shows to be the best configuration, all be it with a larger standard deviation compared to the 20PPI Cu-EP configuration. As discussed previously, the electroplated Cu-EP configurations show the most comparability with the commercial foam Cu-S configurations.

5.3.3 Cost Analysis

A cost analysis of the Cu-P foam samples is discussed and compared to the cost of the commercial copper foam purchased for this study. The cost analysis considers only the foam and the chemical components used in the copper plating bath. All other components such as the PCM, PLA for the case, battery, connectors, and electricity used during plating is not considered. The chemicals used in the preparation of the PU foam skeleton was not considered as these are reused several times, except in the case of the sodium hypophosphite as this is used only once.

The commercial foam was purchased for this study directly from GoodFellow. The cost of the foam pieces was, £477 and £487 for the 10PPI and 20PPI pieces respectively. Both pieces of copper foam were 200mm x 200mm and 5mm thick. A summarised quotation from GoodFellow can be seen in Appendix E.

Each piece of commercial copper is 40,000 mm^2 in theoretical area i.e., not accounting for pores, just considering length and breadth dimensions. The two configurations with commercial foam require 4 pieces of foam 30 mm x 42 mm, thus requiring 5040 mm^2 of foam. Therefore, each piece of foam can be used to create 7.936 configurations, rounding down to 7 configurations, each 10PPI configuration costs approximately £68.14, and each 20 PPI configuration costs £69.57.

The cost of the electroplating chemicals are listed in **Table 11** as the cost per gram or millilitre. Where appropriate the cost per gram is calculated from the cost of 100g container. The cost per millilitre is derived from the cost of 1 litre of

solution. The source of the chemical is listed and price excluding VAT is correct as of 27th July 2022.

Table 11: Cost Breakdown of Electroless Plating Chemicals

Chemical	£/100g	£/g	£/L	£/ml	Source
Copper (II) sulphate Pentahydrate	£31.10	£0.311	-	-	Sigma Aldrich
EDTA	£39.40	£0.394	-	-	Sigma Aldrich
Sodium Hypophosphite Hydrate	£30.80	£0.308	-	-	Sigma Aldrich
2-MBT	£26.20	£0.262	-	-	Sigma Aldrich
Glyoxylic Acid (50% wt) Solution in Water	-	-	£28.12	£0.028	Sigma Aldrich

Table 12 shows the total cost of the plating bath chemicals which is used to manufacture the electroless copper plated foam skeletons in this thesis. The qualities are described earlier in this chapter.

The PU foam used in this study was already purchased by the university some years previous, thus a cost is not known. However, appendix F shows a quote for 10 and 20 PPI Polyester foam from Zouch Converters Ltd. The cost for 150mm x 210mm x 10mm (31,500 mm^2) foam is £2.85 and £2.66 for 10PPI for 20PPI respectively. This results in approximately £ 0.96 for 10PPI and £0.90 for 20PPI per configuration, considering 6 usable foam pieces from each whole foam piece.

Using these values, the total cost of electroless copper plated PU foam for the specified application in this thesis is £6.70 for 10PPI and £6.64 for 20PPI. In comparison to the commercially available solid copper foam from GoodFellow, the in house manufactured foam is 91.17% cheaper for 10PPI and 90.46% cheaper for 20PPI.

Table 12: Cost breakdown of electroless plating bath

Chemical	Quantity	Cost
Copper (II) Sulphate Pentahydrate	4 g	£1.24
EDTA	8 g	£3.15
Sodium Hypophosphite Hydrate	0.4 g	£1.23
2-MBT	0.4 mg	£0.0001
Glyoxylic Acid (50% wt) Solution in Water	*4.2 g*	*£0.12*
	Total	£5.74

Cost for 200ml of solution

The cost saving for the electroless plated foam samples is substantial when compared to the commercial alternative. The configurations with the additional electroplated copper also show a substantial reduction. When considering a cost per gram of pure copper, the London Metal Exchange (LME) shows $7976 USD per tonne of pure copper (accurate as of 11th August 2022 at 14:15pm). This equates to £6521.10 GBP per metric tonne, resulting in approximately £6.52 per kilogram of pure copper, with this the total cost of the electroplated configurations is derived to be £7.26 and £7.22 for the 10PPI and 20PPI configurations respectively. This shows the in house manufactured foam with electroplated copper to be 89.30% cheaper for 10PPI and 89.62% cheaper for 20PPI, when compared to the commercial copper foam.

5.4 Conclusion

The investigation outlined in this chapter shows the results of the experimental analysis of different copper masses deposited onto the surface of polyurethane foam. With three different electroless plating durations, 20, 40 and 80 minutes and then 80-minute electroless deposition and 20-minute electroplating combined (Cu-EP) to create four manufactured configurations of foam for

impregnation with RT31 PCM. A comparison is made to cell-only discharge with no passive cooling, 10mm PCM only for passive cooling (10 mm PCM), and non-plated polyurethane foam impregnated with PCM (10 mm - PU) and PCM-impregnated commercial copper foam (Cu-P). Foam densities of 10PPI and 20PPI are compared in each instance.

It is shown in the results of this proof-of-concept investigation that PCM on its own can reduce the cell temperature by 49.39% with 5 mm of RT31 PCM around the cell, the doubling of the PCM only adds a further 2.35% reduction to 51.42%. It is demonstrated that simply doubling the PCM thickness does not result in the doubling of thermal storage, due to the low thermal conductivity of the PCM.

The addition of foam into the PCM increases the storage potential of the PCM, as found in the literature. The findings of the experimentation in this chapter demonstrate that the addition of electroless copper plating onto polyurethane foam substrates of both 10PPI and 20PPI can reduce the cell temperature of a commercial polymer Li-ion battery further.

When comparing the Cu-P configurations to the Cu-S configurations, it is shown that the solid copper foam (Cu-S) in both densities has a significant advantage over the copper-plated configurations (Cu-P), however, the mass differential between the two foam types is also significant, where it is possible to justify increasing the electroless plating mass attempting to close the gap between the foam configurations. Additionally, this chapter aims to further develop the Cu-P to increase the heat absorbed by the PCM, closer to the levels of the Cu-S configurations. The mass of the plating is increased by longer plating times set out by the literature and the addition of electroplating onto the electroless plated substrate.

The consistent start temperature of each 1.5 C discharge experiment allows for a good comparison of the foam configurations. It is found that in both the 10 and 20 PPI configurations the three Cu-P configurations with different plating times show no significant reduction of cell temperature change when compared to each other. This is also true for the 10PPI configurations when the Cu-P configurations are compared directly to the 10PPI PU configuration, however, there is a drop in temperature change with the 20PPI configurations.

It is shown that there is no considerable difference between the foam densities, even when considering the Cu-EP configurations. It is shown in the discussion that if the 0.5 °C uncertainty is considered for the TC sensors. There is no significant change between the foam densities in each case considered.

The most effective configuration i.e., the 10PPI Cu-EP shows an average cell surface temperature reduction of 63.23% which is close to the sold 10PPI configuration with a 65.44% temperature reduction. This is significant as there is a substantial difference in the mass of the foam skeletons, where the Cu-EP configuration has 91.47% less mass compared to the Cu-S configuration. This is also true for the 20PPI configurations, where the Cu-EP configuration has 88.5% less mass than the Cu-S configuration of the same foam density, there is also a significant drop of the average cell surface temperature, 62.17%. Compared to the 69% reduction of cell surface temperature for the commercial 20PPI foam, this is still a successful result. It is also important to note that there is a substation cost saving where the in house manufactured Cu-EP foam is 89.30% cheaper for 10PPI and 89.62% cheaper for 20PPI, when compared to the commercial copper foam.

While the experimental results show that there is little consistency in the electroless plating, it does show that the addition of copper on the foam skeleton does reduce the cell surface temperature, thus it can be determined that the plated copper mass is aiding in the heat transfer, unlocking further storage capacity of the PCM.

It is shown in this work that there are advantages to the copper deposition of PU foams for the enhancement of PCM thermal conductivity for battery management applications, namely with the substantial reduction of copper mass to achieve similar properties to commercial solid copper foams.

Chapter 6: Conclusions and Future Work

6.1 Conclusions

It is undoubtedly important to monitor and manage the temperature of the lithium-ion battery. As demonstrated in the literature, over-temperature plays a detrimental role in the accelerated degradation of the LIB cell. To combat this the temperature in a commercial LIB pack is recorded at strategic locations throughout and the temperature is provided to the Battery Thermal Management System, where a cooling system, typically indirect liquid cooling or forced air cooling is deployed to manage the thermal gradients.

Chapter three of this work demonstrated a method of utilising a small tube piece made form PVC, to mount a FOS with FBG to measure the lithium-ion battery surface temperature without the use of a full length microtube for the decoupling of temperature and strain. The method, named 'guide tube', demonstrates that the FBGs can provide accurate temperature measurements. The method allows for the FBGs to be uncovered against the battery surface and when compared to a mounting method which holds the FOS in position with glue, restricting the expansion and contraction, the method shows higher accuracy when compared against thermocouple sensors. The accuracy of the temperature readings improves from $\pm$ 4.25 °C to +2.13 °C when the guide tube method is adopted. The research in this chapter was submitted to the 'Sensors and Actuators A: Physical' journal and published in December 2021.

Chapter 4 of this thesis builds on the guide tube method devised in chapter 3 by incorporating a PTFE microtube with specifically designed ABS plinths for adhesion to the LIB surface. This setup allows the FOS with five FBGs to sit across the three cell LIB pack. This method glues the FOS at one side of the LIB pack and uses the PTFE tube at the other side of the LIB pack to decouple strain and temperature to provide only temperature response from the FBGs.

This experimental work deploys three FBGs, one at each of the three LIB cells and one between the cells, the five FBGs are used for temperature measurement of 0.5 C, 2 C and 40CW discharge. The results of this testing regime show an average error of 0.97 °C, 1.33 °C, and 1.27 °C for FBG1 on cell

1, FBG 3 on cell 2 and FBG 5 on cell 3 respectively, which is a significant improvement compared to the +2.13 °C error achieved in the setup detailed in chapter 3.

It is shown that in addition to temperature measurement at the individual cell level, it is possible to capture temperature data between cells, demonstrated by the temperature response of FBG 2 and FBG 4 for each discharge condition. Additionally, it is evident from the regression data, specifically the standard error that the FBG 3 response, situated in the middle of the mounted FOS strand shows a more varied response. It is possible to hypothesise that the larger error seen over the three discharge tests indicated a slack in the FOS which is minimally interfering with the temperature measurements. Overall, the guide tube shows a promising method for the mounting of a FOS strand without the need for a full microtube along the length of the FOS strand. It is planned that this research will be published in a peer review journal in the coming months.

Chapter five, the final research chapter of this thesis, details the proof-of-concept study of the novel application for electroless deposition on polyurethane foam to passively manage the thermal gradient of a LIB. PCM. It is found that on its own PCM can reduce the cell temperature by 49.39% with 5 mm of RT31 PCM and 51.42% with 10 mm.

The most effective configuration found in this study is the commercial 20PPI copper foam (20PPI Cu-S) which achieved 68.28% reduction of the cells surface temperature. The most effective copper plated configuration i.e., the 10PPI Cu-EP shows an average cell surface temperature reduction of 63.23% which is close to the sold 10PPI configuration with a 65.44% temperature reduction.

While the electroless foam enhances the PCM, unlocking more thermal storage, it is shown that the electroless plating time with the methodology used in the plating process does not significantly alter the effectiveness to enhance the thermal storage of the PCM. However, the results of this work show that the commercial foam can be replaced by the copper plated equivalents which have has a substantial reduction of copper mass, in this case to the extent of 91.47%, resulting in a potential cost saving of up to 89.30%, when considering the most effective configuration, 10PPI Cu-EP. It is planned that this research will be published in a peer review journal in the coming months.

6.2 Future Work

The outcomes of the copper plating investigation and the individual cell monitoring will be published in two further peer-reviewed articles that will be submitted in the upcoming months. In addition, some further study directions are discussed in the following subsections to further the research carried out for this thesis.

6.2.1 FBGs for Thermal Monitoring

The works detailing the implementation of the guide tube for individual cell monitoring highlighted some areas of future development. As seen in the results, the middle FBG, (FBG 3) showed possible solution for future work would be to apply a method to support the FBG around the cell without interfering with the FBG situated at the cell surface. It would also be advantageous to further develop the multiplexing method to measure more cells in a larger battery pack.

Additionally, the use of FBGs in between cells is advantageous as the temperature variation seen in these strategically placed sensors could be used to assess and investigate the radiating heat from cells within a battery pack. Due to the small dimensions and minimally invasive nature of FBG sensors, it is possible to situate FBGs within the small gaps between cells, providing more data to the BTMS.

6.2.2 Copper Foam Design and Manufacture

While the copper plating process used in this study successfully demonstrated the utilisation of electroless and electroplating of polymer substrates for the LIB's temperature management, there are still a number of areas which require further investigation.

Since the experimental investigation shows that the small mass changes between the electroless plating configurations show little difference between each other, it is suggested that further research could concentrate on enhancing the electroless plating method to plate the copper at a higher rate or adapting the solution to include a higher concentration of copper. This would involve considerable amount of chemistry-based work, as the electroless copper plating solution is inherently unstable, as was previously mentioned.

Additionally, it would be advantageous to further investigate the electroplating as this resulted in a larger deposition mass compared to the electroless plating. The electroless plating of the foam will still be necessary to provide a conductive substrate for the electroplating process, but nickel might be used in a more straightforward manner to accomplish this.

Finally, the inclusion of the FBG sensors within the foam composites would provide an interesting investigation. When the PCM is added to the foam structure, a procedure would require development allowing the FOS strand to be integrated into the foam and thermally compensated. Theoretically, this might be accomplished by cutting a channel or groove into the foam structure before plating, then adding a microtube inside the channel/groove before being impregnated with PCM. To accurately measure the cell temperature, this must be located close to the LIB cell's surface. As an alternative, the PCM's temperature during phase shift might be recorded using the FBG.

References

[1]   S. Ma *et al.*, "Temperature effect and thermal impact in lithium-ion batteries: A review," *Progress in Natural Science: Materials International,* vol. 28, no. 6, pp. 653-666, 2018/12/01/ 2018, doi: https://doi.org/10.1016/j.pnsc.2018.11.002.

[2]   A. Sarkar, P. Shrotriya, and A. Chandra, "Parametric Analysis of Electrode Materials on Thermal Performance of Lithium-Ion Battery: A Material Selection Approach," *Journal of The Electrochemical Society,* vol. 165, no. 9, p. A1587, 2018/05/25 2018, doi: 10.1149/2.0061809jes.

[3]   S. Wang *et al.*, "Chapter 1 - Lithium-ion battery characteristics and applications," in *Battery System Modeling*, S. Wang *et al.* Eds.: Elsevier, 2021, pp. 1-46.

[4]   Z. Liao, S. Zhang, K. Li, G. Zhang, and T. G. Habetler, "A survey of methods for monitoring and detecting thermal runaway of lithium-ion batteries," *Journal of Power Sources,* vol. 436, p. 226879, 2019/10/01/ 2019, doi: https://doi.org/10.1016/j.jpowsour.2019.226879.

[5]   Forbes. "What Business Leaders Should Know About Lithium-Ion Battery Applications." Forbes.com. https://www.forbes.com/sites/forbesbusinessdevelopmentcouncil/2021/08/18/what-business-leaders-should-know-about-lithium-ion-battery-applications/?sh=147b35bd76c1 (accessed 17/08/2022, 2022).

[6]   J. Twidell and T. Weir, *Renewable energy resources*, 3rd edition. ed. Ann Arbor, Mich: ProQuest, 2015.

[7]   , "Chapter 1 - Development of energy storage technology," in *Grid-scale Energy Storage Systems and Applications*, F.-B. Wu, B. Yang, and J.-L. Ye Eds.: Academic Press, 2019, pp. 1-15.

[8]   BBC News. "Tesla mega-battery in Australia activated." BBC News. https://www.bbc.co.uk/news/world-australia-42190358 (accessed 24/09/2021, 2021).

[9]   E. McTurk, "Bottling Electricity," in *The Fully Charged Guide to Electric Vehicles and Clean Energy*, R. Llewellyn Ed.: Unbound, 2020, pp. 32-35.

[10]   S. Srdic and S. Lukic, "Toward Extreme Fast Charging," *Ieee Electrification Mag,* vol. 7, no. 1, pp. 22-31, 2019, doi: 10.1109/mele.2018.2889547.

[11]   A. Hnatov, S. Arhun, K. Tarasov, H. Hnatova, V. Mygal, and A. Patlins, "Researching the model of electric propulsion system for bus using Matlab Simulink," *IEEE 60th International Scientific Conference on Power and Electrical Engineering of Riga Technical University (RTUCON),* pp. 1-6, 2019, doi: 10.1109/rtucon48111.2019.8982352.

[12]   X. G. Yang, S. Ge, N. Wu, Y. Mao, F. Sun, and C. Y. Wang, "All-Climate Battery Technology for Electric Vehicles: Inching Closer to the Mainstream Adoption of Automated Driving," *Ieee Electrification Mag,* vol. 7, no. 1, pp. 12-21, 2019.

[13]   M. Tariq, A. I. Maswood, C. J. Gajanayake, and A. K. Gupta, "A Lithium-ion battery energy storage system using a bidirectional isolated DC-DC converter with current mode control for More Electric Aircraft," *2016 Ieee Symposium*

Comput Appl Industrial Electron Iscaie, pp. 149-154, 2016, doi: 10.1109/iscaie.2016.7575054.

[14] X. Feng, M. Ouyang, X. Liu, L. Lu, Y. Xia, and X. He, "Thermal runaway mechanism of lithium ion battery for electric vehicles: A review," *Energy Storage Mater,* vol. 10, pp. 246-267, 2018, doi: 10.1016/j.ensm.2017.05.013.

[15] J. Meyer, A. Nedjalkov, A. Doering, M. Angelmahr, and W. Schade, "Fiber optical sensors for enhanced battery safety," *Fiber Optic Sensors and Applications XII,* vol. 9480, p. 94800Z, 2015, doi: 10.1117/12.2183325.

[16] S. S. Zhang, K. Xu, and T. R. Jow, "Charge and discharge characteristics of a commercial LiCoO2-based 18650 Li-ion battery," *Journal of Power Sources,* vol. 160, no. 2, pp. 1403-1409, 2006, doi: 10.1016/j.jpowsour.2006.03.037.

[17] J. Meyer, A. Nedjalkov, E. Pichler, C. Kelb, and W. Schade, "Development of a Polymeric Arrayed Waveguide Grating Interrogator for Fast and Precise Lithium-Ion Battery Status Monitoring," *Batter,* vol. 5, no. 4, p. 66, 2019, doi: 10.3390/batteries5040066.

[18] G. Yang, C. Leitão, Y. Li, J. Pinto, and X. Jiang, "Real-time temperature measurement with fiber Bragg sensors in lithium batteries for safety usage," *Measurement,* vol. 46, no. 9, pp. 3166-3172, 2013, doi: 10.1016/j.measurement.2013.05.027.

[19] M. Nascimento, M. S. Ferreira, and J. L. Pinto, "Real time thermal monitoring of lithium batteries with fiber sensors and thermocouples: A comparative study," *Measurement: Journal of the International Measurement Confederation,* vol. 111, pp. 260-263, 2017, doi: 10.1016/j.measurement.2017.07.049.

[20] A. Fortier, M. Tsao, N. D. Williard, Y. Xing, and M. G. Pecht, "Preliminary study on integration of fiber optic bragg grating sensors in li-ion batteries and in situ strain and temperature monitoring of battery cells," *Energies,* vol. 10, no. 7, 2017, doi: 10.3390/en10070838.

[21] E. Gümüşsu, Ö. Ekici, and M. Köksal, "3-D CFD modeling and experimental testing of thermal behavior of a Li-Ion battery," *Appl Therm Eng,* vol. 120, pp. 484-495, 2017, doi: 10.1016/j.applthermaleng.2017.04.017.

[22] C. Essl *et al.*, "Comprehensive Hazard Analysis of Failing Automotive Lithium-Ion Batteries in Overtemperature Experiments," *Batter,* vol. 6, no. 2, p. 30, 2020, doi: 10.3390/batteries6020030.

[23] D. Rand, R. Woods, and R. Dell, *Batteries for Electric Vehicles*. Research Studied Press Ltd, 1998.

[24] A. Thaler and D. Watzenig, *Automotive Battery Technology* (SpringerBriefs in Applied Sciences and Technology). Cham: Springer International Publishing, 2014.

[25] Z. Wei, J. Zhao, H. He, G. Ding, H. Cui, and L. Liu, "Future smart battery and management: Advanced sensing from external to embedded multi-dimensional measurement," *Journal of Power Sources,* vol. 489, p. 229462, 2021/03/31/ 2021, doi: https://doi.org/10.1016/j.jpowsour.2021.229462.

[26] C. R. Birkl, M. R. Roberts, E. McTurk, P. G. Bruce, and D. A. Howey, "Degradation diagnostics for lithium ion cells," *Journal of Power Sources,* vol.

341, pp. 373-386, 2017/02/15/ 2017, doi: https://doi.org/10.1016/j.jpowsour.2016.12.011.

[27]   R. Sabbah, R. Kizilel, J. R. Selman, and S. Al-Hallaj, "Active (air-cooled) vs. passive (phase change material) thermal management of high power lithium-ion packs: Limitation of temperature rise and uniformity of temperature distribution," *Journal of Power Sources,* vol. 182, no. 2, pp. 630-638, 2008/08/01/ 2008, doi: https://doi.org/10.1016/j.jpowsour.2008.03.082.

[28]   Q. Wang *et al.*, "Experimental investigation on EV battery cooling and heating by heat pipes," *Appl Therm Eng,* vol. 88, pp. 54-60, 2015/09/05/ 2015, doi: https://doi.org/10.1016/j.applthermaleng.2014.09.083.

[29]   L. H. Saw, Y. Ye, and A. A. O. Tay, "Integration issues of lithium-ion battery into electric vehicles battery pack," *Journal of Cleaner Production,* vol. 113, pp. 1032-1045, 2016/02/01/ 2016, doi: https://doi.org/10.1016/j.jclepro.2015.11.011.

[30]   R. Kizilel, R. Sabbah, J. R. Selman, and S. Al-Hallaj, "An alternative cooling system to enhance the safety of Li-ion battery packs," *Journal of Power Sources,* vol. 194, no. 2, 2009, doi: 10.1016/j.jpowsour.2009.06.074.

[31]   T. Wang, K. J. Tseng, J. Zhao, and Z. Wei, "Thermal investigation of lithium-ion battery module with different cell arrangement structures and forced air-cooling strategies," *Applied Energy,* vol. 134, pp. 229-238, 2014/12/01/ 2014, doi: https://doi.org/10.1016/j.apenergy.2014.08.013.

[32]   M. Bass, *Handbook of Optics: Fundamentals, Techniques, & Design*, 2nd ed. McGraw-Hill, 1995, p. 1606.

[33]   C. M. Jha and J. A. Sanchez, "Microprocessor Temperature Sensing and Thermal Management," in *Thermal Sensors: Principles and Applications for Semiconductor Industries*, C. M. Jha Ed. New York, NY: Springer New York, 2015, pp. 57-96.

[34]   J. Cao and A. Emadi, "Batteries Need Electronics," *IEEE Industrial Electronics Magazine,* vol. 5, no. 1, pp. 27-35, 2011, doi: 10.1109/MIE.2011.940251.

[35]   T. Waldmann *et al.*, "Influence of Cell Design on Temperatures and Temperature Gradients in Lithium-Ion Cells: An In Operando Study," *Journal of The Electrochemical Society,* vol. 162, no. 6, pp. A921-A927, 2015, doi: 10.1149/2.0561506jes.

[36]   M. Debert, G. Colin, G. Bloch, and Y. Chamaillard, "An observer looks at the cell temperature in automotive battery packs," *Control Engineering Practice,* vol. 21, no. 8, pp. 1035-1042, 2013/08/01/ 2013, doi: https://doi.org/10.1016/j.conengprac.2013.03.001.

[37]   Z. H. Che Daud, D. Chrenko, F. Dos Santos, E.-H. Aglzim, A. Keromnes, and L. Le Moyne, "3D electro-thermal modelling and experimental validation of lithium polymer-based batteries for automotive applications," *International Journal of Energy Research,* https://doi.org/10.1002/er.3524 vol. 40, no. 8, pp. 1144-1154, 2016/06/25 2016, doi: https://doi.org/10.1002/er.3524.

[38]   S. Tippmann, D. Walper, L. Balboa, B. Spier, and W. G. Bessler, "Low-temperature charging of lithium-ion cells part I: Electrochemical modeling and experimental investigation of degradation behavior," *Journal of Power Sources,*

vol. 252, pp. 305-316, 2014/04/15/ 2014, doi: https://doi.org/10.1016/j.jpowsour.2013.12.022.

[39]   D. Chalise, K. Shah, T. Halama, L. Komsiyska, and A. Jain, "An experimentally validated method for temperature prediction during cyclic operation of a Li-ion cell," *International Journal of Heat and Mass Transfer,* vol. 112, pp. 89-96, 2017/09/01/ 2017, doi: https://doi.org/10.1016/j.ijheatmasstransfer.2017.04.115.

[40]   @PeakSensors. "What Is A Pt100 Sensor? [Full Definition] - Peak Sensors." @PeakSensors. https://peaksensors.co.uk/what-is/pt100-sensor/ (accessed.

[41]   "PT100 sensors (Platinum Resistance Thermometers or RTD sensors)." https://www.picotech.com/library/application-note/pt100-platinum-resistance-thermometers (accessed 08/07/22, 2022).

[42]   E. Sensors. "What are the Pt100 accuracy classes? | EPIC® SENSORS." https://www.epicsensors.com/en/faq/what-are-the-pt100-accuracy-classes/ (accessed 08/07/2022, 2022).

[43]   J. Huang, S. T. Boles, and J.-M. Tarascon, "Sensing as the key to battery lifetime and sustainability," *Nature Sustainability,* vol. 5, no. 3, pp. 194-204, 2022/03/01 2022, doi: 10.1038/s41893-022-00859-y.

[44]   Marcelo M. Werneck, Regina C. S. B. Allil, B. A. Ribeiro, and F. V. B. d. Nazaré, "A Guide to Fiber Bragg Grating Sensors," in *Current trends in short-and long-period fiber gratings*, C. Cuadrado-Laborde Ed.: BoD–Books on Demand, 2013.

[45]   G. Han, J. Yan, Z. Guo, D. Greenwood, J. Marco, and Y. Yu, "A review on various optical fibre sensing methods for batteries," *Renewable and Sustainable Energy Reviews,* vol. 150, p. 111514, 2021/10/01/ 2021, doi: https://doi.org/10.1016/j.rser.2021.111514.

[46]   W. R. Habel, "Optical Fiber Methods in Nondestructive Evaluation," in *Handbook of Advanced Non-Destructive Evaluation*, N. Ida and N. Meyendorf Eds. Cham: Springer International Publishing, 2018, pp. 1-49.

[47]   Y.-J. Rao, "In-fibre Bragg grating sensors," *Measurement Science and Technology,* vol. 8, no. 4, pp. 355-375, 1997/04/01 1997, doi: 10.1088/0957-0233/8/4/002.

[48]   C. Cuadrado-Laborde, *Current trends in short-and long-period fiber gratings*. BoD–Books on Demand, 2013.

[49]   D. L. Romanyk, H. Yu, M. Grotski, S. Seo, O. Addison, and C. R. Dennison, "In situ measurement of dental resin-based composite volumetric shrinkage and temperature effects using in-fibre bragg grating methods," *Journal of the Mechanical Behavior of Biomedical Materials,* vol. 95, pp. 89-95, 2019/07/01/ 2019, doi: https://doi.org/10.1016/j.jmbbm.2019.03.026.

[50]   L. Liu, H. Zhang, Q. Zhao, Y. Liu, and F. Li, "Temperature-independent FBG pressure sensor with high sensitivity," *Optical Fiber Technology,* vol. 13, no. 1, pp. 78-80, 2007/01/01/ 2007, doi: https://doi.org/10.1016/j.yofte.2006.09.001.

[51]   C.-H. Lee, M.-K. Kim, K. Kim, and J. Lee, "Enhanced temperature sensitivity of fiber Bragg grating temperature sensor using thermal expansion of copper

tube," *Microwave and Optical Technology Letters,* vol. 53, pp. 1669-1671, 07/01 2011, doi: 10.1002/mop.26032.

[52]   L. Wang, Y. Wang, J. Wang, and F. Li, "A High Spatial Resolution FBG Sensor Array for Measuring Ocean Temperature and Depth," *Photonic Sensors,* vol. 10, no. 1, pp. 57-66, 2020/03/01 2020, doi: 10.1007/s13320-019-0550-0.

[53]   E. Vergori and Y. Yu, "Monitoring of Li-ion cells with distributed fibre optic sensors," *Procedia Structural Integrity,* vol. 24, pp. 233-239, 2019/01/01/ 2019, doi: https://doi.org/10.1016/j.prostr.2020.02.020.

[54]   Y. Yu, T. Vincent, J. Sansom, D. Greenwood, and J. Marco, "Distributed internal thermal monitoring of lithium ion batteries with fibre sensors," *Journal of Energy Storage,* vol. 50, p. 104291, 2022/06/01/ 2022, doi: https://doi.org/10.1016/j.est.2022.104291.

[55]   J. Peng, S. Jia, H. Yu, X. Kang, S. Yang, and S. Xu, "Design and Experiment of FBG Sensors for Temperature Monitoring on External Electrode of Lithium-Ion Batteries," *IEEE Sensors Journal,* vol. 21, no. 4, pp. 4628-4634, 2021, doi: 10.1109/JSEN.2020.3034257.

[56]   E. McTurk, T. Amietszajew, J. Fleming, and R. Bhagat, "Thermo-electrochemical instrumentation of cylindrical Li-ion cells," *Journal of Power Sources,* vol. 379, pp. 309-316, 2018, doi: 10.1016/j.jpowsour.2018.01.060.

[57]   J. Fleming, T. Amietszajew, E. McTurk, D. Greenwood, and R. Bhagat, "Development and evaluation of in-situ instrumentation for cylindrical Li-ion cells using fibre optic sensors," *Hardwarex,* vol. 3, pp. 100-109, 2018, doi: 10.1016/j.ohx.2018.04.001.

[58]   S. Novais *et al.*, "Internal and External Temperature Monitoring of a Li-Ion Battery with Fiber Bragg Grating Sensors," *Sensors,* vol. 16, no. 9, 2016, doi: 10.3390/s16091394.

[59]   R. Zhao, J. Liu, J. Gu, L. Zhai, and F. Ma, "Experimental study of a direct evaporative cooling approach for Li-ion battery thermal management," *International Journal of Energy Research,* https://doi.org/10.1002/er.5402 vol. 44, no. 8, pp. 6660-6673, 2020/06/25 2020, doi: https://doi.org/10.1002/er.5402.

[60]   N. Sato, "Thermal behavior analysis of lithium-ion batteries for electric and hybrid vehicles," *Journal of Power Sources,* vol. 99, no. 1, pp. 70-77, 2001/08/01/ 2001, doi: https://doi.org/10.1016/S0378-7753(01)00478-5.

[61]   S. Panchal, I. Dincer, M. Agelin-Chaab, R. Fraser, and M. Fowler, "Experimental temperature distributions in a prismatic lithium-ion battery at varying conditions," *International Communications in Heat and Mass Transfer,* vol. 71, pp. 35-43, 2016, doi: 10.1016/j.icheatmasstransfer.2015.12.004.

[62]   G. Zhao, X. Wang, M. Negnevitsky, and H. Zhang, "A review of air-cooling battery thermal management systems for electric and hybrid electric vehicles," *Journal of Power Sources,* vol. 501, p. 230001, 2021/07/31/ 2021, doi: https://doi.org/10.1016/j.jpowsour.2021.230001.

[63]   L. Fan, J. M. Khodadadi, and A. A. Pesaran, "A parametric study on thermal management of an air-cooled lithium-ion battery module for plug-in hybrid

electric vehicles," *Journal of Power Sources,* vol. 238, pp. 301-312, 2013/09/15/ 2013, doi: https://doi.org/10.1016/j.jpowsour.2013.03.050.

[64]   G. Xia, L. Cao, and G. Bi, "A review on battery thermal management in electric vehicle application," *Journal of Power Sources,* vol. 367, pp. 90-105, 2017/11/01/ 2017, doi: https://doi.org/10.1016/j.jpowsour.2017.09.046.

[65]   A. Ibrahim, J. Guo, Y. Wang, Y. Zheng, B. Lei, and F. Jiang, "Performance of serpentine channel based Li-ion battery thermal management system: An experimental investigation," *International Journal of Energy Research,* https://doi.org/10.1002/er.5599 vol. 44, no. 13, pp. 10023-10043, 2020/10/25 2020, doi: https://doi.org/10.1002/er.5599.

[66]   O. Kalkan, A. Celen, K. Bakirci, and A. S. Dalkilic, "Experimental investigation of thermal performance of novel cold plate design used in a Li-ion pouch-type battery," *Appl Therm Eng,* vol. 191, p. 116885, 2021/06/05/ 2021, doi: https://doi.org/10.1016/j.applthermaleng.2021.116885.

[67]   D. W. Sundin and S. Sponholtz, "Thermal Management of Li-Ion Batteries With Single-Phase Liquid Immersion Cooling," *IEEE Open Journal of Vehicular Technology,* vol. 1, pp. 82-92, 2020, doi: 10.1109/OJVT.2020.2972541.

[68]   A. S. Fleischer, *Thermal Energy Storage Using Phase Change Materials, Fundamentals and Applications* (SpringerBriefs in Applied Sciences and Technology). Springer International Publishing, 2015.

[69]   S. Landini, J. Leworthy, and T. S. O'Donovan, "A Review of Phase Change Materials for the Thermal Management and Isothermalisation of Lithium-Ion Cells," *Journal of Energy Storage,* vol. 25, 2019, doi: 10.1016/j.est.2019.100887.

[70]   L. Luo and N. Le Pierrès, "Chapter 3 - Innovative Systems for Storage of Thermal Solar Energy in Buildings," in *Solar Energy Storage*, B. Sørensen Ed. Boston: Academic Press, 2015, pp. 27-62.

[71]   S. A. Khateeb, S. Amiruddin, M. Farid, J. R. Selman, and S. Al-Hallaj, "Thermal management of Li-ion battery with phase change material for electric scooters: Experimental validation," *Journal of Power Sources,* vol. 142, no. 1-2, pp. 345-353, 2005, doi: 10.1016/j.jpowsour.2004.09.033.

[72]   A. Mills and S. Al-Hallaj, "Simulation of passive thermal management system for lithium-ion battery packs," *Journal of Power Sources,* vol. 141, no. 2, pp. 307-315, 2005/03/01/ 2005, doi: https://doi.org/10.1016/j.jpowsour.2004.09.025.

[73]   X. Duan and G. F. Naterer, "Heat transfer in phase change materials for thermal management of electric vehicle battery modules," *International Journal of Heat and Mass Transfer,* vol. 53, no. 23, pp. 5176-5182, 2010/11/01/ 2010, doi: https://doi.org/10.1016/j.ijheatmasstransfer.2010.07.044.

[74]   J. Weng, X. Yang, G. Zhang, D. Ouyang, M. Chen, and J. Wang, "Optimization of the detailed factors in a phase-change-material module for battery thermal management," *International Journal of Heat and Mass Transfer,* vol. 138, pp. 126-134, 2019, doi: 10.1016/j.ijheatmasstransfer.2019.04.050.

[75]   Z. Ling, F. Wang, X. Fang, X. Gao, and Z. Zhang, "A hybrid thermal management system for lithium ion batteries combining phase change materials

with forced-air cooling," *Applied Energy,* vol. 148, pp. 403-409, 2015/06/15/ 2015, doi: https://doi.org/10.1016/j.apenergy.2015.03.080.

[76]   G.-H. Kim, J. Gonder, J. Lustbader, and A. Pesaran, "Thermal Management of Batteries in Advanced Vehicles Using Phase-Change Materials," *World Electric Vehicle Journal,* vol. 2, no. 2, 2008, doi: 10.3390/wevj2020134.

[77]   Z. Liu, Q. Hu, S. Guo, L. Yu, and X. Hu, "Thermoregulating Separators Based on Phase-Change Materials for Safe Lithium-Ion Batteries," *Advanced Materials,* https://doi.org/10.1002/adma.202008088 vol. 33, no. 15, p. 2008088, 2021/04/01 2021, doi: https://doi.org/10.1002/adma.202008088.

[78]   A. Kulshreshtha and S. K. Dhakad, "Preparation of metal foam by different methods: A review," *Materials Today: Proceedings,* vol. 26, pp. 1784-1790, 2020/01/01/ 2020, doi: https://doi.org/10.1016/j.matpr.2020.02.375.

[79]   M. F. Ashby, T. Evans, N. A. Fleck, J. Hutchinson, H. Wadley, and L. Gibson, *Metal foams: a design guide*. Elsevier, 2000.

[80]   H.-P. Degischer and B. Kriszt, *Handbook of cellular metals*. Wiley-VCH, Weinheim, 2002.

[81]   M. D. Goel, V. A. Matsagar, S. Marburg, and A. K. Gupta, "Comparative performance of stiffened sandwich foam panels under impulsive loading," *Journal of performance of constructed facilities,* vol. 27, no. 5, pp. 540-549, 2013.

[82]   J. Banhart, "Manufacture, characterisation and application of cellular metals and metal foams," *Progress in materials science,* vol. 46, no. 6, pp. 559-632, 2001.

[83]   X. Xiao, P. Zhang, and M. Li, "Preparation and thermal characterization of paraffin/metal foam composite phase change material," *Applied Energy,* vol. 112, pp. 1357-1366, 2013/12/01/ 2013, doi: https://doi.org/10.1016/j.apenergy.2013.04.050.

[84]   Z. Wang, Z. Zhang, L. Jia, and L. Yang, "Paraffin and paraffin/aluminum foam composite phase change material heat storage experimental study based on thermal management of Li-ion battery," *Appl Therm Eng,* vol. 78, pp. 428-436, 2015, doi: 10.1016/j.applthermaleng.2015.01.009.

[85]   W. Q. Li, Z. G. Qu, Y. L. He, and Y. B. Tao, "Experimental study of a passive thermal management system for high-powered lithium ion batteries using porous metal foam saturated with phase change materials," *Journal of Power Sources,* vol. 255, pp. 9-15, 2014/06/01/ 2014, doi: https://doi.org/10.1016/j.jpowsour.2014.01.006.

[86]   X. Wang *et al.*, "Performance analysis of a novel thermal management system with composite phase change material for a lithium-ion battery pack," *Energy,* vol. 156, pp. 154-168, 2018/08/01/ 2018, doi: https://doi.org/10.1016/j.energy.2018.05.104.

[87]   W. Wu *et al.*, "An experimental study of thermal management system using copper mesh-enhanced composite phase change materials for power battery pack," *Energy,* vol. 113, pp. 909-916, 2016/10/15/ 2016, doi: https://doi.org/10.1016/j.energy.2016.07.119.

[88]   L. W. Traub, "Calculation of constant power lithium battery discharge curves," *Batter,* vol. 2, no. 2, 2016, doi: 10.3390/batteries2020017.

[89]   Y. Zhao *et al.*, "Performance of a liquid cooling-based battery thermal management system with a composite phase change material," *International Journal of Energy Research,* vol. 44, no. 6, pp. 4727-4742, 2020, doi: 10.1002/er.5254.

[90]   H. Behi *et al.*, "A new concept of thermal management system in Li-ion battery using air cooling and heat pipe for electric vehicles," *Appl Therm Eng,* vol. 174, p. 115280, 2020/06/25/ 2020, doi: https://doi.org/10.1016/j.applthermaleng.2020.115280.

[91]   M. Duff and J. Towey. (2010) Two Ways to Measure Temperature Using Thermocouples Feature Simplicity, Accuracy, and Flexibility. *Analog Dialogue*. 3-8. Available: www.analog.com/analogdialogue

[92]   H. Chikh-Bled, K. Chah, A. Gonzalez-Vila, B. Lasri, and C. Caucheteur, "Behavior of femtosecond laser-induced eccentric fiber Bragg gratings at very high temperatures," *Opt. Lett.,* vol. 41, no. 17, pp. 4048--4051, 2016, doi: 10.1364/OL.41.004048.

[93]   W. R. Habel, "Optical Fiber Methods in Nondestructive Evaluation," (Handbook of Advanced Nondestructive Evaluation, 2019, pp. 595-642.

[94]   A. Raghavan *et al.*, "Embedded fiber-optic sensing for accurate internal monitoring of cell state in advanced battery management systems part 1: Cell embedding method and performance," *Journal of Power Sources,* vol. 341, pp. 466-473, 2017, doi: 10.1016/j.jpowsour.2016.11.104.

[95]   S. Novais *et al.*, "Internal and external temperature monitoring of a li-ion battery with fiber bragg grating sensors," *Sensors,* vol. 16, no. 9, p. 1394, 2016, doi: 10.3390/s16091394 PMID - 27589749.

[96]   M. Nascimento *et al.*, "Lithium batteries temperature and strain fiber monitoring," *24th International Conference on Optical Fibre Sensors,* vol. 9634, p. 96347V, 2015, doi: 10.1117/12.2195218.

[97]   L. W. Sommer *et al.*, "Embedded fiber optic sensing for accurate state estimation in advanced battery management systems," *Mrs Proc,* vol. 1681, 2014, doi: 10.1557/opl.2014.560.

[98]   A. Ramanujam, P. Sankaranarayanan, A. Vasan, R. Jayaprakash, V. Sarangan, and A. Sivasubramaniam, "Qantifying The Impact of Electric Vehicles On The Electric Grid: A Simulation Based Case-Study," *e-Energy '17: The Eighth International Conference on Future Energy Systems,* pp. 228-233, 2017, doi: 10.1145/3077839.3077854.

[99]   Á. González-Vila, A. Ioannou, M. Loyez, M. Debliquy, D. Lahem, and C. Caucheteur, "Surface plasmon resonance sensing in gaseous media with optical fiber gratings," *Opt Lett,* vol. 43, no. 10, p. 2308, 2018, doi: 10.1364/ol.43.002308 PMID - 29762579.

[100]   Y. Xie *et al.*, "An improved electrothermal-coupled model for the temperature estimation of an air-cooled battery pack," *International Journal of Energy Research,* vol. 44, no. 3, pp. 2037-2060, 2019, doi: 10.1002/er.5058.

[101] T. H. Dubaniewicz, Jr. and J. P. DuCarme, "Are Lithium Ion Cells Intrinsically Safe?," *IEEE Trans Ind Appl,* vol. 49, no. 6, pp. 2451-2460, 2013, doi: 10.1109/TIA.2013.2263274.

[102] S. Panchal, M. Mathew, R. Fraser, and M. Fowler, "Electrochemical thermal modeling and experimental measurements of 18650 cylindrical lithium-ion battery during discharge cycle for an EV," *Appl Therm Eng,* vol. 135, pp. 123-132, 2018, doi: 10.1016/j.applthermaleng.2018.02.046.

[103] K. K. Parsons and T. J. Mackin, "Design and Simulation of Passive Thermal Management System for Lithium-Ion Battery Packs on an Unmanned Ground Vehicle," *Journal of Thermal Science and Engineering Applications,* vol. 9, no. 1, 2017, doi: 10.1115/1.4034904.

[104] R. d. S. Marques *et al.*, "Corrosion Resistant FBG-Based Quasi-Distributed Sensor for Crude Oil Tank Dynamic Temperature Profile Monitoring," *Sensors,* vol. 15, no. 12, pp. 30693-30703, 2015, doi: 10.3390/s151229811 PMID - 26690166.

[105] S. S. Zhang, K. Xu, and T. R. Jow, "Study of the charging process of a LiCoO2-based Li-ion battery," *Journal of Power Sources,* vol. 160, no. 2, pp. 1349-1354, 2006/10/06/ 2006, doi: https://doi.org/10.1016/j.jpowsour.2006.02.087.

[106] A. Barai, G. H. Chouchelamane, Y. Guo, A. McGordon, and P. Jennings, "A study on the impact of lithium-ion cell relaxation on electrochemical impedance spectroscopy," *Journal of Power Sources,* vol. 280, pp. 74-80, 2015, doi: 1.

[107] Y. Wang, Z. Chen, and C. Zhang, "On-line remaining energy prediction: A case study in embedded battery management system," *Applied Energy,* vol. 194, pp. 688-695, 2017/05/15/ 2017, doi: https://doi.org/10.1016/j.apenergy.2016.05.081.

[108] J. Kleiner, M. Stuckenberger, L. Komsiyska, and C. Endisch, "Advanced Monitoring and Prediction of the Thermal State of Intelligent Battery Cells in Electric Vehicles by Physics-Based and Data-Driven Modeling," *Batter,* vol. 7, no. 2, 2021, doi: 10.3390/batteries7020031.

[109] C.-Y. Lee *et al.*, "Integrated microsensor for real-time microscopic monitoring of local temperature, voltage and current inside lithium ion battery," *Sensors and Actuators A: Physical,* vol. 253, pp. 59-68, 2017/01/01/ 2017, doi: https://doi.org/10.1016/j.sna.2016.10.011.

[110] M. M. U. Rehman, F. Zhang, M. Evzelman, R. Zane, K. Smith, and D. Maksimovic, "Advanced cell-level control for extending electric vehicle battery pack lifetime," in *2016 IEEE Energy Conversion Congress and Exposition (ECCE)*, 18-22 Sept. 2016 2016, pp. 1-8, doi: 10.1109/ECCE.2016.7854827.

[111] A. Hussain, I. H. Abidi, C. Y. Tso, K. C. Chan, Z. Luo, and C. Y. H. Chao, "Thermal management of lithium ion batteries using graphene coated nickel foam saturated with phase change materials," *International Journal of Thermal Sciences,* vol. 124, pp. 23-35, 2018, doi: https://doi.org/10.1016/j.ijthermalsci.2017.09.019.

[112] S. Inazawa, A. Hosoe, M. Majima, and K. Nitta, "Novel plating technology for metallic foam," *SEI Tech Rev,* vol. 71, pp. 23-30, 2010.

[113] "The Thermal Conductivity of Unfilled Plastics." https://ctherm.com/resources/newsroom/blog/the-thermal-conductivity-of-unfilled-plastics/ (accessed 2023).

[114] "THERMAL CONDUCTIVITY OF PLASTICS." https://engineerexcel.com/thermal-conductivity-plastic/#:~:text=%E2%80%9CHigh%20conductivity%E2%80%9D%20plastics%20are%20those,carbon%20fibers%2C%20and%20carbon%20nanotubes. (accessed 2023).

[115] W. Sha, X. Wu, and K. G. Keong, *Electroless Copper and Nickel-Phosphorus Plating: Processing, Characterisation and Modelling*. Woodhead Publishing, 2011.

[116] L. Wang, L. Sun, and J. Li, "Electroless Copper Plating on Fraxinus Mandshurica Veneer using Glyoxilix Acid as a Reducing Agent," *Biosources,* vol. 6, no. 3, pp. 3493-3504, 2011.

[117] F. Hanna, Z. A. Hamid, and A. A. Aal, "Controlling factors affecting the stability and rate of electroless copper plating," *Materials Letters,* vol. 58, no. 1-2, pp. 104-109, 2004, doi: 10.1016/s0167-577x(03)00424-5.

[118] L. Wei. "Copper electroplating fundamentals." https://www.dupont.com/electronic-materials/blogs/knowledge/copper-electroplating-fundamentals.html# (accessed.

[119] A. Bhattacharya, V. V. Calmidi, and R. L. Mahajan, "Thermophysical properties of high porosity metal foams," *International Journal of Heat and Mass Transfer,* vol. 45, no. 5, pp. 1017-1031, 2002/02/01/ 2002, doi: https://doi.org/10.1016/S0017-9310(01)00220-4.

[120] A. Diani and L. Rossetto, "Melting of PCMs Embedded in Copper Foams: An Experimental Study," *Materials,* vol. 14, no. 5, 2021, doi: 10.3390/ma14051195.

[121] H. Disk. "Technology - Hot Disk." https://www.hotdiskinstruments.com/technology/ (accessed.

Appendix A: MICROCAL 2 Calibration Certificate

CERTIFICATE OF CALIBRATION

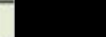| Date Of Issue	Certificate Number
7th December 2021	071221/TCS4

UKAS CALIBRATION 0601

Certificate Issued By:

eti

Electronic Temperature Instruments Ltd
Unit 1, Tevile Industrials, Worthing
West Sussex BN14 8NW, UK
tel: 01903 202151
email: sales@etiltd.co.uk
www.etiltd.com

Page 1 of 1 pages	
Approved Signatory	Signature
S. Wells	

Customer Name: PASS (PORTABLE APPLIANCE SAFETY SERVICES) LIMITED
Address: 1 WILSON STREET
THORNABY
STOCKTON-ON-TEES
COUNTY DURHAM
TS17 7AR

Order Number: 48684   Ref Number: 911/90947
Date Received: 19th November 2021
Date Calibrated: 6th December 2021
Ambient Temperature: 23 °C ± 3 °C   Ambient Humidity: < 60 %rh
Temperature Scale: International Temperature Scale of 1990
Instrument Type : ETI MICROCAL 2 'K' SIMULATOR
Instrument Serial Number: D21467916

Procedure: The instrument was stabilised at ambient temperature, then calibrated by measuring its
output on traceable reference equipment, the temperature equivalent was calculated
from BS EN 60584-1: 2013 reference tables.

Results:

Test Temperature °C	Nominal mV	Measured mV	Equiv Temperature °C	Measurement Uncertainty °C
- 20.0	- 0.777 5	- 0.773 1	- 19.89	± 0.30
0.0	0.000 0	- 0.004 8	- 0.12	± 0.30
+ 100.0	+ 4.096 2	+ 4.092 0	+ 99.87	± 0.30
+ 195.0	+ 7.938 7	+ 7.945 4	+ 195.16	± 0.29
+ 500.0	+ 20.644 3	+ 20.643 7	+ 499.97	± 0.29

Readings taken with the instruments cjc on.

End of Report

The reported expanded uncertainty is based on a standard uncertainty multiplied by a coverage factor k=2, providing a level of confidence of approximately 95%. The uncertainty evaluation has been carried out in accordance with UKAS requirements.

The results indicate performance of instrument at time of measurement, with no warranty as to specification, repeatability or long term stability.

This certificate is issued in accordance with the laboratory accreditation requirements of the United Kingdom Accreditation Service. It provides traceability of measurement to the SI system of units and/ or units of measurement realised at the National Physical Laboratory or other recognised national metrology institutes including the National Institute of Standards and Technology (NIST).This certificate may not be reproduced other than in full, except with the prior written approval of the issuing laboratory.

Appendix B: ESPEC LU-114 Calibration Certificate

試 験 検 査 報 告 書
TEST AND INSPECTION REPORT

ESPEC

PASSED
ESPEC CORP.
INSPECTION SECTION

製 品 名 Product Name	恒温器 Temperature Chamber	
型 式 Model	LU−114	
製造番号 Serial No.	1013003563	

製造年月日 Date of Manufacturing :	2020年3月 Mar.2020	試験年月日 : Date of Test :	2020年3月10日 Mar.10.2020
製造場所 : Place :	エスペックテストシステム㈱ ESPEC TEST SYSTEM CORP.	外囲温度 Ambient Temp. :	19 ℃
試験電源 Power Source:	AC 230V 1φ 60Hz	検査員 : Inspector :	中村 隆英 T.Nakamura

試験検査項目 Test and Inspection Item	仕 様 Specification	試験検査結果 Test Result	判 定 Judgement
各部の機能 Function			GOOD
装備品 Mechanical Fitting			GOOD
外 観 Appearance			GOOD
付 属 品 Accessories			GOOD
性 能 Performance 1. 温度範囲 Temperature range	−20℃〜+85℃	−20℃〜+85℃	GOOD
2．温度変動 Temperature constancy	±1.0	±1.0℃以内 less then ±1.0℃	GOOD
3. 温度極値到達時間 下降 Temp pull-down Time rate	20℃〜−20℃まで 130分以内 20℃ to −20℃ within 130min.	58 分 58 min.	GOOD
電気特性 Electrical Characteristic 絶縁抵抗 Insulation Resistance	10MΩ以上(DC500Vメガ) Over 10MΩ (DC 500V Mega)	100 MΩ	GOOD
電気容量 Capacity 加熱器 Heater	H1 AC230V600W (2.4〜2.8 A)	2.5 A	GOOD
冷凍機 Refrigerater	less than RU1 AC100V250W (3.7 A以下)	1.6 A	GOOD

最終判定 Final Judgement GOOD	検査責任者 Chief Inspector	██████

エスペック株式会社
ESPEC CORP.

Appendix C: EEMB LP963450-PCM-LD Battery Data Sheet

| Document Name	Document No.	Ver	Date	Page
LP963450LC-PCM-LD/ Specification	ZJQM-RD-SPC-H0132	0.0	2018-10-25	3/11

1. Scope 适用范围

This product specification defines the requirements of the rechargeable polymer lithium-ion battery supplied to the customer by EEMB Co., Ltd.

本产品规格书适用于 EEMB 提供的聚合物锂离子电池。

2. Battery Cell Basic Characteristics 电芯产品基本特性

No.	Item 项目		Characteristics 性能指标		Remark 备 注
2.1	Model 型 号		LP963450LC		
2.2	Capacity 容量	Nominal Capacity 标称容量	1800	mAh	0.2C₅A
		Minimum 最小容量	1700	mAh	0.2C₅A
2.3	Nominal Voltage 额定电压		3.7	V	
2.4	Weight 重 量		Approx.36	g	
2.5	Internal Impedance 内 阻	≤	70	mΩ	AC 1KHz(50% charge)
2.6	Dimension 外形尺寸	Length 长	≤ 51	mm	
		Width 宽	≤ 34.5	mm	
		Thickness 主体厚	≤ 9.9	mm	
2.7	Charge 充 电	Maximum Current 最大充电电流	1800	mA	1C₅A（CC&CV）
		Limited Voltage 充电上限电压	4.200±0.020	V	
		End-of Current 充电截至电流	36	mA	
2.8	Discharge 放 电	Maximum Current 最大放电电流	3600	mA	2.0C₅A
		Cut-off Voltage 放电终止电压	2.750±0.005	V	
2.9	Operation Temperature 工作温度	Charge 充电温度	0～45	℃	
		Discharge 放电温度	−40～+45	℃	
2.10	Storage Temperature 贮存温度	1 month 1 个月（贮存期）	−20～+60	℃	
		3 months 3 个月（贮存期）	−20～+45	℃	
		12 months 12 个月（贮存期）	−20～+25	℃	
2.11	Storage Relative Humidity 贮存湿度		65±20	%	

Appendix D: Panasonic NCR18650B Battery Data Sheet
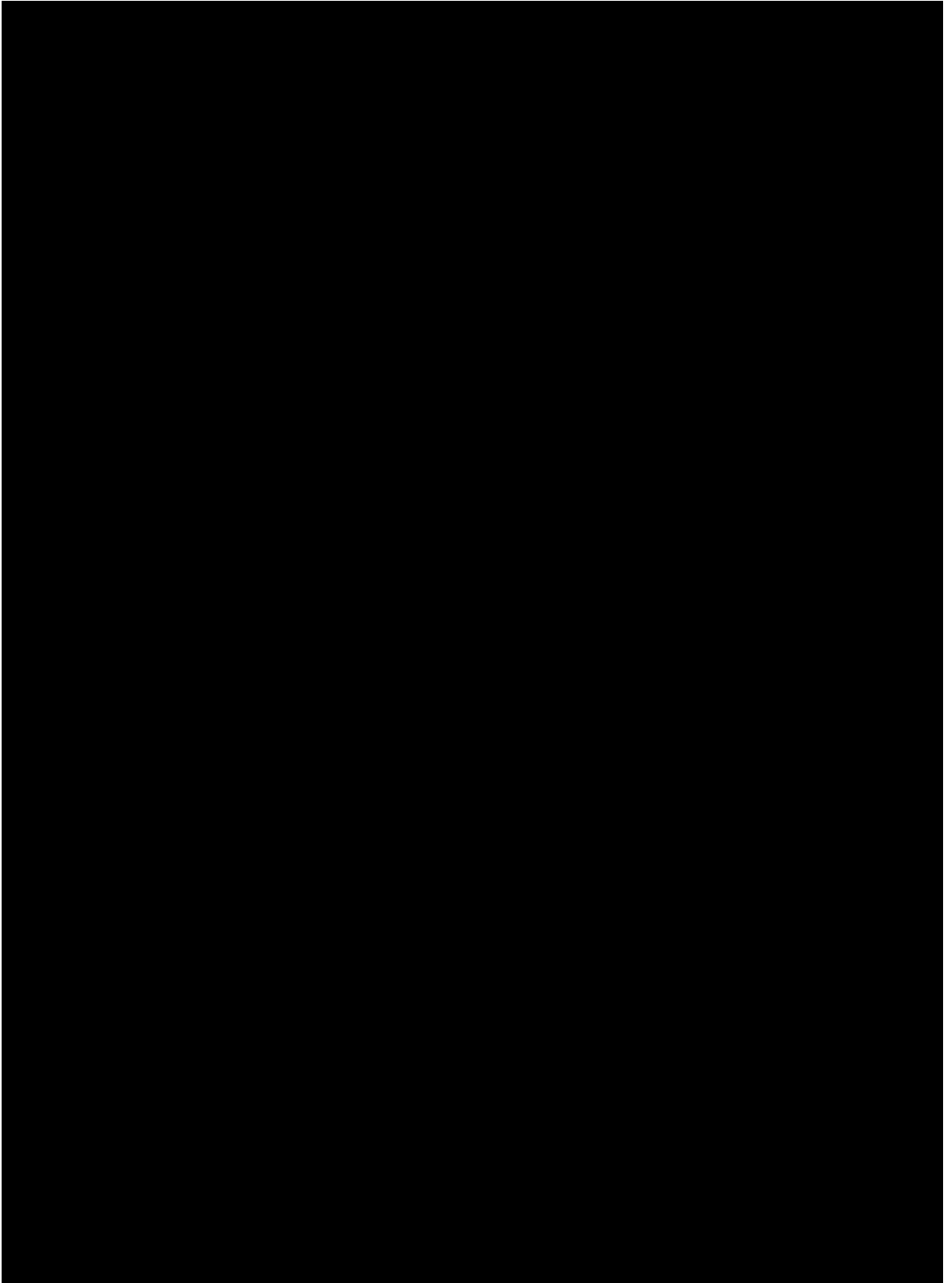
Appendix E: Goodfellow Copper Foam Quote

Goodfellow

Goodfellow Cambridge Limited
Ermine Business Park, Huntingdon PE29 6WR England
Email : info@goodfellow.com
Web : www.goodfellow.com
Telephone 0800 731 4653
Fax 0800 328 7689

Napier University Ventures Ltd.
Edinburgh Napier University
Merchiston Site
10 Colinton Road
EDINBURGH
EH10 5DT
UNITED KINGDOM

Your reference	E-mail
Dated	6-February-2020
Our reference	869471/D E Innamorato
Date	27-February-2020
Direct Dial Telephone	
	Page 2

4. Copper Foam 99.9%
   Density   : 850g/m2
   Porosity   : 89.0%
   PPI   : 20ppi Open cell
   Thickness : 5.0mm (nominal)
   Size   : 200mm x 200mm (nominal)

   Quantity   : 1 pc   Price : GBP 487.00 / pc

3. Copper Foam 99.9%
   Density   : 850g/m2
   Porosity   : 89.0%
   PPI   : 10 open cell
   Thickness : 5.0mm (nominal)
   Size   : 200mm x 200mm (nominal)

   Quantity   : 1 pc   Price : GBP 477.00 / pc

Appendix F: Polymer Foam Quote

Hi Keith,

Good afternoon and I hope you are well?

First of all, thank you for your email enquiry and interest in our products. We now have the pleasure of confirming as follows:

Option 1: ZOUCHretic 10FR - Plain Open-Cell Reticulated Polyester Filter Foam Cut Sheets

Material: ZOUCHretic 10FR
Porosity: 10ppi (10 cells per inch square)
Colour: Black
Density: 26 to 32 Kgs/m3
Drawing No: N/A
Description: Plain Open-Cell Flame Retardant Reticulated Polyester Filter Foam Cut Sheets
Adhesive System: N/A (supplied Plain without adhesive)
Size: 150mm Wide X 10mm Thick X 210mm Long
Presentation: Individually Cut Sheets
MOQ: **6 Units**
Price: **£2.85 per unit**
Availability: 7/10 working days from receipt of order subject to workload at the time of production

Option 2: ZOUCHretic 20FR - Plain Open-Cell Reticulated Polyester Filter Foam Cut Sheets

Material: ZOUCHretic 20FR
Porosity: 20ppi (20 cells per inch square)
Colour: Black
Density: 26 to 32 Kgs/m3
Drawing No: N/A
Description: Plain Open-Cell Flame Retardant Reticulated Polyester Filter Foam Cut Sheets
Adhesive System: N/A (supplied Plain without adhesive)
Size: 150mm Wide X 10mm Thick X 210mm Long
Presentation: Individually Cut Sheets
MOQ: **6 Units**
Price: **£2.66 per unit**
Availability: 7/10 working days from receipt of order subject to workload at the time of production